

UNIVERSITY OF NAPLES FEDERICO II

*Department of Structures  
For Engineering and Architecture*

PH.D. PROGRAMME IN  
STRUCTURAL, GEOTECHNICAL AND SEISMIC ENGINEERING  
COORDINATOR PROF. LUCIANO ROSATI  
XXXII CYCLE



*ROSANNA NAPOLITANO*

PH.D. THESIS

EXPERIMENTAL AND NUMERICAL INVESTIGATIONS ON  
COLD JOINTS IN 3D CONCRETE PRINTED ELEMENTS

TUTOR:  
PROF. ING. ASPRONE DOMENICO

**2018-2019**



To **Claudio**, my partner on a vibrant journey,  
full of life and love.



# Acknowledgements

Foremost, I would like to express my gratitude to my supervisor Professor Domenico Asprone, providing me with precious advice and helpful support during the years of this Ph.D study.

My deepest thanks to Costantino Menna for his encouragement, motivation and essential guidance, helping me in all the time of research and making the completion of this research possible. Thank you for everything!

I want to thank all the members of staff of the Department of Structures for Engineering and Architecture at the University of Naples Federico II.

I wish also to acknowledge the help and hospitality provided throughout my Ph.D Visiting period by the Professor Ezio Cadoni and his technical staff in the DynaMat laboratory of the University of Applied Sciences and Arts of Southern Switzerland.

Sincere gratitude to Lorenzo and Francesco: they provided, in different ways, a great support to my research. Furthermore, special gratitude to my colleague Alberto for sharing with me this unforgettable journey from start to finish.

A special thanks to all my past and present colleagues who have supported me and had to put up with my stresses and groans, giving me invaluable smiles and very nice moments. Among my colleagues I would like to thank especially my friends Martina, Fabrizia, Paolino, Giancarlo and Stefano for their daily precious support.

I gratefully acknowledge all my family members, my beloved brother, my sister in law and my close friends (Teresa, Giovanna, Carla, in particular) who have greatly contributed towards my evolution and supported me everyday.

And last but not the least, I would like to express my very special thanks to Claudio, for being a very special part of me. I am indebted to him with extreme sense of gratitude for the love, help and patience that he has been showing through these years and during the writing of this thesis.

Naples, April 2020



# Abstract

The interest and use of additive manufacturing (AM), also known as 3D-printing, has grown dramatically in the research and various industrial sectors, becoming a revolutionary technology that could up-end the last design approaches. Also the construction sector is recently getting in line with automation field, in order to create a significant synergy and open the door for innovative automatized manufacturing techniques which yield a new fabrication, named as digital fabrication. This method involves creating object from a 3D digital model by adding material without formworks, starting from the element conception by means of CAD technology.

In this context, the technology of 3D Concrete Printing (3DCP), an automated layer-by-layer casting with cementitious materials, has progressed rapidly over the last years. The possibility of obtaining complex shapes of building concrete structures avoiding the use of complicated formwork is a major advantage in term of production rate, architectural freedom, cost reduction and mostly positive environmental impact, considering that formworks represent about 35–60 % of the overall costs of concrete structures. Moreover, it allows human labor to be replaced by robots, thus increasing worker safety and speeding up the construction process.

Though these modern techniques have high potential, many concrete technological issues are still open and are yet to be scientifically investigated, such as the occurrence of weakness surface at the bond interface of the two printed filaments.

In the above outlined contest, a contribution in the assessment of layer interface mechanical behavior is provided by the present work on two scales: experimental and numerical. Special attention has been focused on the assessment of the

interlocking response to the dynamic loading condition.

A critical review of the state-of-the-art and of the theoretical background is firstly carried out: the review process has been dedicated to the current additive manufacturing technologies and in particular on 3D printing application in the construction field.

The experimental campaign, conducted at Laboratory of the Department of Structures for Engineering and Architecture, University of Naples "Federico II" and at DynaMat Laboratory of the University of Applied Sciences of Southern Switzerland (SUPSI) of Lugano, is presented. The experimental program comprised tests on printed and non-printed elements (prismatic and circular shaped), subjected to mechanical tests and DIC (digital image correlation) technique. All the tests were performed in quasi-static way and in dynamic condition. The mechanical characterization at medium and high strain rate was conducted by means of Modified Hopkinson bar and Hydro-Pneumatic Machine.

Experimental results for each specimens are reported: the results in terms of load versus displacement are shown and the evolution of the occurrence of fracture with increasing the force is described. An experimental influence of different constraints, such as resting time i.e. the time between the printings of two successive layers, on the strength of the interfaces is highlighted, in order to better understand the relevance of taking into account process parameters for interface behavior assessment. The numerical simulation, modelled by means of FEM (Finite Elements Method) analysis is also performed, aimed to validate the experimental results.

The last part of the work focuses on the definition of apposite and hypothetic strategies of interlaminar reinforcement implementation, optimizing the junction mechanical characteristics in the 3D printed elements. To this aim, the method of applying steel rods that pass across the junctions was proposed and tested, in order to examine the effect of the steel elements on the shear resistance of joints and to improve the overall behaviour of the elements realized through automated technology system. Based on the obtained results, the assessment of the capacity of the structural and non-structural printed components of achieving required performances is discussed.

Finally, future developments of this research work are presented, combining technological and sustainable aspects. The main goal is to use a material containing recycled carbon fibers as printable material, starting from a specific study on the influence of the percentage and length of fibers usage on the



mechanical performance of cement based carbon fibers-reinforced mortars.

**Keywords:** 3D Concrete printing; Bond strength; Experimental tests; Dynamic response; Numerical simulation; Failure mode; Shear strength assessment; Interlaminar reinforcement; Sustainability; Short carbon fibers.



# Tables of contents

ABSTRACT.....	7
TABLES OF CONTENTS .....	11
LIST OF FIGURES.....	13
LIST OF TABLES .....	19
CHAPTER 1 .....	21
INTRODUCTION .....	21
1.1 REASEARCH PURPOSE .....	21
1.2 WORK ORGANIZATION AND OUTLINE .....	26
REFERENCES.....	27
CHAPTER 2 .....	29
3D CONCRETE PRINTING: A NEW CHALLENGE FOR CONSTRUCTION INDUSTRY .....	29
2.1 HISTORY OF THE USE OF 3D PRINTING PROCESSES.....	30
2.2 3D PRINTING IN CONCRETE INDUSTRY .....	31
2.2.1 <i>Binder Jetting</i> .....	34
2.2.2 <i>Material deposition method (MDM)</i> .....	35
2.3 3D CONCRETE PRINTING PARAMETERS .....	39
2.3.1 <i>Printing machines</i> .....	42
2.3.2 <i>Rheological requirements</i> .....	45
2.3.2.1 <i>Workability of concrete</i> .....	49
2.3.2.2 <i>Buildability of concrete</i> .....	52
2.3.3 <i>Mechanical properties</i> .....	59
2.3.3.1 <i>Hardened properties: Influence of Geometry</i> .....	60
2.3.3.2 <i>Printing path</i> .....	62
2.4 RESEARCH GAP .....	64
REFERENCES.....	67
CHAPTER 3 .....	71
MECHANICAL CHARACTERIZATION OF THE INTERFACES OF 3D PRINTED CONCRETE ELEMENTS .....	71
3.1 EXPERIMENTAL SETUP DESIGN .....	74
3.1.1 <i>Punch-through shear test</i> .....	75
3.2 EXPERIMENTAL PROGRAM.....	79
3.2.1 <i>Material properties</i> .....	79

3.2.2.	<i>3D printing machine</i> .....	86
3.2.3.	<i>Specimen production</i> .....	88
3.2.4.	<i>Interface Measurement systems</i> .....	90
3.3	PUNCH-THROUGH SHEAR TEST RESULTS.....	96
	REFERENCES.....	111
<b>CHAPTER 4</b> .....		<b>113</b>
<b>NUMERICAL SIMULATION OF THE INTERFACE BEHAVIOUR OF 3D PRINTED CONCRETE ELEMENTS</b> .....		<b>113</b>
4.1	NUMERICAL ANALYSIS .....	114
4.1.1.	<i>Cohesive Model</i> .....	116
4.1.2.	<i>Cohesive Model calibration</i> .....	121
4.2	NUMERICAL RESULTS .....	123
4.2.1.	<i>Bulk concrete Element</i> .....	123
4.2.2.	<i>Layered concrete Element</i> .....	132
	REFERENCES.....	143
<b>CHAPTER 5</b> .....		<b>145</b>
<b>INTERLAMINAR REINFORCEMENT SYSTEM</b> .....		<b>145</b>
5.1	EXPERIMENTAL TEST AND RESULTS.....	150
5.2	NUMERICAL TEST AND RESULTS.....	161
5.3	SUMMARY .....	164
	REFERENCES.....	169
<b>CHAPTER 6</b> .....		<b>171</b>
<b>DYNAMIC CHARACTERIZATION OF 3D PRINTED CONCRETE ELEMENTS' INTERFACES</b> .....		<b>171</b>
6.1	EXPERIMENTAL PROGRAM.....	172
6.1.1.	<i>Material composition</i> .....	172
6.1.2.	<i>Specimens preparation</i> .....	173
6.2	EXPERIMENTAL SET-UP.....	175
6.2.1.	<i>Direct tensile setup</i> .....	176
6.2.1.	<i>Shear tests setup</i> .....	180
6.3	EXPERIMENTAL RESULTS.....	184
6.3.1.	<i>Tensile tests results</i> .....	184
6.3.2.	<i>Shear tests results</i> .....	193
	REFERENCES.....	200
<b>CHAPTER 7</b> .....		<b>203</b>
<b>CONCLUSIONS AND FUTURE DEVELOPMENTS: A SUSTAINABILITY PERSPECTIVE ON 3D PRINTING</b> .....		<b>203</b>

# List of Figures

Figure 1.1. First 3D-printed house produced in Italy .....	22
Figure 1.2. First 3D-printed bridge realized in Shanghai .....	22
Figure 1.3. Schematic working path .....	25
Figure 2.1. First stereolithography apparatus – a 3D printer (Hull, 1986) .....	30
Figure 2.2. Mapping 20 years of 3D printing in Construction, from 1906 to 2015 (Langenberg, 2015).....	32
Figure 2.3. Images of AMoC by various institutes: (a) Minibuilders (Institute of Advanced Architecture of Catalonia), (b) Concrete Printing (University of Loughborough), (c) Contour Crafting (University of Southern California), and (d) D-shape.....	33
Figure 2.4. Printing system of BJ technology (Meteyer et al. 2015) .....	34
Figure 2.5. Contour crafting process (Khoshnevis 2004) .....	37
Figure 2.6. Contour Crafting example by University of Southern California .....	37
Figure 2.7. Schematic of concrete delivery system (Le TT. et al., 2012) .....	39
Figure 2.8. Concrete Printing by the University of Loughborough (Lim et al., 2011) ....	39
Figure 2.9. The process of 3D printing for construction industry (Paul et al. 2017) .....	40
Figure 2.10. Printing process parameters (Salet et al. 2018) .....	41
Figure 2.11. 3D concrete printers (a) four-axis gantry and (b) six-axis autonomous robotic printer.....	44
Figure 2.12. Newtonian fluid’s behavior .....	46
Figure 2.13 Non Newtonian fluid's behaviour as function of time and shear rate.....	47
Figure 2.14 Yield stress of non-Newtonian fluids (Roussel N. 2012).....	47
Figure 2.15 Bingham Model .....	48
Figure 2.16 Thixotropy loop .....	49
Figure 2.17 Abrams Cone .....	50
Figure 2.18 Shapes of concrete, Abrams Cone .....	51
Figure 2.19 Heat spreading through time.....	54

Figure 2.20 Yield stress evolution over time. Experimental results comparison between the models by Perret et al. and Roussel .....	55
Figure 2.21 a) Fracture occurrence for a test carried out with time gap of 17 s; b) Sample after the test carried out with a time gap of 60 s.....	56
Figure 2.22 Displacement of the upper plate vs time.....	56
Figure 2.23 Comparison between critical stress and vertical stress history (Perrot, Rangeard, and Pierre 2016).....	57
Figure 2.24 Schematic of layered extrusion process with concrete (Wangler et al. 2016). A digitally controlled extrusion head moves at velocity $V$ , creating layers of individual height $h$ and width $w$ . The overall height $H_m$ is dependent on the velocity and contour length $L$ . .....	59
Figure 2.25 Example of 3D printed elements .....	60
Figure 2.26. Compression loads application in printed objects related to the printing direction.....	61
Figure 2.27. Flexural loads application in printed objects related to the printing direction.....	61
Figure 2.28. Print path adopted by Hambach et al. (Hambach, Rutzen, and Volkmer 2019) .....	63
Figure 2.29 left: Flexural behavior according to the print path; right: Compressive behavior according to the print path (Hambach, Rutzen, and Volkmer 2019).....	63
Figure 3.1. Interface bond strength test methods. A: pull-off test; B: splitting test; C: wedge splitting test; D: slant shear method; E: torsion bond strength test; F: shear strength test (Zareiyan and Khoshnevis 2017) .....	72
Figure 3.2. Fixture for bond shear test (Rahul et al. 2019) .....	74
Figure 3.3. Notched cube geometry.....	75
Figure 3.4. Punch-through shear test proposed by J. Davies (Davies et al. 1987) .....	76
Figure 3.5. Schematic of the modified Punch-through shear setup .....	77
Figure 3.6. Geometry of the setup .....	78
Figure 3.7. Supports details .....	78
Figure 3.8. Experimental setup .....	79
Figure 3.9. Printing of concrete elements.....	81
Figure 3.10. Schematic of mould frame for 160x40x40 mm prisms.....	82
Figure 3.11. Three point bending test setup .....	82
Figure 3.12. Bending moment diagram .....	83
Figure 3.13. Stress distribution along cross section.....	83

Figure 3.14. Uniaxial compression test setup .....	84
Figure 3.15. BigDelta WASP .....	86
Figure 3.16. Printing process .....	87
Figure 3.17. Printing Scheme .....	87
Figure 3.18. Printing Mode_ .....	89
Figure 3.19. Printing Mode_ .....	89
Figure 3.20. Printing Mode_ .....	90
Figure 3.21. Printing Mode_ .....	90
Figure 3.22. LVDT application .....	91
Figure 3.23. Image_setup_GUI.....	93
Figure 3.24. Correlate_images_GUI.....	93
Figure 3.25. Compute_data_GUI .....	94
Figure 3.26. Specimen for Digital Image Correlation.....	95
Figure 3.27. Image Acquisition Setup .....	95
Figure 3.28. P-d Plots of Bulk Concrete Specimens .....	97
Figure 3.29. left: $\gamma_{xy}$ distribution at the cracks onset, (bulk specimen 2_bk, point O); right: $\gamma_{xy}$ distribution at the failure, (bulk specimen 2_bk, point F) .....	97
Figure 3.30 Load-displacement curve, specimens group A ( $t_{r1}=100s$ ).....	98
Figure 3.31 Load-displacement curve, specimens group B ( $t_{r2}=200s$ ) .....	98
Figure 3.32 Load-displacement curve, specimens group C ( $t_{r3}=1800s$ ) .....	99
Figure 3.33 Load-displacement curve, specimens group D ( $t_{r4}=3600 s$ ).....	99
Figure 3.34 Comparison between average values of $P_{max}$ and $P_c$ .....	102
Figure 4.1. a) Mode I “opening mode”, b) Mode II “sliding mode”, c) Mode III “tearing mode” .....	114
Figure 4.2. Cohesive forces in the fracture process zone .....	117
Figure 4.3. Traction-separation law, cohesive model.....	118
Figure 4.4 Typical load-displacement curve from the punch- through test .....	119
Figure 4.5. Mode II, sliding mode.....	119
Figure 4.6. Schematic of node-based interaction .....	120
Figure 4.7 Comparison Compressive Curve, input vs output.....	121
Figure 4.8 Comparison Tensile Curve, input vs output .....	121

Figure 4.9 Three Point Bending test Simulation .....	122
Figure 4.10 Uniaxial compressive test Simulation.....	122
Figure 4.11 Bulk concrete element implemented in Abaqus .....	124
Figure 4.12 Plain concrete specimen: mesh and boundary conditions.....	126
Figure 4.13 Upper rigid body which simulates the loading plate.....	127
Figure 4.14 Load-displacement curve of Punch-Through test simulation of plain concrete.....	128
Figure 4.15 U2 evolution in Punch-through test simulation, plain concrete at 37th step .....	129
Figure 4.16 U2 evolution in Punch-through test simulation, plain concrete at 98 <sup>th</sup> step .....	129
Figure 4.17 U2 evolution in Punch-through test simulation, plain concrete at 538 <sup>th</sup> step .....	130
Figure 4.18 Cracks evolution, punch-through test simulation, plain concrete at 37 <sup>th</sup> step .....	130
Figure 4.19 Cracks evolution, punch-through test simulation, plain concrete at 538 <sup>th</sup> step .....	131
Figure 4.20 left: Single element part; right: Assembly .....	133
Figure 4.21 Surfaces .....	134
Figure 4.22 left: Mesh size of the specimen; right: Boundary conditions of the layered specimen.....	134
Figure 4.23 Vertical displacement distribution 1 <sup>st</sup> Step .....	137
Figure 4.24 Vertical displacement distribution 12 <sup>th</sup> Step.....	137
Figure 4.25 Vertical displacement distribution 27 <sup>th</sup> Step.....	138
Figure 4.26 Vertical displacement distribution 83 <sup>rd</sup> Step.....	138
Figure 4.27 Shear stress distribution through fracture surfaces at 1 <sup>st</sup> Step .....	139
Figure 4.28 Shear stress distribution through fracture surfaces at 12 <sup>th</sup> Step.....	140
Figure 4.29 Shear stress distribution through fracture surfaces at 27 <sup>th</sup> Step.....	141
Figure 4.30 Shear stress distribution through fracture surfaces at 83 <sup>rd</sup> Step .....	141
Figure 4.31 Load vd Displacement curve, layered specimen simulation.....	142
Figure 5.1 Experimental and numerical curve, bulk material specimen.....	146
Figure 5.2 Experimental and numerical curve, un-reinforced specimen group A .....	147
Figure 5.3 Experimental and numerical curve, un-reinforced specimen group B .....	147



Figure 5.4 Experimental and numerical curve, un-reinforced specimen group C.....	148
Figure 5.5 Experimental and numerical curve, un-reinforced specimen group D .....	148
Figure 5.6. Rods system .....	150
Figure 5.7 Load-displacement curve, specimens group A_reinforced ( $t_{r1}=100s$ ).....	152
Figure 5.8 Load-displacement curve, specimens group B_reinforced ( $t_{r2}=200s$ ) .....	152
Figure 5.9 Load-displacement curve, specimens group C_reinforced ( $t_{r3}=1800s$ ).....	153
Figure 5.10 Load-displacement curve, specimens group D_reinforced ( $t_{r4}=3600s$ ).....	153
Figure 5.11 Vertical displacement distribution 1 <sup>st</sup> Step .....	162
Figure 5.12 Vertical displacement distribution 16 <sup>th</sup> Step.....	162
Figure 5.13 Vertical displacement distribution 38 <sup>th</sup> Step.....	163
Figure 5.14 Load vd Displacement curve, reinforced layered specimen simulation....	164
Figure 5.15 Experimental and numerical curve, specimen group A_reinforced .....	165
Figure 5.16 Experimental and numerical curve, specimen group A_reinforced .....	165
Figure 5.17 Experimental and numerical curve, specimen group C_ reinforced.....	166
Figure 5.18 Experimental and numerical curve, specimen group D_ reinforced .....	166
Figure 5.19 Comparison between average values of $P_{max}$ for unreinforced, reinforced and bulk material specimens.....	168
Figure 6.1. Size prismatic specimen .....	173
Figure 6.2. Size cylindrical specimen .....	174
Figure 6.3. Direct static tensile test setup.....	176
Figure 6.4. Hydro-Pneumatic Machine scheme.....	177
Figure 6.5. Hydro-Pneumatic Machine for medium strain-rate tests .....	177
Figure 6.6. Modified Hopkinson Tensile Bar apparatus (Cadoni et al, 2011) .....	178
Figure 6.7. Specimen place in Modified Hopkinson Tensile Bar.....	179
Figure 6.8. The design of Punch-through shear test setup.....	180
Figure 6.9. The design of Punch-through shear test setup.....	180
Figure 6.10. left: Modified Hopkinson compression Bar; right: shear testing specimen .....	182
Figure 6.11 Shear supports design.....	183
Figure 6.12. Shear supports production.....	184
Figure 6.13. Specimen with bulk material before and after static tensile test.....	186

Figure 6.14. Printed specimen with $T_s=30$ min before and after static tensile test .....	186
Figure 6.15. Specimen with $T_s=0$ min before a high strain rate tensile failure test .....	187
Figure 6.16. Specimen with $T_s=0$ min after a high strain rate tensile failure test .....	187
Figure 6.17. Specimen with $T_s=10$ min before a high strain rate tensile failure test ....	188
Figure 6.18. Specimen with $T_s=10$ min after a high strain rate tensile failure test .....	188
Figure 6.19. Fracture time, $T_f$ vs. strain velocity, $v_s$ data .....	189
Figure 6.20. Static series variance, in terms of tensile stress, at different strain rates ..	190
Figure 6.21. Stress vs time of group of specimens with $T_s=0$ min.....	191
Figure 6.22. Stress vs time of group of specimens with $T_s=10$ min.....	192
Figure 6.23. Stress vs time of group of specimens with $T_s=30$ min.....	192
Figure 6.24. Printed specimen with $T_s=0$ min before(left) and after (right) high dynamic tensile test.....	193
Figure 6.25. Printed specimen with $T_s=30$ min before(left) and after (right) high dynamic tensile test .....	193
Figure 6.26. Specimen failure history subjected to dynamic shear test (ID specimen: 3L_T0_005) at different steps.....	194
Figure 6.27. Specimen failure history subjected to dynamic shear test (ID specimen: 3L_T10_005) at different steps.....	195
Figure 6.28. Specimen failure history subjected to dynamic shear test (ID specimen: 3L_T30_005) at different steps.....	196
Figure 6.29. Bulk series variance percentage, in terms of shear stress .....	198
Figure 6.30. $DIF_\tau$ vs. Waiting time $T_s$ experimental data .....	199

# List of Tables

Table 2.1. Mix goals (Malaeb et al. 2015) .....	42
Table 3.1. Mixture composition.....	80
Table 3.2. Specimen labels for three point bending test .....	84
Table 3.3. Specimen labels for uniaxial compressive test .....	85
Table 3.4. Main features of specimens .....	89
Table 3.1. Experimental results for printed specimens .....	101
Table 3.2. The transversal strain distribution at the cracks onset and at the failure for a specimen (as an example) belonging to each group.....	106
Table 3.3. The images representing the failure for a specimen (as an example) belonging to each group.....	110
Table 4.1. Estimated values of characteristic length.....	116
Table 4.2. CDP model parameters .....	121
Table 4.3. Main mechanical parameters.....	123
Table 4.4. Mechanical properties .....	124
Table 4.5. Tensile Strength input data for CDP model .....	125
Table 4.6. Compressive Strength input data for CDP model.....	125
Table 4.7. Crack initiation load and maximum load .....	142
Table 5.1. Critical and Maximum Load average values comparison.....	149
Table 5.2. Main features of reinforced specimens .....	151
Table 5.3. Experimental results for printed reinforced specimens .....	154
Table 5.4. The transversal strain distribution at the failure for a specimen (as an example) belonging to each group .....	156
Table 5.5 The images representing the failure for a specimen (as an example) belonging to each group.....	160
Table 5.6. Parameters of the traction-separation law .....	161
Table 5.7. Parameters for rebars material characterization .....	161
Table 5.8. Crack initiation load and maximum load .....	164

*List of Tables*

---

Table 5.9. Critical and Maximum Load average values comparison.....	167
Table 6.1. Specimen labels .....	175
Table 6.2. Normal stresses of non-printed and printed mortars .....	189
Table 6.3. Transversal stress of non-printed and printed mortars .....	197

# Chapter 1

## INTRODUCTION

### 1.1 Research purpose

In the modern Fourth industrial revolution, namely Industry 4.0, the integration of intelligent production systems and advanced information technologies play an important role on economic competitiveness (Zawadzki and Zywicki 2016). More specifically, Industry 4.0 refers to the emergence and diffusion of a range of new digital industrial technologies (Rüßmann et al. 2015), notably embedded computer networks or accelerated wireless connections for gathering information from physical objects (the Internet of Things); the collection and real-time evaluation of data to optimize the costs and quality of production (Big Data and Analytics); robots with greater autonomy and flexibility; and advanced manufacturing techniques, such as Additive Manufacturing AM (3-D printing).

On the other hand, the physical part of the smart factories is limited by the capability of the existing manufacturing systems. This makes the AM as one of the vital components of Industry 4.0. and a key technology for fabricating customized products due to its ability to create objects with advanced attributes, such as new materials and sophisticated shapes. The Additive Manufacturing technologies, defined by American Society for Testing and Materials (ASTM) as "the process of joining materials to make objects from 3D model data, usually layer upon layer, as opposed to subtractive manufacturing methodologies, such as traditional machining" (ASTM F2792 - 10), are currently used in various industries such as aerospace, biomedical, and manufacturing (Thompson et al. 2016). Recently, AM methods are arousing an increasing interest also in the construction sector, and in particular in the concrete technology, as demonstrated by recent projects and showed in Figures 1.1 and 1.2. In fact, while conventional

construction processes are mainly based on subtractive technologies, where the material is treated to get the final object, for example natural stones or ceramic pavements or on formative technologies, where the material is poured into a mould at liquid state, such as reinforced concrete (Buswell et al. 2007), these technologies still represent a novelty in this field, making possible the creation of an object through material's multiple filaments overlap.



Figure 1.1. First 3D-printed house produced in Italy



Figure 1.2. First 3D-printed bridge realized in Shanghai

The adoption of additive manufacturing technologies potentially brings a number of advantages (Sasson and Johnson 2016; Laplume et al., 2016). Firstly, it guarantees greater freedom in the design of shapes, elements and structures, for functional and esthetic purposes, often referred as freeform constructions (Asprone et al. 2018). Then, other advantages include reduction in construction cost by avoiding formwork and human labor and in construction time by operating at a constant rate, increasing worker safety and production speed, minimizing the errors through automated material deposition. Finally, digital fabrication leads to more sustainability in construction by reducing waste generation (Wangler et al. 2016).

Among the main families of concrete digital fabrication techniques of concrete-like elements, most developments have been focused on layered extrusion technology, probably due to its procedure which is based on the more widespread production of polymeric elements. Briefly, this technique consists of a digitally controlled nozzle which precisely extrudes concrete layer upon layer. The layers are generally on the order of few centimeters. The material is laid down continuously following a pre-set path till the end of the first layer, subsequently the second layer is printed above and so on (Perkins and Skitmore, 2015; Le et al., 2012).

However, additive manufacturing technologies currently suffer from a number

of drawbacks, which limit their spread. Firstly, the control of the material hardening over time is the most important issue. In fact, the time gap between two layers should be the shortest possible to ensure a maximum bond between two layers but long enough to have a self-sustaining element. Achieving a proper time gap that balances the two requirements depicted above, the rheological properties of the fresh concrete material assume a great relevance (Valkenaers et al., 2014; Paul et al., 2018). In particular, the concrete has to assure:

- workability, in order to optimize the transportation of the suspension through the printing head,
- pumpability, i.e. the capacity to be worked and moved to the printing head through a pumping system within a given time interval,
- extrudability, so to be extruded properly through the printing head with material flow,
- buildability, remaining stacked in layers after extrusion and sustaining at the same time the weight of the subsequent layers that are deposited by the printing process.

Moreover, the layered extrusion technology necessarily creates interfaces between subsequently deposited layers, namely “Cold Joint”. These surfaces might create a potential zone of weakness into the printed structures and depend on different parameters, such as the time between the printings of two successive layers. Various authors studied the influence of interfaces on mechanical performances in 3D printing concrete. Le et al. (Le et al., 2012) investigated the tensile strength of the interlayers, deducing a decrease in strength with increasing interval times. Nerella et al. (Nerella and Mechtcherine, 2017a) performed mechanical tests and SEM (scanning electron microscope) investigations of microstructure at the interface of substrate. For two printable mixtures and different interval times (1 min, 10 min and 1 day), the strength exhibited a significant reductions, which in the case of one mixture was around 50% for 1 min and over 90% for 1 day. In the work of Wolfs et al. (Wolfs, Bos and Salet, 2019) the results of an experimental campaign on the relation between 3D printing process parameters (interface interval time, nozzle height) and the compressive and tensile strength, determined through flexural and splitting tests, were presented, in three perpendicular directions. The strength reduces as the layer interval time increases. In the flexural and splitting tests, a bond strength reduction of 16% and 21% respectively was measured at the 24h interval compared to the 15s. For the

layer interval times of 1h and 4h, only a minor drop in strength is observed in both tests, indicating that even if the print process is delayed for a significant period of time, the strength properties remain approximately equal, given adequate covering of the specimens during this period. Furthermore, reductions up to 72% have been reported for the interlayer interval time of 60 min by Kim et al. (Kim et al. 2017), while the results of Panda et al. indicate 75% reduction at an interval time of 20 min (Biranchi Panda, Chandra Paul, and Jen Tan, 2017).

In spite of everything, a specific study on mechanical characterization of interfaces behavior and in addition a comparison between mechanical and numerical characterization have not been reported yet.

The situation outlined above is sufficient to understand that the state of the art on assessment of interfaces behavior in 3D printed elements still needs to be advanced in several aspects.

This work aims at contributing to the determination of mechanical properties of printed concrete elements and, in particular, on the characterization of the interface behaviour between subsequent layers. In order to investigate the effects of the printing process on the mechanical properties of the elements, an experimental test, based on a modified version of the punch-through shear test, and a numerical Finite Elements method are performed, for assessing the effect of the resting time on the inherent strength of the interfaces and validating the experimental results, respectively. The experimental campaign revealed an effective weakness surface in the interface of the different layers, highlighting the need for the interface bond characterization and modelling and the definition of opposite strategies of interlaminar reinforcement implementation. A wide range of approaches is available for reaching the aim of reinforcement in the Digital Fabrication with concrete field, which provide tensile strength, including the addition of ductile materials, such as fibres, or the installation of passive reinforcement. Nevertheless a specific focus on the enhancing the bond at this interface of 3D printed concrete elements is not available. Recently, efforts have been made to improve the bond between consecutive layers by increasing the mechanical contact between the layers (Zareiyani, B. and Khoshnevis, B., 2017) or applying a low-viscous mineral-based primer before deposition of each subsequent layer. To this scope, a reinforcing method of the cold joints is suggested and tested.

Furthermore, since the dynamic behaviour of construction materials is a crucial matter to investigate for structural engineering, the assessment of this type of



properties also on elements made of a proper cementitious material has been implemented. It is clear that structures or material requirements needs to satisfy severe dynamic scenarios which could occur during their lifetime, such as earthquake and blast events. Since the response of materials can be different in dynamic conditions from that in quasi static condition and a specific focus on the interfaces' dynamic behaviour of 3D printed concrete elements is not available in the scientific literature, detailed studies result fundamental for better understand the behavior of the 3D printed elements subjected to high dynamic loading conditions. The workflow, characterized by the different thematic macro areas dealt with in the work path, is represented in Figure 1.3.

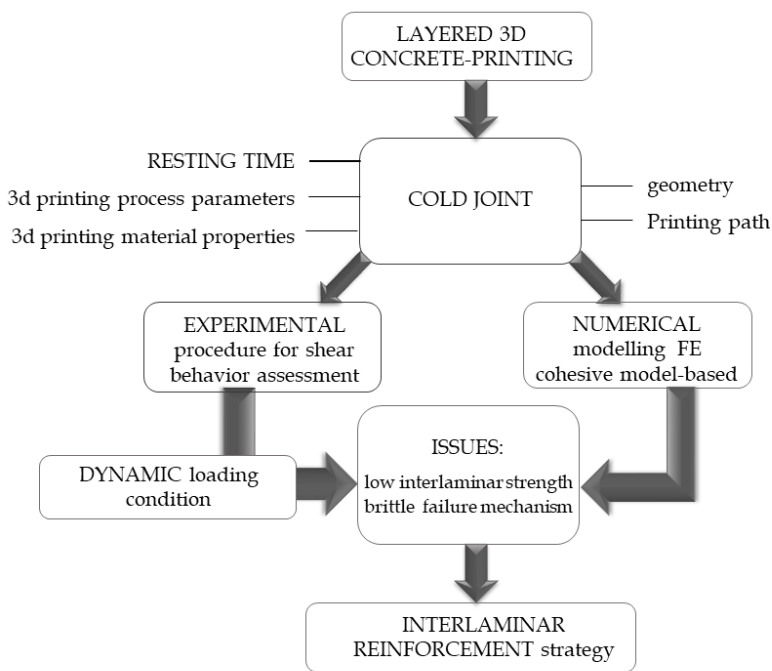


Figure 1.3. Schematic working path

Finally, in order to set this innovative technology such as 3D printing in a sustainable perspective, a printable material containing recycled carbon fibers is performed. Specifically, the process consists of recycling of carbon fibers wastes deriving from automotive industry and reusing within a digital construction system. The main goal is provide solutions to many economic and environmental impacts such as high cost of waste disposal and CO<sub>2</sub> emissions reduction and turn

carbon fibers materials at the end of their service life into novel resources and minimize waste. An experimental campaign for evaluating the mechanical performance of cement based carbon fibers is conducted.

## **1.2 Work organization and outline**

The presented work, whose motivations and main goals are reported above, is divided in six sections.

Firstly, in **Chapter 2** an overview on the main additive manufacturing etchnologies, in particular on 3D concrete printing process, is analyzed with a special focus on parameters influencing mainly this process.

**Chapter 3** describes the experimental characterization including the test specimen details, material properties, test specimen construction, test setup and instrumentation. Finally, a numerical simulation, aiming to reproduce the experimental contributions is carried out.

A detailed description of the experimental response is provided and discussed in **Chapter 4**, together with a comparison with theoretical results.

In details **Chapter 5** an explored reinforcement interlaminar method, in terms of mechanical and numerical features, providing its effectiveness and feasibility is discussed and proposed.

**Chapter 6** deals with further applications of this technology for achieving benefits in terms of mechanical material properties and environmental impact.

Finally a summary of the research work is provided, together with main conclusions and some recommendations for future research in this field.

## References

- Asprone, D., Auricchio F., Menna C., and Mercuri V. 2018. “3D Printing of Reinforced Concrete Elements: Technology and Design Approach.” *Construction and Building Materials* 165 (March): 218–31. <https://doi.org/10.1016/j.conbuildmat.2018.01.018>.
- Buswell, R. A., Leal de Silva W. R., Jones S. Z., and Dirrenberger J. 2018. “3D Printing Using Concrete Extrusion: A Roadmap for Research.” *Cement and Concrete Research*. Elsevier Ltd. <https://doi.org/10.1016/j.cemconres.2018.05.006>.
- Buswell, R. A., Soar R. C., Gibb A. G. F., and Thorpe A.. 2007. “Freeform Construction: Mega-Scale Rapid Manufacturing for Construction.” *Automation in Construction* 16 (2): 224–31. <https://doi.org/10.1016/j.autcon.2006.05.002>.
- Kim, Heechang, Park E, Kim S., Park B., Kim N., and Lee S. 2017. “Experimental Study on Mechanical Properties of Single- and Dual-Material 3D Printed Products.” *Procedia Manufacturing* 10: 887–97. <https://doi.org/10.1016/j.promfg.2017.07.076>.
- Laplume, A., Anzalone G. C, and Pearce J. M. n.d. “Open-Source, Self-Replicating 3-D Printer Factory for Small-Business Manufacturing.” *The International Journal of Advanced Manufacturing Technology*. <https://doi.org/10.1007/s00170-015-7970-9>.
- Le, T. T., Austin S. A., Lim S., Buswell R. A., Gibb A. G.F, and Thorpe T.. 2012. “Mix Design and Fresh Properties for High-Performance Printing Concrete.” *Materials and Structures/Materiaux et Constructions* 45 (8): 1221–32. <https://doi.org/10.1617/s11527-012-9828-z>.
- Le, T. T., Austin S. A., Lim S., Buswell R. A., Law R., Gibb A.G.F., and Thorpe T.. 2012. “Hardened Properties of High-Performance Printing Concrete.” *Cement and Concrete Research* 42 (3): 558–66. <https://doi.org/10.1016/j.cemconres.2011.12.003>.
- Nerella V., and Mechtcherine V., 2017b. “MICRO-AND MACROSCOPIC INVESTIGATIONS ON THE INTERFACE BETWEEN LAYERS OF 3D-PRINTED CEMENTITIOUS ELEMENTS.” <https://www.researchgate.net/publication/319504633>.
- Panda B., Paul S.C., Hui L.J., Tay Y.W.D., Tan M.J., 2017. “Additive Manufacturing of Geopolymer for Sustainable Built Environment Additive Manufacturing of Geopolymer for Sustainable Built Environment.” <https://doi.org/10.1016/j.jclepro.2017.08.165>.
- Panda, B, Paul S.C., Mohamed N. A. N, Tay Y W, and Tan M J. 2017. “Measurement of Tensile Bond Strength of 3D Printed Geopolymer Mortar.” *Measurement* 113: 108–16. <https://doi.org/10.1016/j.measurement.2017.08.051>.
- Panda, B., Paul S.C., and Tan M. J.. 2017. “Anisotropic Mechanical Performance of 3D Printed Fiber Reinforced Sustainable Construction Material.” *Materials Letters* 209 (December): 146–49. <https://doi.org/10.1016/j.matlet.2017.07.123>.

- Paul SC, Tay YWD, Panda B, Tan MJ, 2017. “Fresh and Hardened Properties of 3D Printable Cementitious Materials for Building and Construction Fresh and Hardened Properties of 3D Printable Cementitious Materials for Building and Construction.” *Archives of Civil and Mechanical Engineering* 18 (1): 311–19. <https://doi.org/10.1016/j.acme.2017.02.008>.
- Paul S.C., Tay Y W, Panda, B, and Tan M J. 2018. “Fresh and Hardened Properties of 3D Printable Cementitious Materials for Building and Construction.” *Archives of Civil and Mechanical Engineering* 18 (1): 311–19. <https://doi.org/10.1016/j.acme.2017.02.008>.
- Perkins, I., and Skitmore M.. 2015. “Three-Dimensional Printing in the Construction Industry: A Review.” *International Journal of Construction Management*. Taylor and Francis Ltd. <https://doi.org/10.1080/15623599.2015.1012136>.
- Rüßmann, M., Lorenz M., Gerbert P., Waldner M., Justus J., Engel P., and Harnisch M.. 2015. “Industry 4.0: The Future of Productivity and Growth in Manufacturing Industries.”
- Sasson, A., and Johnson J. C.. 2016. “The 3D Printing Order: Variability, Supercenters and Supply Chain Reconfigurations.” *International Journal of Physical Distribution and Logistics Management* 46 (1): 82–94. <https://doi.org/10.1108/IJPDLM-10-2015-0257>.
- Thompson, M. K., Moroni G., Vaneker T., Fadel G., Campbell R. I., Gibson I., Bernard A., et al. 2016. “Design for Additive Manufacturing: Trends, Opportunities, Considerations, and Constraints.” *CIRP Annals - Manufacturing Technology* 65 (2): 737–60. <https://doi.org/10.1016/j.cirp.2016.05.004>.
- Valkenaers, H., Jansen D., Voet A., Van Gysel A., and Ferraris E.. 2014. “Additive Manufacturing for Concrete: A 3D Printing Principle.” <https://lirias.kuleuven.be/1461285?limo=0>.
- Wangler, T., Lloret E., Reiter L., Hack N., Gramazio F., Kohler M., Bernhard M., et al. 2016. “Digital Concrete: Opportunities and Challenges.” *RILEM Technical Letters* 1 (October): 67. <https://doi.org/10.21809/rilemtechlett.2016.16>.
- Wolfs, B. and Salet, 2019. “Hardened Properties of 3D Printed Concrete: The Influence of Process Parameters on Interlayer Adhesion.” *Cement and Concrete Research* 119 (May): 132–40. <https://doi.org/10.1016/j.cemconres.2019.02.017>.
- Zareiyan, B., and Khoshnevis B.. 2017. “Effects of Interlocking on Interlayer Adhesion and Strength of Structures in 3D Printing of Concrete.” *Automation in Construction* 83 (August): 212–21. <https://doi.org/10.1016/j.autcon.2017.08.019>.
- Zawadzki, P., and Zywicki K.. 2016. “Smart Product Design and Production Control for Effective Mass Customization in the Industry 4.0 Concept.” *Management and Production Engineering Review* 7 (3): 105–12. <https://doi.org/10.1515/mper-2016-0030>.

## Chapter 2

# 3D CONCRETE PRINTING: A NEW CHALLENGE FOR CONSTRUCTION INDUSTRY

In this chapter, a detailed description of the 3D printing for construction industry is carried out. The first section reviews current main approaches on 3D printing technology, with a special focus on 3D concrete printing. A brief examination on the history of the use of 3-D printing and on the process that unites the various technologies used in the construction sector is discussed.

The second part of the chapter provides a structured insight into the several technological and technical issues. First, the main requirements of the entire 3D printing process are recalled and discussed. Specifically, a state-of-the-art review that can be readily evidenced and related to key areas of research, identifying the interdependent factors effecting, and effected by, the mechanics and control of the process. Finally, the focal point related to anisotropic behavior of the elements produced by 3D printing process is described. The study on the effect of interlocking on overall structural performance, as main consequence of anisotropy of elements, will be applied in next chapters in different approaches, and with the addition of new proposals.

## 2.1 History of the use of 3D printing processes

3D printing has a rich history. It started from an imperfect machine and ended up into something that can bring to life anything you have in mind.

Traditionally, the use of 3D printing was limited to the manufacturing sector, for fabricating prototypes with low production volumes, small part sizes and complex designs (Berman and Zarb, 2012). This is the reason why the 3D printing technology was usually referred to as Rapid Prototyping (RP) technology during that time. The first 3D printer, using stereolithography technology, was developed by Charles Hull in 1986 (Hull, 1986). This 3D printing technique referred to a method of printing objects layer by layer using a process in which lasers selectively caused chains of molecules to link together, forming polymers.

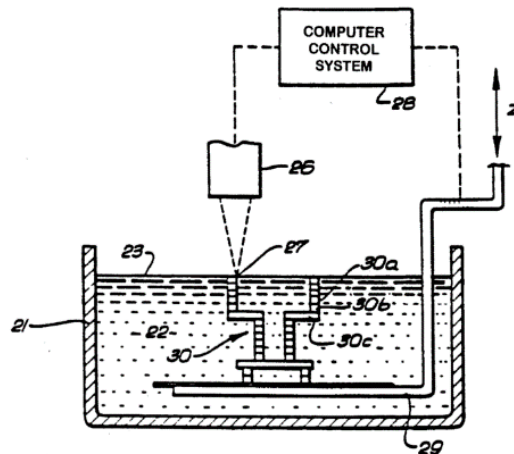


Figure 2.1. First stereolithography apparatus - a 3D printer (Hull, 1986)

In the following years, other RP technologies have also been introduced into market, such as, for example, Selective Laser Sintering (SLS) and Fused Deposition Modeling (FDM) 3D printing processes, introduced into the market in 1989, which used a laser and a liquid resin as a power source to form 3D objects, respectively. Later, in the 1996 Arthur et al. (Arthur et al., 1996) used RP technology to produce electrical discharge machining electrodes. The technology continued to play an important role in the manufacturing industry in the 21<sup>st</sup> century. In fact, Vinodh et al. (Vinodh et al. 2009) investigated the adoption of 3D printer to produce the prototype of a knob of an electronics switch.

Despite the use of RP technologies was constantly expanding, there were a few attempts to demonstrate the applicability of the technologies in the construction industry, by using construction-related materials. For example, Hinczewski et al. (Hinczewski et al., 1998) studied the possibility of using stereolithography to produce ceramic three-dimensional parts. A complex ceramic part was produced using stereolithography although the mechanical properties of the part were not optimized. Similarly, Khoshnevis et al. (Khoshnevis et al., 2001) used contour crafting and demonstrated that it could be used to produce plaster part if forced drying by heating was adopted. The research team at Loughborough University has taken an initiative to develop a 3D concrete printing process that can produce freeform building element. These pilot studies demonstrated that 3D printing technologies could be used to produce construction components as long as appropriate quality control strategies were adopted.

## **2.2 3D printing in Concrete Industry**

Additive manufacturing methods, such as three-dimensional printing, have been the potential to address different challenges posed by concrete construction. These technologies have been explored for the production of concrete since the mid-1990s, in which a variety of deposition strategies, robots, printer heads and materials have been used.

A graphical impression of the development of 3D printing in the construction industry has been given by Langenberg (2015), by collecting all projects in the field of 3D printing related to construction in a database and plotting them on a time line relating them to a location on the world map, in order to show the amount of projects increasing in time and the hot-spots where the developments take place.

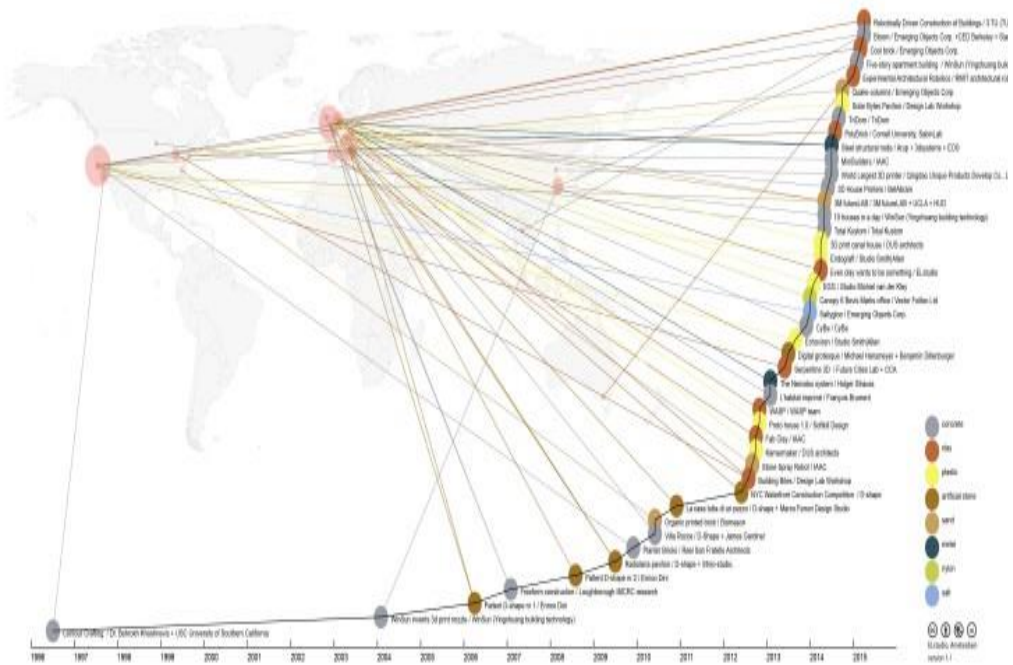


Figure 2.2. Mapping 20 years of 3D printing in Construction, from 1906 to 2015 (Langenberg, 2015)

Developments started in the mid-1990s. The first attempt at using cement based materials in an approach to AM was suggested by Pegna (Pegna 1997); then in California, USA, Khoshnevis introduced a technique termed Counter Crafting, as shown in Figure 2.3c (Khoshnevis and Dutton 1998; Khoshnevis 2004), Khoshnevis et al. 2006). This involves the deposition of layers of continuous concrete-like filament on top of each other. Until approximately 2012, developments have been steady. Besides Khoshnevis, pioneering work was done by the University of Loughborough (Le et al., 2012a; Le et al., 2012b; Lim et al., 2011, 2012; Fig.2.3b), Shanghai based contractor Winsun, and the company Total Kustom in Minnesota, USA. An alternative to working with single, large robots was introduced by the Institute of Advanced Architecture of Catalonia in 2014 (IAAC 2014; Figure 2.3a).





Figure 2.3. Images of AMoC by various institutes: (a) Minibuilders (Institute of Advanced Architecture of Catalonia), (b) Concrete Printing (University of Loughborough), (c) Contour Crafting (University of Southern California), and (d) D-shape.

An altogether different approach, similar to StereoLithography, was adopted by Enrico Dini, named DShape (Figure 2.3 (d); Colla and Dini 2013, Cesaretti et al., 2014, Dhape.com 2016). He filed his first patent in 2006 and has been developing a range of objects since. Recently, other works (Wolfs, Salet and Hendriks, 2015; Wu, Wang and Wang, 2016) are contributing to the technology development.

Currently, the main 3D concrete printing technology in most literatures are categorized into two techniques, namely 1) Binder Jetting and 2) Material deposition method (MDM).

The basic principle of both these techniques is to build up any complex structure by adding small layers of material one over another. It begins with the creation of

a 3D computer-aided-design (CAD) model, which is sliced into several 2D layers and then printed with an assigned material in an incremental manner to obtain the prototype as described in the CAD model.

### 2.2.1. *Binder Jetting*

Binder jetting is one of the multistep AM processes originally developed at Massachusetts Institute of Technology (MIT) in the early 1990s (Meteyer et al. 2015). Even though it was developed in the 90s, it was a considerable time until its commercialization in 2010.

Binder jetting is a 3D printing process that creates objects by depositing from a print head a liquid binder layer by layer over a powder bed. Both inorganic and organic binders exist; in fact the binder is usually a liquid and the metal/ceramic is in the form of a solid powder. Binder is ejected in droplet form onto a thin layer of powder material spread on top of the build tray. This method incrementally glues 2D cross sections of the intended component to each layer of material powder (Perkins and Skitmore 2015).

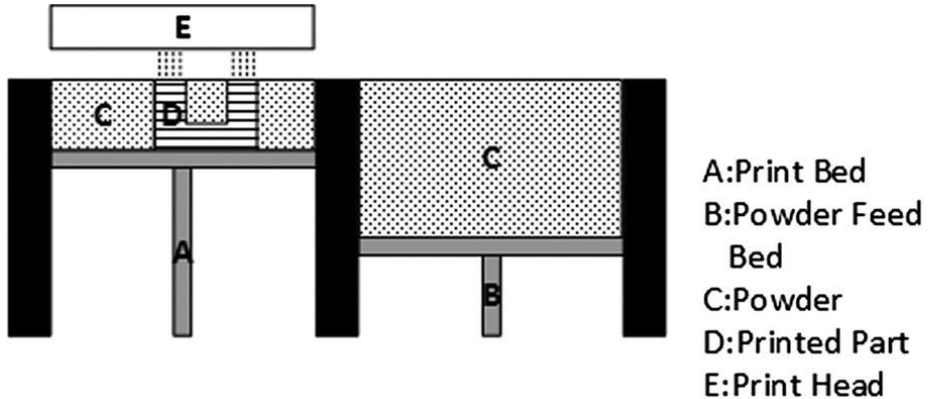


Figure 2.4. Printing system of BJ technology (Meteyer et al. 2015)

This process has been used primarily for the production of casting molds for metal parts, but recently is being investigated as a method to produce architectural elements with resolutions on the order of millimeters.

Any raw material that is not glued by the binder remains inside the constrained build container and is used to support subsequent layers. The unbound material can be removed from the print bed using a vacuum cleaner after the printing,

which can be recycled and deployed for another printing task (Khoshnevis et al. 2006).

This process can take full advantage of the almost unrestricted geometric freedom of a binder jetting printing process and combine it with the structural capabilities of concrete, by printing elements that can subsequently be assembled and infilled with a structural concrete. This method moreover encourages designs to have voids and overhanging features which enable the printing of complex geometries. It has a relatively high resolution that results in the good surface finish because of the minimal distance between layers. This layer thickness value is determined by the penetration of the binder. If the layer thickness is too large, the binder may not penetrate deep enough to glue the current and the previous layer together (Cesaretti et al., 2014). This process is iterated for building the entire part. However, the BJG process involves several post-processes that follow the printing of the parts such as curing, de-powdering, sintering, infiltration, annealing, and finishing (Wong and Hernandez 2012; Meteyer et al. 2015). These post-processes sometimes take longer time than the actual printing and may incur significant costs.

Compared to other 3D printing methods for architectural applications, binder jetting allows for a high degree of geometric freedom, as stated earlier, even allowing cantilevered or hollow parts because the unbound powder supports the part during fabrication. While parts with the structural capacity of unreinforced Portland cement can be printed again the introduction of reinforcement remains problematic. The layer height is restricted by the binding process, and determines both speed and the level of detail, and recycling of unbound cement powder may be problematic with exposure to humidity. Additionally, post -manufacture processing is often necessary, such as infiltration of epoxy or additional curing steps. The future challenge for binder jetting will be to broaden the spectrum of printable powder-binder combinations to increase the stability of the printed parts - including reinforcement -and to reach a more environmentally friendly and sustainable fabrication.

### 2.2.2. *Material deposition method (MDM)*

Similar to fused deposition modelling (FDM), in which a continuous filament of a thermoplastic polymer is used to 3D print layers of materials, material deposition method (MDM) is a 3D printing processes that successively lays material as CAD model (Panda et al. 2017). The extruded material have to support

its own weight and the weight of each subsequent layer, in order to get the final object without any deformation. The processes using MDM philosophy are:

1) **Contour crafting** is layered fabrication technology with great potential in the automated construction of whole, small structures including some of their subcomponents. The pioneer of contour crafting technology is Dr. Khoshnevis from the University of Southern California as early as 2004 (Khoshnevis 2004), with the aim of printing high-rise buildings and even houses on the moon, claiming that with this process a single house or even a whole estate of houses may be constructed in a single run with the possibility of each having a different design. In 1999, Richard J. Russell II (Russell R.J.,1999) completed his PhD dissertation on analyzing polystyrene melt flow using Contour Crafting through experimental approach. In 2002, Hongkyu Kwon (Kwon, 2002) continued the research on CC by using experimental approach for uncured ceramic material. He investigated the effect of side trowel on the capability and quality of the Contour Crafting process to fabricate 2.5D and 3D parts, and he concluded that the surface quality of the extruded part with trowels on two sides was better than a single side trowel on the exterior angle. Kwon also simulated the pattern of flow in the CC nozzle during fabrication processes with CFD software to study the effect of the pressure on the extrusion and geometry. In 2005, Dooli Hwang (Hwang, 2005) used experimental approach to study the application of Contour Crafting on a full scale concrete wall. His research showed that designing the setting time depends on time of deposition cycle, material delivery, CC machine preparation, and fabrication rate. He also added Bentonite, plastic clay, to the mix to increase the paste plasticity and decrease the water seepage. In 2012, Tony Di Carlo (Di Carlo, 2012) applied experimental and numerical techniques to analyze the structural properties of fresh concrete subject to Contour Crafting. He developed a special mortar mixture which can be safely used for layered fabrication. His proposed cementitious mixture was suitable for freeform-layered fabrication and was tested for a full-scale demonstration. Di Carlo also studied the structural properties of fresh concrete for safe layering by developing analytical and numerical tools. Contour crafting (CC) is a gantry-based system that extrudes material in a layer-by-layer manner. The key feature of CC is the use of trowels attached to the nozzle. The trowel guides the printed material to create exceptionally smooth and accurate surfaces, as shown in Figure 2.5. This trowel can be deflected at different angles (by computer control) to create various non-orthogonal structures. Such approach enables a deposition of higher layer

thickness without significantly compromising the surface finish. According to the classification of the 3D printing technologies in the world of Digital Fabrication, this method is called also as “Layered extrusion 3D printing” (Wangler et al., 2016).

This method allows the use of different materials, such as polymer, ceramic slurry, cement and also a variety of materials with large aggregates and additives like reinforcement fibers.

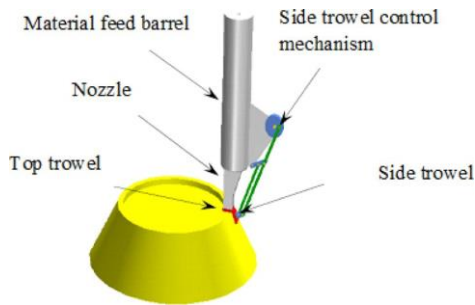


Figure 2.5. Contour crafting process (Khoshnevis 2004)



Figure 2.6. Contour Crafting example by University of Southern California

2) **Concrete Printing (CP)**, which is similar to Contour Crafting, is a new method developed at the Department of Civil and Building Engineering of the Loughborough University, UK. It is based on the concrete extrusion layer by layer following a digital model. This technique however has been developed without the trowels used in contour crafting, in order to require a smaller resolution of deposition to achieve higher 3-dimensional freedom, and to allow greater control of internal and external geometries. One of the by-products of this process is the ribbed surface finish, as the resulting surface is heavily dependent on the layer thickness. However, if a smooth finish is required, either the wet material is troweled during the building process or the printed finish is ground to a smooth

surface. This must all be completed manually because this step is not yet automated (S Lim et al. 2012). This print process doesn't require the use of labour-intensive formwork and incorporates functional voids into the structure (S Lim et al. 2011). As resulting of increasing interest of 3D concrete printing, several companies have developed different type of printers. One example is the company WinSun in Shanghai, who recently succeeded in printing full scale houses in less than 24 h by prefabricating and assembling various portions of the structure. Other examples is the company Total Kustom from architect Andrey Rudenko, who recently produced a 3D printed hotel suite in the Philippines, and the project WASP, which launched the world's biggest 3D printer, a 12 m tall hexagonal shaped structure. The Chinese company HuaShang Tengda has recently 3D printed a two-storey villa measuring 400 m<sup>2</sup> in a mere month and a half, adopting a method of erecting a steel frame on-site and printing around it. Growing research interest has led to the establishment of materials-based approaches in recently launched projects such as ConPrint3D at TU Dresden and 3D Concrete Printing at TU Eindhoven, as well as the XTreeE team in France. The printing process consists of three stages: data preparation, concrete preparation, and component printing. In the data preparation stage a component is designed as a 3D CAD model, then converted to an STL file format and sliced with a desired layer depth. The printing path for each layer is then generated to create a G-Code file for printing. Concrete preparation involves mixing and placing it into the container. Once the fresh concrete has been placed into the container, it can be conveyed smoothly through the pump-pipe-nozzle system to print out selfcompacting concrete filaments, which can build layer-by-layer structural components. The schematic in Figure 2.7 shows the delivery system of the concrete printing process.

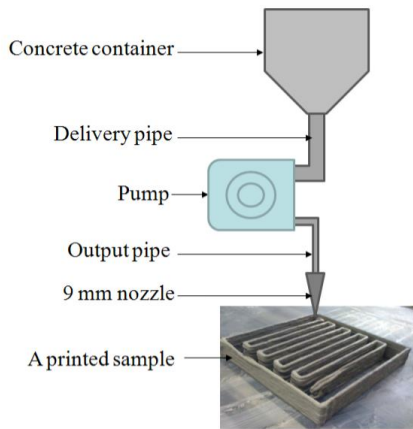


Figure 2.7. Schematic of concrete delivery system (Le TT. et al., 2012)

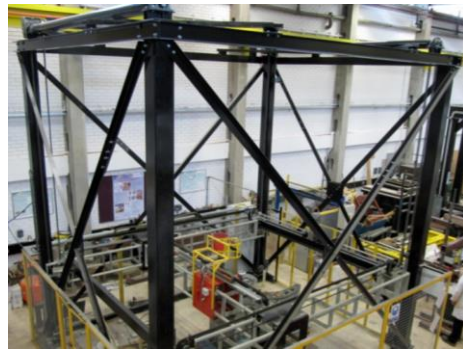


Figure 2.8. Concrete Printing by the University of Loughborough (Lim et al., 2011)

## 2.3 3D concrete printing parameters

The typical 3D concrete printing (3DCP) process for the construction industry, as widely above-mentioned, is explained graphically in the following Figure. The whole 3D printing process follows two main ways, which can be named as a software segment (left side of Figure 2.9) and a hardware segment (right side of Figure 2.9). At first, a 3D software such as AutoCAD or Solid Works is used to model the objects, then it is exported to another software for slicing (define the layer dimension).

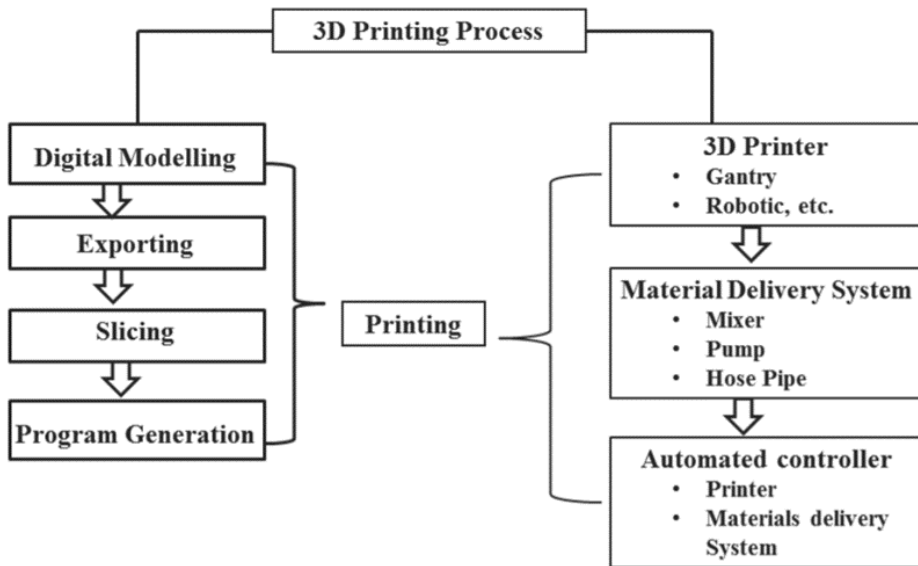


Figure 2.9. The process of 3D printing for construction industry (Paul et al. 2017)

Thereafter, a program file in the form of G-code is generated for the whole object for the printer to read and perform the job as shown in Figure 2.9. In the hardware segment, an integrated printer (either gantry or robotic) with material delivery system that is connected with a pump and hose pipe are required to deliver the material to the nozzle orifice/head, which is connected at the end part of the hosepipe to deposit the material in layer by layer. A controller is also required to control the printer and pump according to the design (shape, size, etc.) of the printed object (S. Paul et al. 2017). More details on 3DCP process are presented in several research works, developed by Bos et al. (Bos et al. 2016), Wolfs (Wolfs, 2015) and Lim et al. (Lim et al. 2011).

While the interest on 3D printing is growing rapidly, however, there are still some concerns about the application of this technology on concrete elements, related mainly to the manufacturing process and to the nature of the cementitious material.

Firstly, the control of the material properties at the fresh state, i.e. the rheological properties, results a critical milestone for the structural stability of the final 3D concrete elements (Valkenaers et al. 2014; S. Paul et al. 2017; Wangler et al. 2016). It is however the hardened properties and the conformity to design geometry to give a value to the manufacturing component (Buswell et al. 2018).



Another factors influencing significantly the objects quality are the printing parameters, such as the printing machine, the printing speed, the nozzle design.

The most important awareness is the multi-parameter interdependency of the main components of the 3DCP system (material, printer, and geometry). Each of these components constitutes a range of parameters and variables (Figure 2.10) and creates some relations to be understood and quantified.

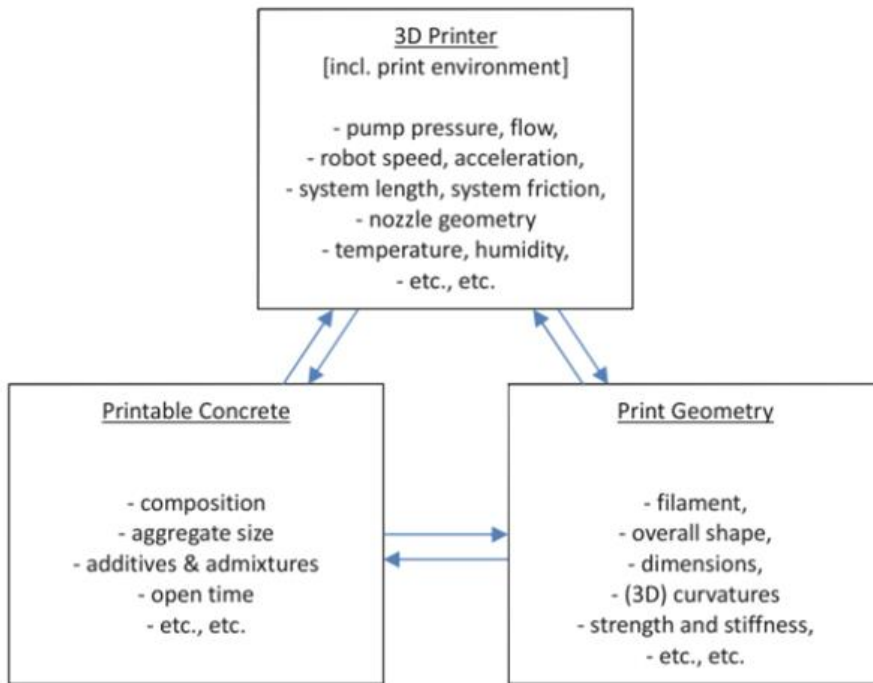


Figure 2.10. Printing process parameters (Salet et al. 2018)

In designing a concrete mix for 3D concrete printing, it is important to ensure that it meets different performance requirements. Therefore, the printing machine, on one hand, and the design of the concrete mix, on the other, must be complementary. In general, digital fabrication with concrete introduces much more stringent requests in terms of material control than for ordinary concrete. So controlling the rheological and mechanical properties becomes more critical for successful execution.

Many papers are available concerning the optimization of mixtures in order to

make a “Printable” material. Moreover, studies have been carried out about the optimization of building rate of concrete in 3D printing (Perrot, Rangeard, and Pierre 2016), connecting the built-up process to the evolution of concrete properties through time. Another topic that is being faced by the researchers is the dependence of mechanical performances on the elements geometry (Hambach, Rutzen, and Volkmer 2019).

In order to design the optimal mix, certain target goals were set for the mix. Table 2.1 presents these goals.


Maximize compressive strength		Maximize workability
Maximize flowability in the system		Maximize buildability upon pouring
Maximize speed of concrete setting		Maintain appropriate setting rate so as to ensure bonding with the subsequent layer

Table 2.1. Mix goals (Malaeb et al. 2015)

The table presents some goals that seem to be in conflict with each other. The challenge, in fact, is in maintaining an appropriate balance of the different goals. For example, maximizing the compressive strength in the mix means minimizing the water-cement ratio, but a right water/cement (w/c) ratio must be maintained to guarantee workability of the concrete. In addition, the mix should be flowable throughout the system, yet, upon pouring, the mix must be buildable and each layer should be able to hold itself and subsequent layers. Finally, wed, the mix should setas fast as possible, but slow enough to ensure proper bonding with the successive layer.

To address these goals, specific criteria must be set. The most important aspects of the printing machine and mix are studied.

### 2.3.1. *Printing machines*

The design of the 3D printing machine, especially in relation to printing technology, is a key aspect to consider for the successful feasibility of 3D elements. The optimization of machine is strictly linked to the optimization of material, and more specifically to both fresh and printed properties of concrete mix. The most common 3D printer is made up of three fundamental components: the concrete

tank and pumping mechanism, the printing nozzle and motion control system. The process in fact involves the storing of concrete in the tank, which is pumped or rotated in order to move it to the nozzle; finally the concrete is poured out. Moreover, the machine is designed to create three-dimensional objects and so it is able to move on a tri-axial plane ( $x, y, z$ ).

A critical element influencing strongly the extruded concrete properties is the nozzle. The nozzle diameter has a direct relationship with the concrete mix properties, specifically its flowability. As the diameter size decreases, the flowability of the mix should be increased to account for it and vice versa. In addition, the nozzle has two trowels, a side and top trowel, which lag behind it. The side trowel on the outer side functions to straighten the concrete being poured as the nozzle passes by. The top trowel serves to straighten the upper surface of the concrete layer to ensure maximum buildability.

Referring to the nozzle, its speed and so the extrusion speed results one of the most important parameters to control for the assessment of the printed concrete behavior. If a large quantity of concrete is being extruded, the only way to get it chemically and mechanically sound will be to give enough time for the setting to happen. That is why such techniques traditionally exhibit slow nozzle speeds, typically around a few meters per day. On the contrary, when extruding mortar layers around 1 mm, it is preferable to keep a relatively high-flow pumping system while increasing the nozzle speed, up to several hundreds of millimetres per second. The main reason for it being that such precise printing must be as quick as possible to be implemented in the building industry.

Also the nozzle height represents a variable in the printing process investigated by several authors. The findings by Panda et al. (Panda et al. 2017) reported an element strength reduction of over 30% for increasing nozzle height, while the work of Wolfs et al. (Wolfs, Bos, and Salet 2019) found no clear relation between the height of the nozzle and the strength of the element.

Furthermore a series of parameters such as speed of concrete flow and printer head speed, nozzle section, slump and inclination of the print surface influence the deposition of a single layer. Obviously, the smaller the layer section, the more detailed a printed object can become, generally at the price of the overall print speed. When deviating from printing a straight line, that is, introducing corners, a difference in deposition rate arises between the inside of the filament (near the corner centre) and the outside, resulting in a difference in material deposition. If this difference becomes too big, this may result in tearing of the

outer edge of the filament and skewing of the section due to the deposition difference. Hence, a minimum radius of curvature should be maintained, the value of which, however, is highly dependent on the individual 3DCP parameters, including the filament section itself (a broad filament results in a larger deposition difference than a narrow one).

Another type of printer widespread in 3D concrete printing application is based on four-axis gantry. Typically, for large-scale printing, the gantry is more suitable due to its simplicity. However, for printing complex objects, the robotic printer is more practically suited due to its 6-axis rotational ability (Figure 2.11). Furthermore, the robot printers have the advantage of being more mobile/movable than gantry printers and of being able to print certain prints due to the 6-axis movement that gantry printers would have difficulties with. Gantry printers on the other hand typically have cost and stability advantages, offers the ability to make larger prints and even print entire buildings in one go (as opposed to the more limited prints of robot printers and the robot printers need for printing single elements). Gantry printers also allow for non-continuous printing, which is needed when printing entire buildings, are far easier to control and does not require highly skilled programmers.

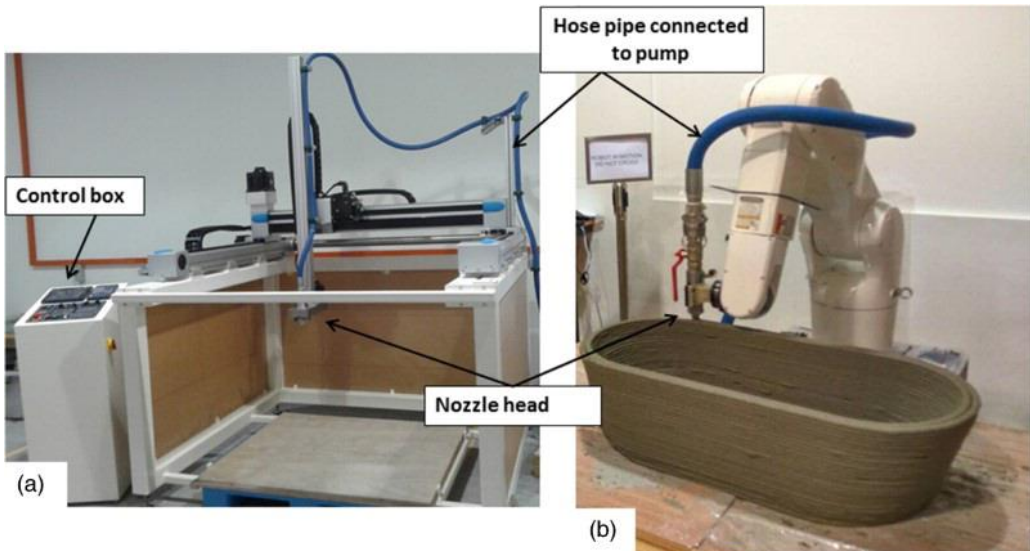


Figure 2.11. 3D concrete printers (a) four-axis gantry and (b) six-axis autonomous robotic printer.

### 2.3.2. Rheological requirements

Among all the variables involved in the printing process the first one that needs to be studied and understood is the composition of material. Indeed, the mixture composition affects the printability of the material. The term printable means that the cement paste must be able to both be extruded (i.e. workability) and sustain the required weight (i.e. buildability). In order to achieve a printable concrete the fresh state of the material must be studied; so the rheological properties must be investigated.

Concrete behaviour as liquid strongly differentiates from a liquid like water. "Liquid" is a very simple word to describe the complexity of the behaviour of concrete during its fresh state since it is made of different elements each of them of different sizes (they range from few nanometres to several millimetres) and various types (organic or mineral) suspended in water. The contribute of each concrete's component is not affected just by mix proportions but also by temperature and especially by time. Moreover, unlike water, liquid concrete doesn't follow the Newton's law of viscosity.

In order to understand the Non-Newtonian behaviour of concrete, a in-depth analysis about the Newton law of viscosity is needed, referred to the ability of a material to express a dynamic viscosity when it undergoes a shearing flow.

When the fluid undergoes a shear flow, shear stress arises. Meanwhile, since we are studying a fluid, along with the stress there is also a flow velocity  $v_x(y)$ . The ratio  $v_x(y)/y$  is defined as rate of shear deformation, whereas expressing it by differential equation it is called local shear velocity or more easily shear rate  $\dot{\gamma}$ . It is the rate of change of velocity at which one layer of fluid passes over an adjacent layer. What Newton's law states is that there is a relationship between the shear rate and the shear stress through a parameter called viscosity  $\mu_0$ .

$$\tau = \mu_0 \cdot \dot{\gamma} \quad \text{Newton's Law} \quad (1)$$

$$\dot{\gamma} = \frac{\partial v_x(y)}{\partial y} \quad \text{Shear Rate} \quad (2)$$

Moreover, in this relationship  $\mu_0$  is assumed constant, i.e. it is not function of the shear rate. This means that for  $\dot{\gamma}=0$ , shear stress is zero. Herein below in Figure the behaviour of a Newtonian fluid.

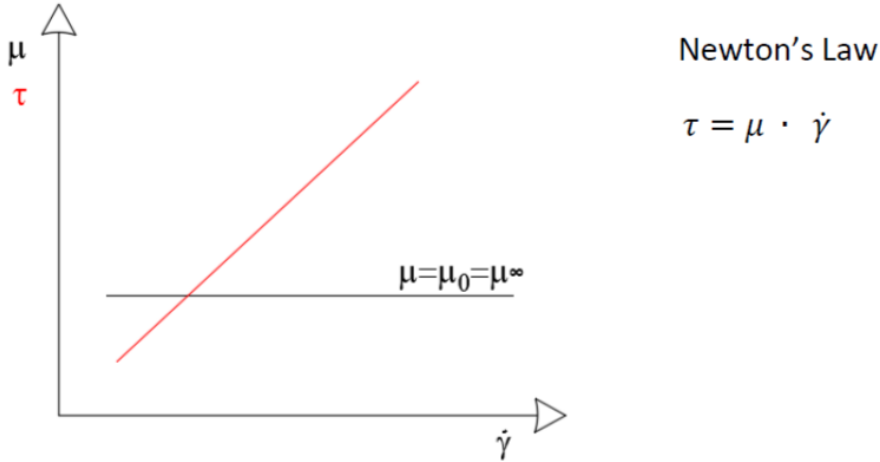


Figure 2.12. Newtonian fluid's behavior

Some other liquids (non-Newtonian) exhibit more complex behaviour which can be described by generalising the above approach, i.e. by considering the apparent viscosity ( $\eta$ ), defined as:

$$\eta = \frac{\tau}{\dot{\gamma}} \quad (3)$$

where  $\eta$  is function of shear rate  $\eta(\dot{\gamma})$ . It is worth noticing that the above relationships are valid as long as the flow is not too fast, i.e. till the Re (Reynold number) remains smaller than 1. Hence, apparent viscosity changes according to the flow characteristics. Moreover, neither non-Newtonian fluids follow just one fundamental law, instead there are many models and specific properties related to the behaviour of different materials. In fact, there are two main way by which Non-Newtonian fluids may differs from Newtonians, firstly how the apparent viscosity changes as function of the shear rate and then how it changes with time. Apparent viscosity can either raise or decrease with shear rate, having shear thickening and shear thinning respectively. Besides, given a fixed shear rate,  $\eta$  may grows with time exhibiting the so called rheopexy, otherwise if  $\eta$  decreases over time the thixotropy occurs. Once the shear rate is removed and the material is at rest it can recovery its apparent viscosity, this behaviour is still connected to thixotropy.

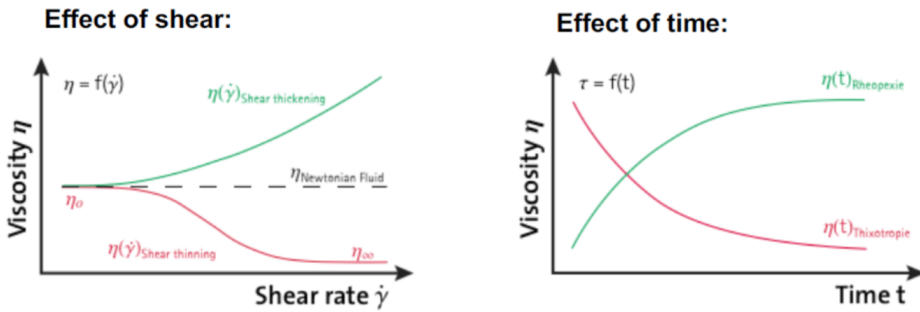


Figure 2.13 Non Newtonian fluid's behaviour as function of time and shear rate

Another significant characteristic of Non-Newtonian fluid is the yield stress ( $\tau_c$ ). There are materials that behave as solids under certain circumstances and as liquid otherwise. Actually, these materials behave as a solid as long as the applied stress is less than a critical value, once they undergo a bigger stress they begin showing a liquid behavior (Figure 2.14).

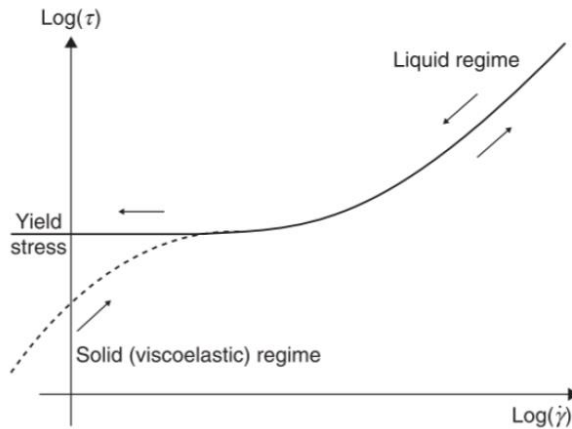


Figure 2.14 Yield stress of non-Newtonian fluids (Roussel N. 2012)

Over the years many formulations have been proposed to model the yield stress as well as the two-fold nature i.e. liquid and solid of such materials. Among the available formulations, the one that better matches to the real behaviour of concrete is the Bingham Model (Figure 2.15).

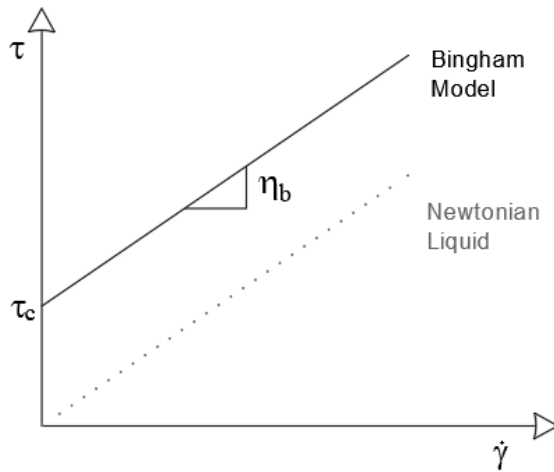


Figure 2.15 Bingham Model

Since concrete is a thixotropic material, it changes its state over a rest time which affects the critical stress at the same way that time influences apparent viscosity of concrete. In this respect, there is a test method that uses this property to study the behaviour of fresh materials like concrete at fresh state, it is referred to as thixotropy loop (Figure 2.16).

The peculiarity of thixotropic material may be noted in the “hold” segment (Figure 2.16) in which holding a steady shear rate the viscosity decreases as well as the shear stress. Afterward, a decreasing shear rate is applied until the curve intercepts the  $\tau$  axis at a lower  $\tau_0$ . What happens then is that letting rest the material it recovers its initial critical stress up to  $\tau_{0,up}$ . Although, it's important to call attention to another fundamental process that concrete undergoes, namely hardening. The concrete curing develops over time like rheological properties do. Moreover, it's important to recall that the raising of concrete yield stress is due to two different phenomena flocculation and hydration (Roussel N. 2012).



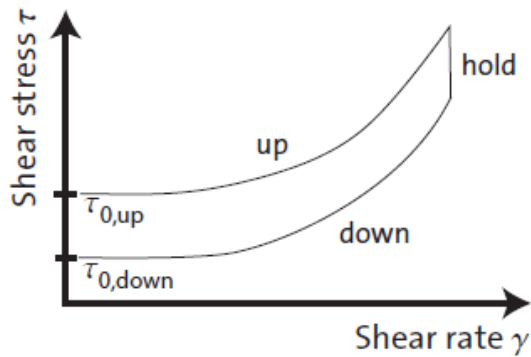


Figure 2.16 Thixotropy loop

The reason of this overview concerning rheology is pointing out the properties which have been exploited by many authors to obtain a printable concrete. Indeed, since printing process has different steps, all of which require time, e.g. time to mix the material or time to lay down different layers.

### 2.3.2.1 Workability of concrete

Cementitious materials have to meet a basic property in order to be printed, namely Workability. The latter refers to the material capability of keeping its fluid state long enough to be pumped and to flow through the nozzle, in the specific case of 3DCP. In fact, workability of concrete has been studied also for most common concrete manufacturing process, it is defined as the ability of fresh concrete mix to fill the form properly. Obviously, the starting point to achieve a workable concrete is its mixture. Generally, concrete is made of: fine or coarse aggregates bonded together with cement, latter hardens when combined with water since that an hydration process activates. Depending on aggregates size and cement/water ratio the material can perform very different behaviours, for example a low water-cement ratio yields a strong concrete.

Aggregates make up most of concrete admixture, they can be sand, natural gravel or crushed stone. The size distribution of the aggregates influences the quality of concrete, an even size distribution leads to big gaps whereas adding smaller particles tends to fill the gaps between the aggregates. Within 3DCP process the dimension of hosepipes and nozzles enforces using small aggregates size, therefore sand is the biggest aggregate usable. Workability depends on water

content, aggregates, cementitious content and age (level of hydration). However, it is not always possible reaching the desired material behaviour only by tuning the mix, therefore chemical admixtures are added in order to modify specific properties. Raising water content increases workability but at the same time may lead to segregation of aggregates with a resulting concrete having reduced quality. The major types of admixtures which aim to improve workability are superplasticizers, also known as high range water reducers. Superplasticizers are polymeric dispersants used in cementitious materials either to reduce yield stress at constant solids content or to increase the solids content at constant yield stress. These polymers are used as dispersants to avoid particle segregation and improve the flow characteristics of concrete. Their addition to concrete allows the reduction of the water to cement ratio, not affecting the workability.

Workability of concrete can be measured by concrete slump test, which follows the EN 12350-2 or ASTM C-143 test standards. It aims to measure the consistency of fresh concrete before it sets. The test is carried out using a metal mould in a conical shape, known as Abrams cone that is open at both ends. This cone is filled with fresh concrete then is refined to the top of the mould. Afterward, the mould is carefully lifted vertically upward let the concrete slumps (subsides). The slump of the concrete is measured from the top of the concrete to the level of the top of the slump cone (Figure 2.17).



Figure 2.17 Abrams Cone

The slumped concrete takes various shape and according to them the slump is termed as true slump, shear slump or collapse slump. The only meaningful shape is the true slump by which considerations about the workability of concrete may

be taken (Figure 2.18). Based on the slump the material can correspond to one of the five slump classes identified in the UNI EN 206 - 2006 and UNI 11104:2004 which go from S1 through S5.

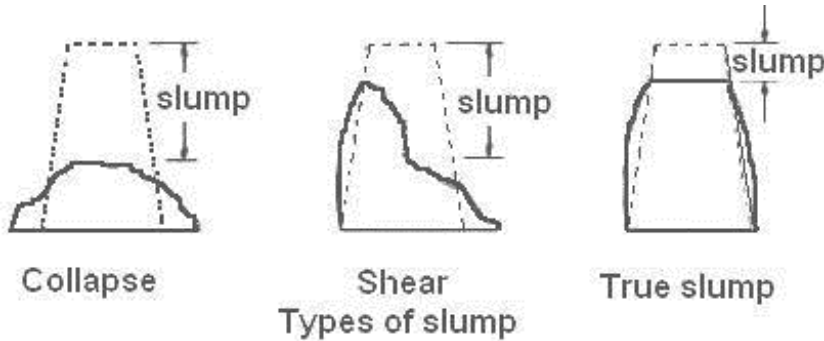


Figure 2.18 Shapes of concrete, Abrams Cone

Concerning the concrete used for printing methods, major efforts have been put trying to optimize the mixtures, because the measuring of workability through slump test is not the most appropriate method for this type of elements. Rather than seeking the best workability, researchers have instead investigated materials capable of expressing the greater strength and stability possible and at the same time a material which was still workable. In general, the mixtures used by many authors have similarities, all of their mortar pastes don't get an high content of water. However, all of them has added a superplasticizer in order to achieve a workability that would allow the print. Most common superplasticizer used are sodium lignosulfonate (S. Paul et al. 2017) and polycarboxylate (Asprone et al. 2018). To better classify the kind of texture that a printable material assumes, it is possible to place it the S1 of the slump classes, as in the work of Asprone et al. 2018. A slump test was reported in the work of Paul et al. 2017. As outcome of such test the slump values were in range of 2-6% of total specimen height. Having a pretty firm material would induce thinking that the extrusion or the flow in general were difficult but recalling the thixotropic property of concrete it's easy to understand that with a steady shear rate applied on the material, produced by the Archimedes Screw or the pump installed, the apparent viscosity tends to diminish and so the concrete flowability is assured.

### 2.3.2.2 Buildability of concrete

Buildability refers to the ability to both remain stacked in layers after extrusion and sustain the weight of the subsequent layers that are deposited by the printing process. Material consistency plays a key role in the stability of layers. In fact, as the material comes out from the nozzle no time is elapsed, thus hardening is not started yet. Since the most used mortar is usually firm, the first printed layer has not any issue to stay in place without significant vertical strains. The problems start when the upper layers are deposited and the material beneath undergoes substantial loads. The ability of deposited layers to sustain its own weight is linked to its rheology and especially to its yield stress.

In order to ensure the element stability during the printing process, the yield stress must be to sufficient to bear this load. The yield stress of cementitious materials increases over time at rest. A formulation which describe the raising of yield stress over time has been proposed by Roussel et al. 2006 (Nicolas Roussel 2006). He proposed a thixotropy model for fresh concrete. Thixotropic behaviour of a fluid must be represented at least by an apparent viscosity, i.e.  $\eta = \tau / \dot{\gamma}$ , which depends on the state of flocculation ( $\lambda$ ). Moreover, the state of flocculation changes with time, hence along with a relationship for the shear stress the variation of flocculation must be considered.

$$\tau = f(\eta(\lambda, \dot{\gamma}), \dot{\gamma}) \quad (4)$$

$$\frac{d\lambda}{dt} = f(\lambda, \dot{\gamma}) \quad (5)$$

The general form of the model proposed by Roussel is the following:

$$\tau = (1 + \lambda)\tau_0 + k\dot{\gamma}^n \quad (6)$$

$$\frac{\partial\lambda}{\partial t} = \frac{1}{T\lambda^m} - \alpha\lambda\dot{\gamma} \quad (7)$$

where  $\lambda$  is the flocculation state of the material and  $T$ ,  $m$ ,  $n$  and  $\alpha$  are thixotropy parameters. The flocculation state depends on the flow history, when the maximum shear rate is applied,  $\lambda$  is equal to zero, then it will evolve to a positive value. Assuming that the Bingham model is sufficient for the description of a

steady state flow of fresh concrete:  $n=1$  and  $k=\eta$ . Then, assuming that the yield stress at rest increases as a linear function of time:  $m=0$ . This assumption is true for many materials and seems true for concretes (Billberg 2005). The model becomes:

$$\tau = (1 + \lambda)\tau_0 + k \dot{\gamma}^1 \quad (8)$$

$$\frac{\partial \lambda}{\partial t} = \frac{1}{T} - \alpha \lambda \dot{\gamma} \quad (9)$$

At rest, the shear rate equals to zero and the evolution of the apparent yield stress is:

$$\tau_0(t) = (1 + \lambda)\tau_0 = \tau_0 + \tau_0 \frac{1}{T} = \tau_0 + A_{thix}t \quad (10)$$

With  $A_{thix} = \frac{\tau_0}{T}$ , defined as the structuration rate, i.e. a constant rate of increase in yield stress over the time at rest.

The evolution of yield stress with time is necessary to understand if the bottom layer can sustain the upper layers. Using the thixotropy model described above is possible to know if the resting time, and the strength growing which come along with it, are enough. The study carried out by Perrot et al. 2014 (Perrot, Rangeard, and Pierre 2016) aimed to find out a formulation for a critical time, i.e. the time after which a failure may occur due to the lack of mechanical strength of the first layer, moreover a computation of the highest building rate has been done. The idea behind this paper is to compare the mechanical strength of the bottom layer with the mechanical load due to the weight of the above-deposited layers. To do this, two models are necessary, the first one which refers to the evolution of the mechanical strength (e.g. thixotropy model proposed by Roussel) and the second one which refer to the evolution in time of the mechanical load due to the building of construction. Concerning the vertical stress acting on the first deposited layer, it should increase step-by-step as new layers are deposited. Although an average building rate ( $R$ ) can be computed.

The vertical stress acting on the first layer can be written as follows:

$$\sigma_v = \rho g h(t) = \rho g R t \quad (11)$$

where  $\rho$  is the specific weight of the concrete,  $t$  is the time from the deposition

of the first layer and  $h$  is the height of the element which raises over the time. The failure of the first layer will occur when  $\sigma_v$  will equal to a critic failure stress, which is linked to the yield stress:

$$\sigma_c = \alpha_{geom} \cdot \tau_0(t) \quad (12)$$

where  $\tau_0(t)$  is the yield stress of the first deposited material and  $\alpha_{geom}$  is a geometric factor which depends on the form of the built structure.

The increase in yield stress through time is evaluated with the thixotropy model described above, therefore it is considered to be linear during the dormant period (i.e. the period during the formation of Calcium Silicate Hydrate bridges between cement grains). The dormant period is measured by measuring the time in which the heat spreading is constant (Figure 2.19).

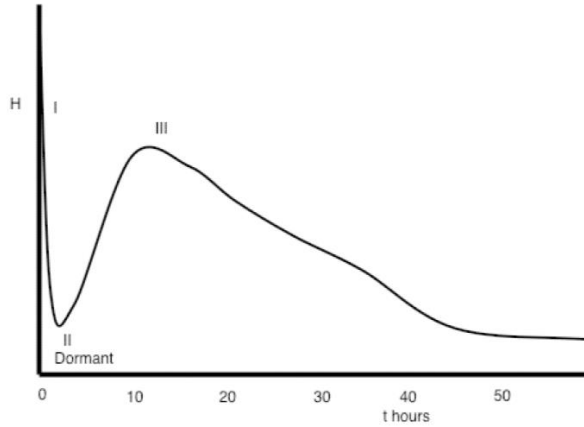


Figure 2.19 Heat spreading through time

After this linear increasing period which last up to 60 min, the rate of yield stress accelerates. This means that a linear increasing of yield stress would not be suitable from the end of the dormant period on. Other models than that proposed by Roussel are reported, like the exponential one proposed in the work of Perrot et al. (Perrot, Rangeard, and Pierre 2016) which is described below:

$$\tau_0(t) = A_{thix} \tau_c \left( e^{\frac{t_{rest}}{t_c}} - 1 \right) + \tau_0 \quad (13)$$

where  $t_c$  is a characteristic time used to obtain the best fit with experimental results.

In order to validate the proposed model, a rheometer was used. Hence, measurements of the yield stress of the material has been done every 10 minutes. Then, the experimental outcomes and the prediction of the yield stress increase, computed with both linear and exponential models, are plotted (Figure 2.20):

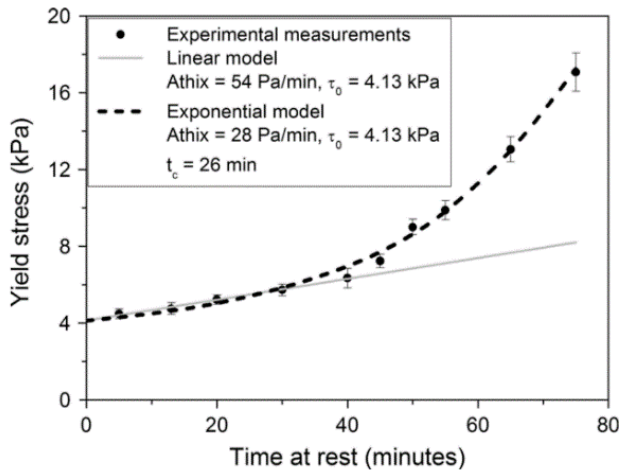


Figure 2.20 Yield stress evolution over time. Experimental results comparison between the models by Perret et al. and Roussel

In Figure 2.20 is showed how the linear model doesn't match the experimental point after a characteristic time  $t_c$ . More interesting though is the test carried out aimed to find out the critical time after which the failure of the first deposited layer occurs, with a given building rate ( $R$ ).

In order to simulate the loading to layer by layer construction a sample of material has been placed between two plates. Then the material was loaded by the upper plate. The upper plate was then loaded in 1.5 N increments. Different tests with different time gaps, which ranged from 11 to 60 second, were carried out. Loading has gone on until the sample plastically deformed, which correspond to the failure of such material. In Figure 2.21 the test's setup is shown:

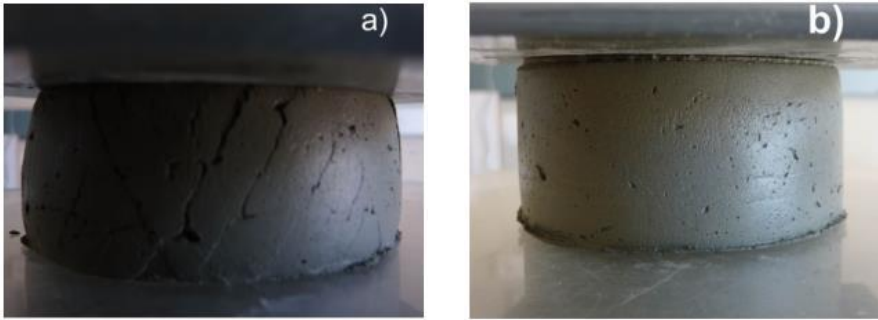


Figure 2.21 a) Fracture occurrence for a test carried out with time gap of 17 s; b) Sample after the test carried out with a time gap of 60 s

What has been noted is that changing the building rate, i.e. changing the time gap between two load increments, the failure occurs at different load and at different stresses (Figure 2.21). Increasing the building rate the material has less time to develop its yield stress whereas if the building rate decreases enough the vertical stress grows slower than the yield stress, consequently no fractures occur.

This test well depicts how the structural built-up of concrete can be used to increase the buildability of a 3D printed element.

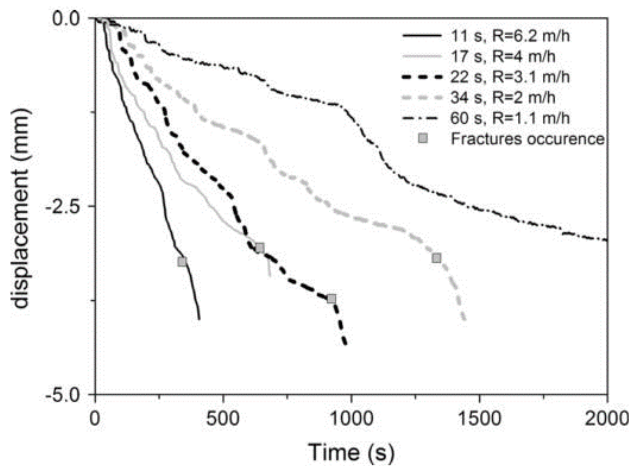


Figure 2.22 Displacement of the upper plate vs time

Beside the experimental results, an analytic formulation aimed of predicting the failure occurrence depending on time and building rate would be very useful to design a printing process being sure that no issues relate to buildability will occur.



Failures occur when vertical stress equals critical stress, using the linear model for the yield stress it is possible to write the following equations:

$$\sigma_v(t) = \sigma_c(t) \quad (14)$$

$$\rho g R t = \alpha_{geom} \cdot \tau_0 + A_{thix} t \quad (15)$$

$$t_f = \frac{\tau_0 \cdot \alpha_{geom}}{\rho g R - A_{thix}} \quad (16)$$

where  $t_f$  is the failure time, namely the time at which the first layer fails. This formulation can be used to find the perfect building rate which does not lead to the element failure. The reliability of the formulation has been confirmed by comparing the failure prediction to the failure detection (Figure 2.23).

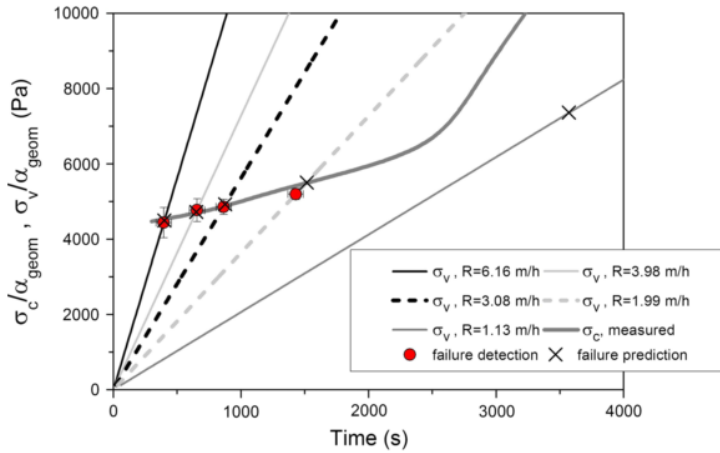


Figure 2.23 Comparison between critical stress and vertical stress history (Perrot, Rangeard, and Pierre 2016)

The study carried out by Perrot et al. (Perrot, Rangeard, and Pierre 2016) points out the importance of lower building rate in order to avoid the element failure. However, it is not so immediate designing a printing process based on the building rate since it is a global parameter. What would be very effective is to assess a range of velocity in which the elements stability is assured. A maximum velocity may be estimate using again the structural built-up of concrete, as Wangler et al. (Wangler et al. 2016) described in his work. Let's start from the

initial yield stress  $\tau_0$  which may be capable of sustain its own weight. Calling  $h$  the height of the first deposited layer the vertical stress acting on the first layer due to its own weight is:

$$\sigma_{v,0} = \rho gh \quad (17)$$

then using the Von Mises in order to have the shear stress, i.e. the initial yield stress takes the following form:

$$\tau_0 = \frac{\rho gh}{\sqrt{3}} \quad (18)$$

Recalling the structuration rate ( $A_{thix}$ ) and naming  $t_{H,n}$  the minimum time needed to reach the final layer, producing an element of height  $H_m$  :

$$A_{thix} = \frac{\tau_0}{\tau} = \frac{\rho g H_m}{\sqrt{3} t_{H,min}} = \frac{\rho gh}{\sqrt{3} t_{h,min}} \quad (19)$$

$t_{h,n}$  in the minimum time requires to produce one layer. Hence, it is possible to express  $t_{h,n}$  as function of  $A_{thix}$  which is basically constant before onset of hydration.

$$t_{h,min} = \frac{\rho gh}{\sqrt{3} A_{thix}} \quad (20)$$

This formulation can be used to evaluate the maximum horizontal velocity  $V$ , above which structural build-up would not be fast enough to sustain the deposited material:

$$V < \frac{\sqrt{3} L A_{thix}}{\rho gh} \quad (21)$$

where  $L$  is the length of the layer.

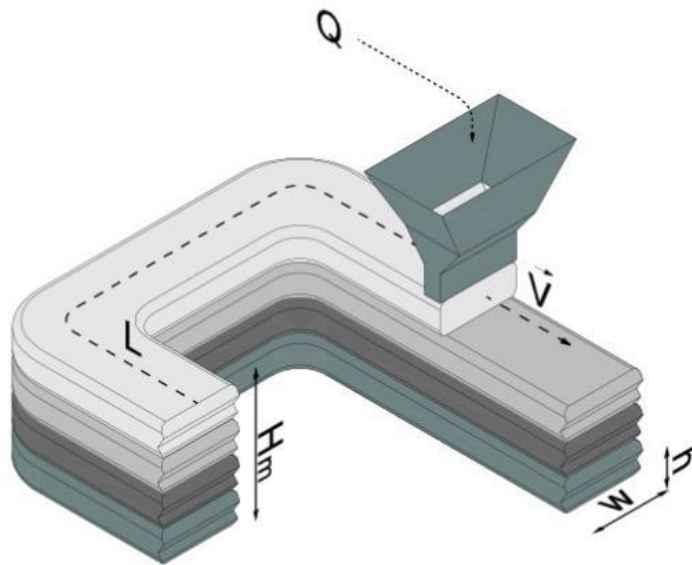


Figure 2.24 Schematic of layered extrusion process with concrete (Wangler et al. 2016). A digitally controlled extrusion head moves at velocity  $V$ , creating layers of individual height  $h$  and width  $w$ . The overall height  $H_m$  is dependent on the velocity and contour length  $L$ .

It is possible to manage the buildability by reducing the speed of the printer. As shown above, this maximum velocity achievable is function of the rheological properties of the material and other parameters related to the printing process such as length and height of the layers. Thereby, this formulation is valid for every material provided that the first layer is able to support its own weight.

### 2.3.3. *Mechanical properties*

The mechanical performance of a layer-like elements such those produced by 3D printers cannot be expected be equal to casted elements. This come up from the nature of the printed elements themselves. By comparing a casted element with a printed element it appears at first sight that in the printed one there are discontinuity surfaces that somehow will affect the overall mechanical behaviour of such elements (Figure 2.25).

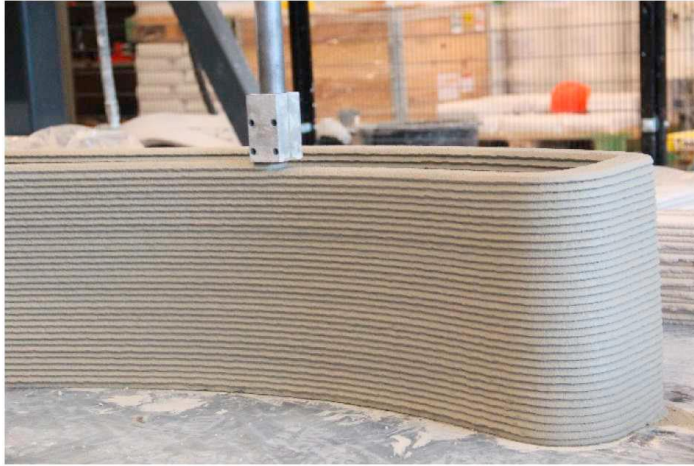


Figure 2.25 Example of 3D printed elements

### ***2.3.3.1 Hardened properties: Influence of Geometry***

One of the most critical aspects of the hardened properties is the effect of the layers on the mechanical behaviour. The printed structures have a mixed isotropic and anisotropic properties in different direction unlike cast specimens that present isotropic properties in all directions. It is expected that the material compatibility is higher in the horizontal direction, i.e. within a single layer, compared to the vertical direction, i.e. normal to the discontinuity surfaces (Van Zijl, Paul, and Tan 2016). Figure 2.26 and Figure 2.27 show the possible ways of applying load in different directions of 3D printed object. The tensile strength in the vertical direction (z direction) is related to the bond strength among the successive layers. The bond strength is related to many parameters such as material viscosity, printing time gap between the layers, contact area between the successive layers (rectangular nozzle gives more contact area than circular nozzle), etc.

In this respect, there are many ongoing researches some of them have already got some compelling results (Paul et al. 2017; Hambach, Rutzen, and Volkmer 2019; Nerella et al. 2016). The studies conducted by Paul et al. and Nerella et al. have shown how flexural and compressive strength of 3DCP is related to the printing direction.

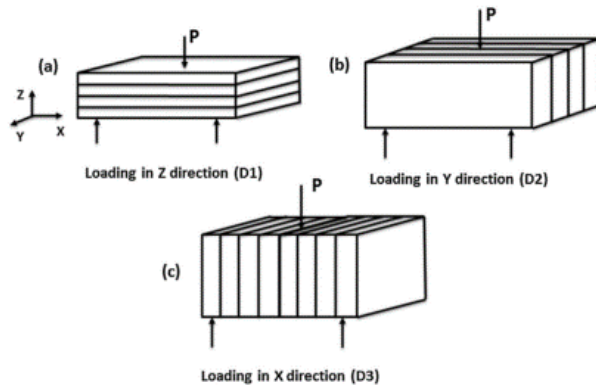


Figure 2.26. Compression loads application in printed objects related to the printing direction

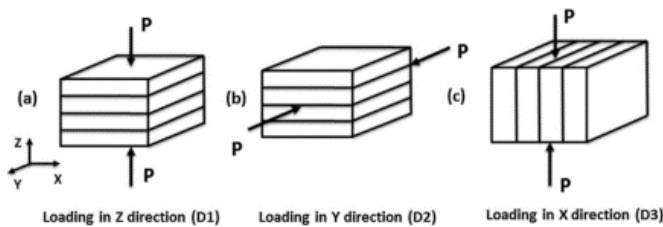


Figure 2.27. Flexural loads application in printed objects related to the printing direction

Nerella et al. have compared the compression strength of printed specimens tested in direction D1 and D3 (see Figure 2.26) with cast specimens obtaining about 14% and 10% increase respectively. In the same study, in a flexural strength test, authors have reported about 16% and 14% higher strength in printed specimens tested in directions D1 and D3 (see Figure 2.27), respectively, than in cast specimen. By testing specimens parallel to the layer deposition (see Figure 2.26a & b), Feng et al. (Feng et al. 2015) obtained higher compressive strength than when testing perpendicular to the layer depositions (see Figure 2.26c). Nerella et al. (Nerella et al. 2016) also observed similar behaviour. However, the mechanism of this strength variation, which is a function of the test direction, was not explained by the authors. Perhaps, this phenomenon is hard to explain. It is noteworthy that Feng et al. (Feng et al. 2015) heat cured their specimens and tested at the young age of 3 hours while Nerella et al. (Nerella et al. 2016) did not

mention the curing method used. In addition, the layer thickness of the printed specimens in both experiments was significantly different. The layer thickness in Nerella et al. was about 15 mm x 38 mm while Feng et al. used a thickness of 0.0875 mm. In both studies, the influence of the printing direction on mechanical properties is clearer. The compressive and flexural strengths were consistently the lowest in testing direction D3 (Figure 2.26c and Figure 2.27c). In this orientation, compressive and flexural splitting may occur along the weak joints in 3D printed concrete specimens. Finally also the funding of a further recent study developed by Paul et al. (Paul et al. 2017) showed the influence of printing direction on mechanical properties of the printed specimens. At 28 days of testing, specimens collected from the printing direction of D3 were found to have about 15% higher compression strength than specimens collected from the other directions including cast specimens. Moreover, about 10% less flexural strength was found in control specimen than the specimens collected from direction D1 and D2.

### ***2.3.3.2 Printing path***

One of the reasons why 3DPC is such an interesting technology is the fact that it gives the chance to build unique pieces without needing any formwork. It's called free-form technique indeed. Free-form in 3DCP means giving to the layers any desired shape, accordingly, beside rheology and buildability the influence of printing shape must be studied. One noteworthy study was carried out by Hambach et al. (Hambach, Rutzen, and Volkmer 2019) whose work refers exactly to the influence of print-path on mechanical performances of printed specimens. Two different print patterns, namely a parallel shaped (print path A for 3-point bending tests, print path C for uniaxial compressive strength tests) and a crosshatch shaped pattern (print path B for 3-point bending tests, print path D for uniaxial compressive strength tests) were employed (Figure 2.28) in order to investigate the influence of different print paths. For print path A and C each layer was printed identical to the layer above and beneath, for print path B and D instead, each layer was twisted by 90° respect to the close layers.

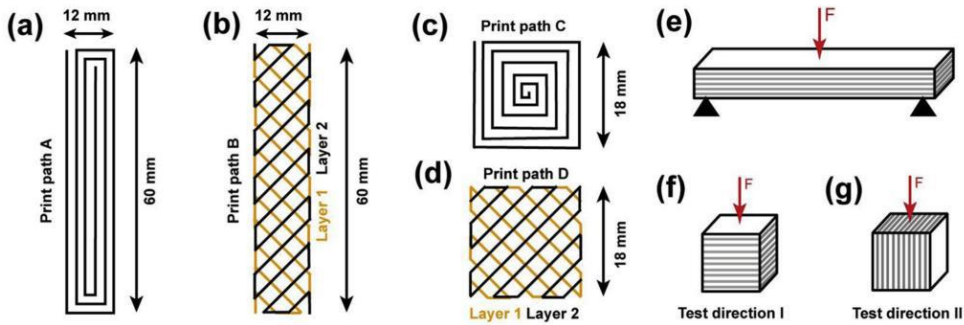


Figure 2.28. Print path adopted by Hambach et al. (Hambach, Rutzen, and Volkmer 2019)

Compression tests were performed in two directions perpendicular (test direction I) and longitudinal (test direction II) to the layer orientation whereas 3-point bending tests were performed perpendicular to layer orientation. Moreover, Hambach et al. (Hambach, Rutzen, and Volkmer 2019) carried out tests either with different types of fibres or without any fibres (plain cement paste). Based on the stress-strain curves that came out from the tests, some reflection can be done. Firstly, it is immediately clear that fibres give a massive flexural strength improvement. Furthermore, specimens with fibres showed high dependency to the print path, indeed print path A reached higher flexural strength compared to print path B (see Figure 2.29 on the left). Secondly, specimens without fibres showed no relation with print path for what concerns the 3-point bending moment, this could mean that the low tensile strength of plain cement paste does not allow the onset of more complex mechanisms of failure.

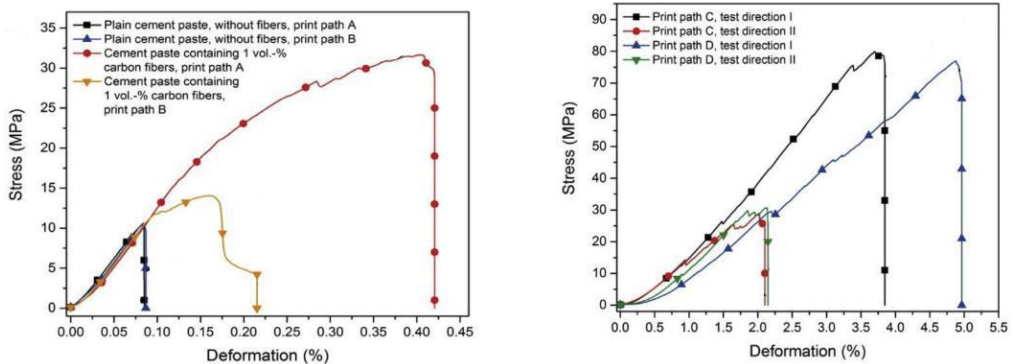


Figure 2.29 left: Flexural behavior according to the print path; right: Compressive behavior according to the print path (Hambach, Rutzen, and Volkmer 2019)

The compressive behaviour (which is shown in Figure 2.29 on the right) is very different among the tested specimens. It's not the print path which influences the most the compressive behaviour but the test direction. There is a big drop of strength, greater than 50% reduction. However, it is possible to notice a change of slope and larger max-deformation for the print path D.

Between the specimens printed with the two patterns there are slight differences in terms of mechanical behaviour, perhaps scaling up the elements size may give other results, but no studies have been done about the relationship between print-path and mechanical properties on bigger elements.

## 2.4 Research gap

The layered build-up of printed objects, the lack of compaction and the typical material compositions used in 3DCP processes set this manufacturing technology apart from others in terms of structural properties. The layered extrusion technology necessarily creates interfaces between subsequently deposited layers, namely "Cold Joint". These surfaces might create a potential zone of weakness into the printed structures and depend on different parameters, such as the time between the printings of two successive layers.

The understanding of cold joint phenomenon is way far to be complete. However, some study on SCC (self-compacting concrete) can be considered, such "Distinct-layer casting of SCC: The mechanical consequences of thixotropy" carried out by Roussel et al. (N. Roussel and Cussigh 2008). Indeed, it possible to associate a cold joint to a distinct-layer casting, which is a weak point between the first and second layer casted in a SCC technique. If a thixotropic material has long time to rest before another layer is casted its apparent yield stress could increase above a critical value, then the two layers do not mix at all. Besides some experimental test, Roussel et al. have proposed a method to estimate the critical time after which the distinct-layer casting onset occurs.

The authors assumed that the stresses generated at the interface of two layers can be decomposed into non-dependant normal stresses due to the weight of the second layer and shear stresses due to the viscous shearing generated by the second layer casting. The shear stress generated at the interface can be evaluate with a formulation similar to that of the Bingham model:

$$\tau_{xy} = \tau_0 + \eta \dot{\gamma}_{xy} \quad (22)$$



where the shear rate  $\dot{\gamma}_{xy}$  at the interface between two layers is roughly equal to the horizontal flowing speed of concrete  $V$  divided by the average thickness  $h/2$  of the second layer:

$$\tau_{xy} = \tau_0 + \eta \frac{2V}{h} \quad (23)$$

Considering the flow as extensional normal stresses can be expressed as follows:

$$\sigma_{xy} = \sigma_{yy} = -\frac{\sigma_{zz}}{2} = \frac{\rho gh}{6} \quad (24)$$

In order to mix the two layers flow has to be initiated, this happens when the normal and shear stresses are sufficient to initiate flow. Von Misès criterion has been chosen:

$$\frac{(\sigma_{xy}^2 + \sigma_{yy}^2 + \sigma_{zz}^2)}{2} + \tau_{xz}^2 = \tau_0^2(t_{rest}) \quad (25)$$

where  $\tau_0(t_{rest})$  is the apparent yield stress of the first layer after a resting time of  $t_{rest}$ . Then using the thixotropy model proposed by Roussel et al. (Roussel et al., 2012) is possible evaluate e critical time of such time, i.e.  $t_{rest}^c$  which is the time after which subsequent layers do not mix anymore.

$$\tau_0(t) = \tau_0 + A_{thix}t \quad (26)$$

$$t_{rest}^c = \frac{\sqrt{\frac{(\rho gh)^2}{12} + \left(\frac{2\eta V}{h}\right)^2}}{A_{thix}} \quad (27)$$

About printing velocity, it has to be high in order to avoid cold joint, but also lower than the maximum building speed found previously, i.e.  $V < \sqrt{3} L A_{thix} \rho g h'$ .

Using  $t_{rest}^c$  Wangler et al. have found the low bound of printing velocity:

$$V > \frac{\rho gh^2}{4\eta} \quad (28)$$

In conclusion, a velocity range can be defined, considering both buildability of material and cold joint phenomenon.

$$\frac{\rho gh^2}{4\eta} < V < \frac{\sqrt{3}LA_{thix}}{\rho gh} \quad (29)$$

Various authors studied the influence of interfaces on mechanical performances in 3D printing concrete, but its study in terms of mechanical characterization, and in particular of shear strength, is still limited.

The strong anisotropic behaviour of the concrete printed elements deriving by the occurrence of Cold Joints emphasizes the need for the interface bond characterization and modelling and the definition of apposite strategies of interlaminar reinforcement implementation.

With this in the mind, the present work focuses on the determination of mechanical properties of printed concrete elements and, in particular, on the characterization of the interface behaviour between subsequent layers. In order to investigate the effects of the printing process on the mechanical properties of the elements, an experimental and measurement procedure to assess the effectiveness of the interlayer strength of printed elements is proposed, designed and validated by means of numerical simulation.

## References

- Arthur, M., Reynolds P., and Courvalin P.. 1996. "Glycopeptide Resistance in Enterococci." *Trends in Microbiology* 4 (10): 401–7. [https://doi.org/10.1016/0966-842X\(96\)10063-9](https://doi.org/10.1016/0966-842X(96)10063-9).
- Asprone, D., Auricchio F., Menna C., and Mercuri V.. 2018. "3D Printing of Reinforced Concrete Elements: Technology and Design Approach." *Construction and Building Materials* 165 (March): 218–31. <https://doi.org/10.1016/j.conbuildmat.2018.01.018>.
- Billberg, P. 2005. "Development of SCC Static Yield Stress at Rest and Its Effect on the lateral Form Pressure." In *SCC 2005, Combining the Second North American Conference on the Design and Use of Self-Consolidating Concrete and the Fourth International RILEM Symposium on Self-Compacting Concrete, 2005*, 583–89. <http://www.divaportal.org/smash/record.jsf?pid=diva2%3A343052&dswid=171>.
- Bos, F., Wolfs R., Ahmed Z., and Salet T.. 2016. "Additive Manufacturing of Concrete in Construction: Potentials and Challenges of 3D Concrete Printing." <https://doi.org/10.1080/17452759.2016.1209867>.
- Hambach, M., Rutzen M., and Volkmer D.. 2019. "Properties of 3D-Printed Fiber-Reinforced Portland Cement Paste." In *3D Concrete Printing Technology*, 73–113. Elsevier. <https://doi.org/10.1016/B978-0-12-815481-6.00005-1>.
- Hinczewski, C., Corbel, S. and Chartier, T., Stereolithography for the fabrication of ceramic three-dimensional parts. *Rapid Prototyping J.*, 1998, 4(3), 104.
- Hull, Charles W, and Arcadia C.. 1986. "APPARATUS FOR PRODUCTION OF THREE-DIMENSIONAL OBJECTS BY STEREO THOGRAPHY."
- Hwang, D. 2005. "Experimental Study of Full Scale Concrete Wall \*construction Using Contour Crafting - ProQuest." Accessed October 19, 2019. <https://search.proquest.com/openview/353fcc9e088f3b6346eb645ed3a799ad/1?pq-origsite=gscholar&cbl=18750&diss=y>.
- Khoshnevis, B. 2004. "Automated Construction by Contour Crafting - Related Robotics and Information Technologies." In *Automation in Construction*, 13:5–19. <https://doi.org/10.1016/j.autcon.2003.08.012>.
- Khoshnevis, B., Bukkapatnam S., Kwon H., and Saito J.. 2001. "Experimental Investigation of Contour Crafting Using Ceramics Materials." <http://www.emerald-library.com/ft>.
- Khoshnevis, B., and Dutton R.. 1998. "Innovative Rapid Prototyping Process Makes Large Sized, Smooth Surfaced Complex Shapes in a Wide Variety of Materials." *Materials Technology* 13 (2): 53–56. <https://doi.org/10.1080/10667857.1998.11752766>.

- Khoshnevis, B., Hwang D., Yao K., Yeh Z., Khoshnevis B., Hwang D., Yao K., and Yeh Z.. 2006. “Mega-Scale Fabrication by Contour Crafting.” *Int. J. Industrial and Systems Engineering*. Vol. 1.
- Le, T. T., Austin S. A., Lim S., Buswell R. A., Gibb A. G.F., and Thorpe T.. 2012. “Mix Design and Fresh Properties for High-Performance Printing Concrete.” *Materials and Structures/Materiaux et Constructions* 45 (8): 1221–32. <https://doi.org/10.1617/s11527-012-9828-z>.
- Le, T. T., Austin S. A., Lim S., Buswell R. A., Law R., Gibb A. G.F., and Thorpe T.. 2012. “Hardened Properties of High-Performance Printing Concrete.” *Cement and Concrete Research* 42 (3): 558–66. <https://doi.org/10.1016/j.cemconres.2011.12.003>.
- Lim, S., Buswell R A, Le T. T., Austin S. A., Gibb A G F, and Thorpe T. 2012. “Developments in Construction-Scale Additive Manufacturing Processes.” *Automation in Construction* 21 (1): 262–68. <https://doi.org/10.1016/j.autcon.2011.06.010>.
- Lim, S., Austin S., Buswell R., Le T., Wackrow R., Gibb A., and Thorpe T.. 2011. “Development of a Viable Concrete Printing Process.” <http://www.iaarc.org/publications/fulltext/S20-3.pdf>.
- Malaeb, Z., Hachem H., Tourbah A., Maalouf T., Zarwi N. El, and Hamzeh F.. 2015. “3D Concrete Printing: Machine and Mix Design.” *International Journal of Civil Engineering and Technology* 6 (April): 14–22. [http://www.researchgate.net/profile/Farook\\_Hamzeh/publication/280488795\\_3D\\_Concrete\\_Printing\\_Machine\\_and\\_Mix\\_Design/links/55b608c308aec0e5f436d4a1.pdf](http://www.researchgate.net/profile/Farook_Hamzeh/publication/280488795_3D_Concrete_Printing_Machine_and_Mix_Design/links/55b608c308aec0e5f436d4a1.pdf).
- Meteyer, S., Xu X., Perry N., and Zhao Y. F.. 2015. “Energy Consumption Model of Binder-Jetting Additive Manufacturing Processes.” *International Journal of Production Research* 53 (23): 7005–15. <https://doi.org/10.1080/00207543.2014.937013>.
- Nerella, V. N., Krause M., Näther M., Mechtcherine V. 2016. “Studying Printability of Fresh Concrete for Formwork Free Concrete On-Site 3D Printing Technology (CONPrint3D) CONPrint3D® View Project Textile Reinforced Concrete View Project Studying Printability of Fresh Concrete for Formwork Free Concrete on-Site 3D Printing Technology (CONPrint3D).”
- Panda, B. N., Bahubalendruni R.M.V.A., Biswal B. B., and Leite M.. 2017. “A CAD-Based Approach for Measuring Volumetric Error in Layered Manufacturing.” *Proceedings of the Institution of Mechanical Engineers, Part C: Journal of Mechanical Engineering Science* 231 (13): 2398–2406. <https://doi.org/10.1177/0954406216634746>.
- Paul, S.C., D. Tay, Panda B., Tan M.J. 2017. “Fresh and Hardened Properties of 3D Printable Cementitious Materials for Building and Construction Fresh and Hardened Properties of 3D Printable Cementitious Materials for Building and Construction.” *Archives of Civil and Mechanical Engineering* 18 (1): 311–19. <https://doi.org/10.1016/j.acme.2017.02.008>.
- Pegna, J. 1997. “Exploratory Investigation of Solid Freeform Construction ?.” *Automation in Construction*. Vol. 5.

- Perkins, I., and Skitmore M.. 2015. "Three-Dimensional Printing in the Construction Industry: A Review." *International Journal of Construction Management*. Taylor and Francis Ltd. <https://doi.org/10.1080/15623599.2015.1012136>
- Perrot, A., Rangeard D., and Pierre A.. 2016. "Structural Built-up of Cement-Based Materials Used for 3D-Printing Extrusion Techniques." *Materials and Structures/Materiaux et Constructions* 49 (4): 1213–20. <https://doi.org/10.1617/s11527-015-0571-0>.
- Roussel N. 2012. "Understanding the Rheology of Concrete - Google Books." 2012. [https://books.google.it/books?hl=en&lr=&id=2NlwAgAAQBAJ&oi=fnd&pg=PP1&dq=Understanding+the+rheology+of+concrete&ots=1rWyGsjUJV&sig=r3L6rbk9AWSkLrJKT8BdQObv6ss&redir\\_esc=y#v=onepage&q=Understanding+the+rheology+of+concrete&f=false](https://books.google.it/books?hl=en&lr=&id=2NlwAgAAQBAJ&oi=fnd&pg=PP1&dq=Understanding+the+rheology+of+concrete&ots=1rWyGsjUJV&sig=r3L6rbk9AWSkLrJKT8BdQObv6ss&redir_esc=y#v=onepage&q=Understanding+the+rheology+of+concrete&f=false).
- Roussel, N., and Cussigh F.. 2008. "Distinct-Layer Casting of SCC: The Mechanical Consequences of Thixotropy." *Cement and Concrete Research* 38 (5): 624–32. <https://doi.org/10.1016/j.cemconres.2007.09.023>.
- Roussel, N. 2006. "A Thixotropy Model for Fresh Fluid Concretes: Theory, Validation and Applications." *Cement and Concrete Research* 36 (10): 1797–1806. <https://doi.org/10.1016/j.cemconres.2006.05.025>.
- Russell R.J. 1999. "An Experimental Approach to Analyzing Polystyrene Melt Flow When Troweling Using the Contour Crafting Process." Accessed October 19, 2019. <https://elibrary.ru/item.asp?id=5363425>.
- Roussel N., Ovarlez G., Garrault S., Brumaud C., 2012 The origins of thixotropy of fresh cement pastes, *Cement Concrete Res.*, 42 148-157
- Valkenaers, H., Jansen D., Voet A., Van Gysel A., and E. Ferraris. 2014. "Additive Manufacturing for Concrete: A 3D Printing Principle." <https://lirias.kuleuven.be/1461285?limo=0>.
- Vinodh, S, Sundararaj G., Devadasan S.R., Kuttalingam D., and Rajanayagam D. 2009. "Agility through Rapid Prototyping Technology in a Manufacturing Environment Using a 3D Printer." *Journal of Manufacturing Technology Management* 20 (7): 1741–79. <https://doi.org/10.1108/17410380910984267>.
- Wolfs, R. J.M., Bos F. P., and Salet T. A.M.. 2018. "Early Age Mechanical Behaviour of 3D Printed Concrete: Numerical Modelling and Experimental Testing." *Cement and Concrete Research* 106 (April): 103–16. <https://doi.org/10.1016/j.cemconres.2018.02.001>.
- Timothy W., Lloret E., Reiter L., Hack N., Gramazio F., Kohler M., Bernhard M., et al. 2016 "Digital Concrete: Opportunities and Challenges." *RILEM Technical Letters* 1 (October): 67. <https://doi.org/10.21809/rilemtechlett.2016.16>.
- Wolfs, Rob. 2015. "3D Printing of Concrete Structures." MASTER

Wolfs, R., Salet T., and Hendriks B.. 2015. “3D Printing of Sustainable Concrete Structures.”

Wong, K. V., and Hernandez A.. 2012. “A Review of Additive Manufacturing.” *ISRN Mechanical Engineering* 2012: 1–10. <https://doi.org/10.5402/2012/208760>.

Wu, J. Wang, X. Wang., 2016 “A critical review of the use of 3-D printing in the construction industry” *Autom ConStruct*, 68 (2016), pp. 21-31

van Zijl, G., Paul, S.C., and Tan, M.J., 2016. Properties of 3d printable concrete. In: *Proceeding for 2nd international conference on progress in additive manufacturing (Pro-AM)*. Singapore, 421–426

## Chapter 3

# MECHANICAL CHARACTERIZATION OF THE INTERFACES OF 3D PRINTED CONCRETE ELEMENTS

Concrete structures based on 3D printing have characterized by a form of multiple layer build-up. The material property of the 3D-printed concrete's interface between layers is expected to be far different from that of general concrete bodies since there are weak bondings. Such a difference finally affects the structural performance of concrete structures even though the interfaces are formed before initial setting of the concrete. Experimental characterization of interfaces is paramount for understanding fundamental characteristics of the behavior of entire element.

Most of early research work on concrete 3D printing was focused on the mechanical behaviour of printed concrete elements, and in particular on the compressive, flexural and tensile strength reduction in these elements characterized by multiple layers. A schematic of the existing test methods for measuring the bond strength between layers is presented in Figure 3.1.

Le et al. (Le et al. 2012) investigated compressive and flexural strengths in different loading directions and compared with that of the mould cast specimens. The mould cast specimens had high compressive and flexural strengths of about 107 N/mm<sup>2</sup> and 11 N/mm<sup>2</sup> respectively. On the other hand, the compressive and flexural strengths of printed specimens were lower and varied from 91 to 102 N/mm<sup>2</sup> and 6 to 17 N/mm<sup>2</sup> respectively, depending on the loading direction.

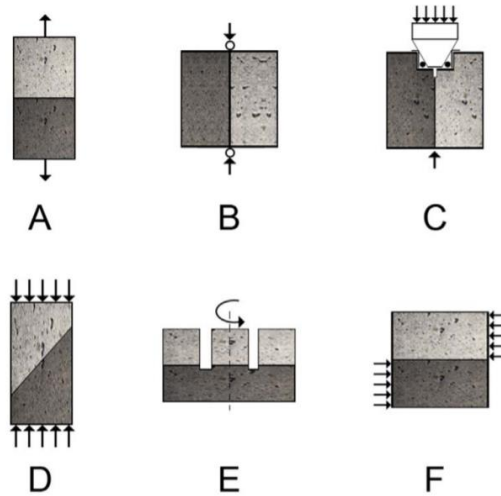


Figure 3.1. Interface bond strength test methods. A: pull-off test; B: splitting test; C: wedge splitting test; D: slant shear method; E: torsion bond strength test; F: shear strength test (Zareiyan and Khoshnevis 2017)

Panda et al. (B. Panda et al. 2017) also observed similar results when comparing the compressive and flexural strengths of 3D printed and mould cast geopolymer concrete. Apart from this, a few other researchers have also reported anisotropic behaviour for printed concrete elements. Contrary to the results obtained by Le et al., Nerella et al. (Nerella et al. 2016) found that the compressive strength of printed specimens was higher by about 10% as compared to mould cast specimens when tested along certain directions. These contradictions in the results indicate that the mechanical properties would also be dependant on the type of mix used, the printer system and the print parameters used in a particular study. For instance, Panda et al. (B Panda et al. 2017) showed that the tensile bond strength can depend on the print parameters such as time gap between two successive layers, print speed and the height from which the nozzle is depositing the layer. It was found that the bond strength decreased with increasing time gap between layers. Further, the increase in print speed or the height of the nozzle from the deposited layer also led to the decrease in the tensile bond strength. The decrease in tensile bond strength with increased time gap was also observed by a few other researchers.

Nerella et al. (Nerella and Mechtcherine, 2017b) performed mechanical tests



and SEM (scanning electron microscope) investigations of microstructure at the interface of substrate. For two printable mixtures and different interval times (1 min, 10 min and 1 day), the strength exhibited a significant reductions, which in the case of one mixture was around 50% for 1 min and over 90% for 1 day.

In the work of Wolfs et al. (R. J. M. Wolfs, Bos, and Salet, 2019) the results of an experimental campaign on the relation between 3D printing process parameters (interface interval time, nozzle height) and the compressive and tensile strength, determined through flexural and splitting tests, were presented, in three perpendicular directions. The strength reduces as the layer interval time increases. In the flexural and splitting tests, a bond strength reduction of 16% and 21% respectively was measured at the 24h interval compared to the 15s. For the layer interval times of 1h and 4h, only a minor drop in strength is observed in both tests, indicating that even if the print process is delayed for a significant period of time, the strength properties remain approximately equal, given adequate covering of the specimens during this period. Furthermore, reductions up to 72% have been reported for the interlayer interval time of 60 min by Kim et al. (Kim et al. 2017), while the results of Panda et al. indicate 75% reduction at in interval time of 20 min (B Panda et al. 2017).

On the basis of numerous research on this topic, the proposed contribution aims to characterize the cold joint from the point of view of its shear strength with varying the resting time, by means an appropriate experimental setup, discussed below.

This chapter provides details of the experimental investigation carried out at the Laboratory of the Department of Structures for Engineering and Architecture, University of Naples “Federico II” to address the main performance of 3D concrete systems.

The design procedure of test is discussed. The construction of specimens, crucial for the success of experimental tests, is described. Finally, based on visual observations and recorded test data, the performance of each test specimen is analyzed and discussed. For each specimen, the measured load-displacement relations and the stored images related to failure mechanism are presented. The damage description of specimens and their implications are discussed.

### 3.1 Experimental setup design

The weakness in bonding between layers is one of the most main cause of structural performance reduction of concrete structure made of multiple interfaces by 3D printing technology, especially with reference to shear behavior. In fact, unlike general concrete structures, printed concrete could exhibit noticeable shear critical issues, given the presence of layers which, if subjected to stresses, could generate sliding breaking, and therefore a sudden loss of resistance for the entire element or structure.

For determining the shear strength of overlay materials, several tests could be performed. In the study of Rahul et al. (Rahul et al. 2019) the interfaces were evaluated by a direct bond shear test by a fixture shown in Figure 3.2, founding that the shear strength at interface between the horizontal and vertical layers results lower by 24–25% and 22–30% respectively, compared to the shear strength of the mould cast concrete. With the interface at the centre, the cylindrical specimen is placed horizontal in the grooves of upper and lower jaws of the fixture. The jaws are then pulled apart at a constant displacement rate of 0.1 mm/minute. The failure load is divided by the cross-sectional area of the cylinder to obtain the bond shear strength. The cylindrical specimens cut out from mould cast cubes were also tested in a similar manner to obtain the shear strength of mould cast concrete.

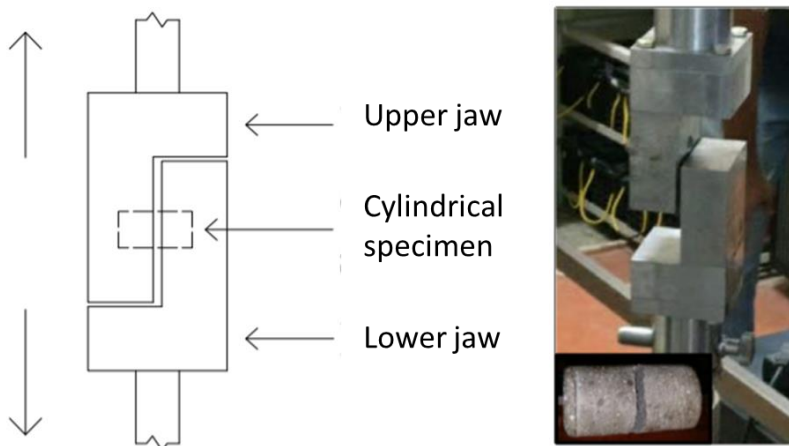


Figure 3.2. Fixture for bond shear test (Rahul et al. 2019)

### 3.1.1. Punch-through shear test

Experimental campaign to determine shear bond strength was performed considering as reference the Punch-through shear test proposed by J. Davies (Davies, Yim, and Morgan 1987). In this study a compression test on a notched specimen (Figure 3.3) and a method to read the critical energy were proposed.

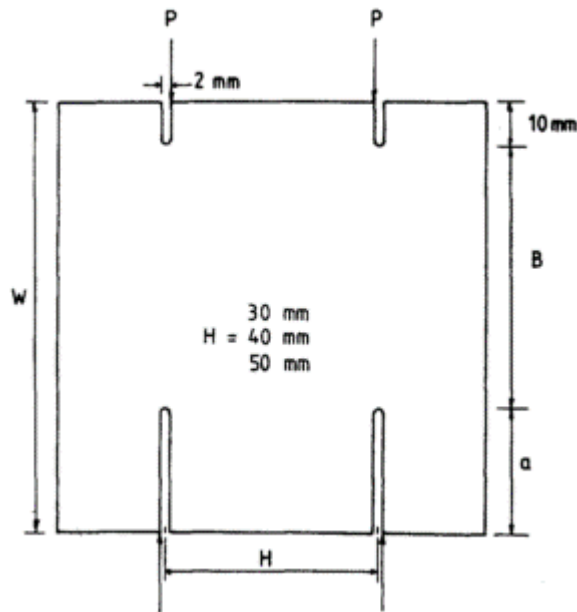


Figure 3.3. Notched cube geometry

The fracture test arrangement is shown in Figure 3.4. A simply-designed rig was used to ensure that the punch-through shear mechanism is maintained during testing. To cater for the slight difference in specimen sizes the part of the rig marked AP on the diagram was adjustable.

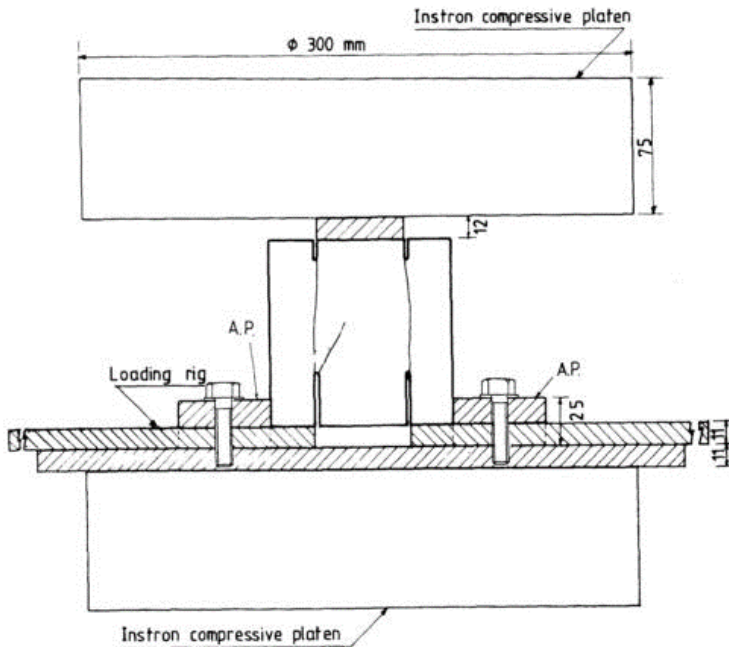


Figure 3.4. Punch-through shear test proposed by J. Davies (Davies et al. 1987)

The punch through shear test is based on the idea of forcing a sliding fracture along two identified surfaces; so its results be appropriate for the purpose of this research.

Since this test was calibrated on specimen characterized by bulk material, some modifications on the original setup and the specimen's geometry were needed due to constraints related to the printing process. In fact, by printing process, the layers thickness cannot exceed some values imposed by the size of the nozzle and the consistency of the concrete which limits the possibility of stretching. The specimens in the work of Davis et al., about the punch-through shear test were cubes of 10 cm length for each edge (see Figure 3.4).

It was outlined by the author how the ratio of the specimen's height over the specimen's width has to be 1 over 1 in order to make shear fracture the superimposed mode of fracture. Based on the length/width ratio given by Davies the geometry of the printed samples is chosen resulting a length and width of 14 cm whereas the thickness is about 5 cm.

The samples made of layers were arranged in a way that the 3 central layers are under the upper loading plate whereas the two external layers, on both side of

the sample, in contact with the bottom supports. The adopted setup is composed of a bottom steel HE 160B girder featured multiple stiffeners aim to be the piece where the setup is fixed. Above the girder two steel platens are placed and fixed by means of 4 M6 screws (with the diameter of 6mm). The distance between the edges of the two platens is 63 mm, which means that three central layers of the specimen are not supported. Even though, the dimension of three layers is 60mm, 1.5 millimetres on each side are left in order to compensate any geometric variability that may occur. Regarding to the side supports, one steel corner 5mm thick is placed on each side of the specimen and fixed on the support plates using M6 screws. The corner supports have 2 slots each in order to make them slide, this allows a certain flexibility which is necessary to use the same setup with specimen of different sizes but also to fit specimen with slightly different widths. The dimensions and the details of the setup are reported in the following figures.

Punch-through  
SET-UP

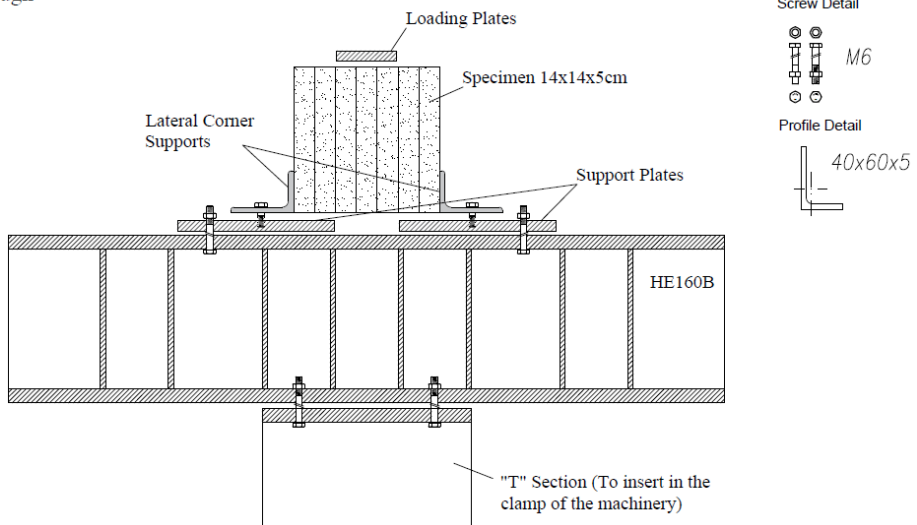


Figure 3.5. Schematic of the modified Punch-through shear setup

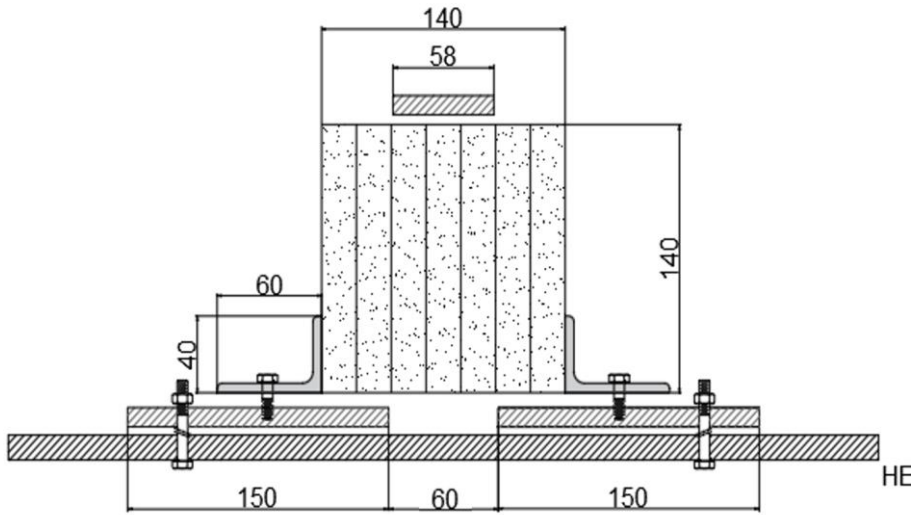


Figure 3.6. Geometry of the setup

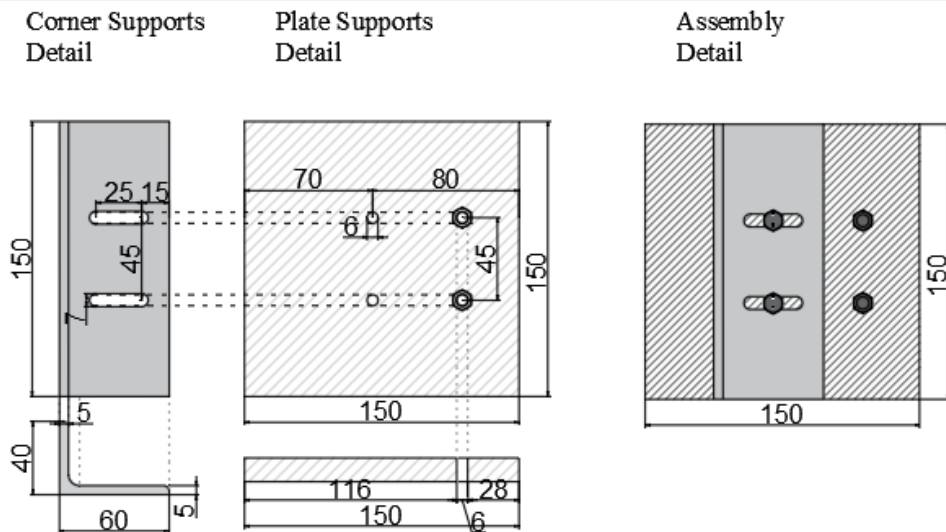


Figure 3.7. Supports details

Besides, since the surfaces of the printed elements are slightly irregular the perfect contact with the lateral supports were not assured, therefore lead sheets were placed between the lateral support and the specimen.

Concerning the loading phase, the entire setup was placed in a MTS810 (Material Test System) which is an uniaxial servo-hydraulic machine featuring a load capacity up to 500 kN.



Figure 3.8. Experimental setup

## 3.2 Experimental program

A wide experimental campaign was carried out, by using a specific material composition, printing machine and preparation of the specimen. The single properties are described below.

### 3.2.1. *Material properties*

Printing process requires a material which has specific properties. Optimal viscosity of the fresh concrete is needed to make it workable (§2.3.2.1), i.e. the material has to be capable of keeping its fluid state long enough to be pumped and to flow through the nozzle, as well as buildable (§2.3.2.2), i.e. the material must be capable to being stacked in layers. Moreover, an high strength is required to compensate for the potential weakness of the connection points between the

contiguous layers. Finally, the maximum aggregate size has to be compatible with the extrusion head whose nozzle has a diameter of 30 mm.

The cement-based mortar (Asprone et al., 2018) is characterized by a water-cement ratio of 0.38 and a maximum diameter of the aggregates of 4mm. The low water-cement ratio aims to increase the buildability of the material. The mixture contains also of polypropylene short fibres of 0.1% by weight, in order to prevent plastic shrinkage cracking in early stage of curing and after the deposition stage. Nonetheless, since the low water-cement ratio combined with the presence of the fibres in the mixture bring to an overall firm material, an admixture is needed to adjust the viscosity of such material. A polycarboxylate superplasticizer is added accordingly, achieving an optimal rheological balance, i.e. ensuring a good buildability along with a proper workability.

The cement used is an high strength Portland 42.5 R from Italcementi (“I.Work TECNOCEM - Classe 42,5 | Italcementi”) whereas the aggregate composition is given by a sand at controlled humidity (100 % moisture content) with maximum particles size lower that 4 mm mixed with a filler (size  $\leq 0.067$  mm) aimed to fill the voids and reduce the overall porosity accordingly. The leftover component of the mixture are polypropylene short fibres and polycarboxylate superplasticizer. In the following table the mix composition is reported:

<b>Materials</b>	<b>Quantity for 1 litre of mixture</b>	
Water	0,188	kg
Cement	0,490	kg
Sand(Controlled Humidity)	1,450	kg
Filler	0,101	kg
Polypropylene fibers	0,001	g
Polycarboxylate Superplasticizer	0,002	g

Table 3.1. Mixture composition

The slump class of this concrete is evaluated according to the EN 1250-2:2009 procedure (“BS EN 12350-2:2009 Testing Fresh Concrete. Slump-Test) and is equal to S1, being  $14 \pm 2$  mm the corresponding average slump measure.

The adopted material expressed a right balance between workability and



buildability; indeed, the fresh material throughout the printing process was both “liquid” enough to allow the printer to easily extrude and to deposit the material and firm enough to allow the bottom layers of concrete to underpin the subsequent concrete layers without loss in term of stability and deformations (see Figure 3.9).



Figure 3.9. Printing of concrete elements

A characterization of plain concrete, which makes up the layers of the printed elements, is necessary for knowing the uniaxial compressive and tensile strength as well as the overall nonlinear behaviour of material. For this reason three point bending test and uniaxial compression test were performed.

A three point bending test was carried out according to the European standard procedure (UNI EN 22768-1) aimed to obtain the flexural strength of plain concrete. The specimens are prisms of 40 x 40 x 160 mm dimensions which were prepared into an assembled mould frame made of steel. Here below a schematic of the mould frame is shown:

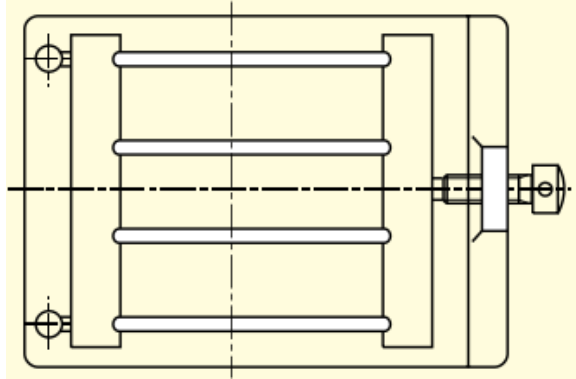


Figure 3.10. Schematic of mould frame for 160x40x40 mm prisms

The test setup is made of two bottom supports and one load head on the upper side (Figure 3.11).



Figure 3.11. Three point bending test setup

Applying an increasing load through the load head the specimen accumulates inner stresses up to the failure which corresponds to the attaining of the maximum tensile strength in the middle span cross section. Once the test was performed, the prism showed a neat fracture underneath the load head, forming

two separated pieces of 40 x 40 x 80 mm.

The flexural strength was computer by knowing the bending moment diagram which occurs in a such test setup. Indeed, a three point bending test can be schematized as a simple supported beam with concentrated load in the middle span that presents a bi-triangular bending moment diagram is generated (Figure 3.12).

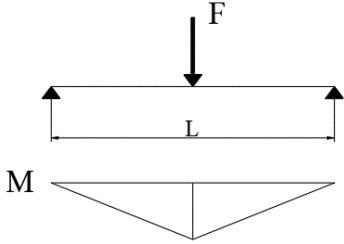


Figure 3.12. Bending moment diagram

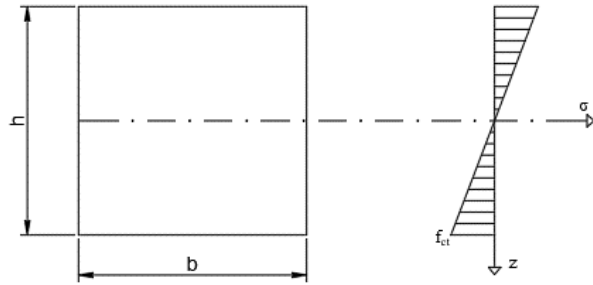


Figure 3.13. Stress distribution along cross section

The maximum moment is recorded at midspan and its value is:

$$M_{\frac{L}{2}} = \frac{FL}{4} \quad (30)$$

Afterwards, analysing the stress distribution within the cross section is possible to get the flexural strength, which is generated in the lowest part of the cross section (Figure 3.13).

The maximum tensile stress can be evaluated as follows:

$$f_{ct} = \frac{M \cdot h/2}{I} = \frac{FL}{4} \cdot \frac{h}{2} \cdot \frac{12}{bh^3} = \frac{3FL}{2bh^2} \quad (31)$$

Where  $I$  is inertia moment of the cross section.

Six specimens were tested, and the relative flexural strengths were then elaborate to obtain an average value. In the following table the name of each specimen is reported:

3 Point Bending Test Specimens	Name
	F1
	F2
	F3
	F4
	F5
	F6

Table 3.2. Specimen labels for three point bending test

The compressive behaviour of concrete is investigated by means of standard uniaxial compressive test, as reported in the European Standard (Uni En 22768-1). The test consists in the application of a growing force by means of a load controlled machine on the upper surface of a cube specimen until the failure of such element occurs.

The machinery used is composed by two parallel plates (Figure 3.14), the bottom one is fixated whereas the upper one is shifting downward in order to impress the compression on the specimen.



Figure 3.14. Uniaxial compression test setup

The specimens for this test are actually the remaining prisms from the three-point bending test previously described, whose dimension are 40 x 40 x 80 mm. The European Standards allows in fact the use of such elements for determinating concrete uniaxial behaviour.

The stress is evaluated by the ratio between applied Force over upper surface area  $\sigma = \frac{F}{A}$  whereas the strain is measured by means of a strain gauge applied on the front face of the specimen. The cubic uniaxial compression strength is the stress corresponding to failure load  $F_{max}$ , hence  $R_c = \frac{F_{max}}{A}$ .

Failure stress is actually the cubic strength of the material, which is greater than cylindrical strength due to the geometry effects. It is also possible to obtain the Young's modulus  $E$  and the Poisson's modulus  $\nu$  using the following relations:

$$E = \frac{\sigma}{\epsilon} \tag{32}$$

$$\nu = \frac{\epsilon_t}{\epsilon_l} \tag{33}$$

where  $\epsilon_t$  is the horizontal strain whereas  $\epsilon_l$  is the vertical strain, both of them are measured by means of strain gauges.

The test has been performed on 12 specimens whose label are reported in Table 3.3.

Specimens for Uniaxial Compressive Test	Name
	C1_FA1
	C2_FA1
	C3_FA2
	C4_FA2
	C5_FA3
	C6_FA3
	C7_FA4
	C8_FA4
	C9_FA5
	C10_FA5
	C11_FA6
C12_FA6	

Table 3.3. Specimen labels for uniaxial compressive test

### 3.2.2. 3D printing machine

The printer used to manufacture the specimens is a BigDelta WASP from the Italian CSP company. The printing area of this machine is a triangle, with each side being 4.0m. The printing head is sustained by three movable braces which are connected to the pillars of the machine framework. The end of each brace moves along the pillars, this controlled movement allows the exact placement of the printing head within the work area (Figure 3.15).

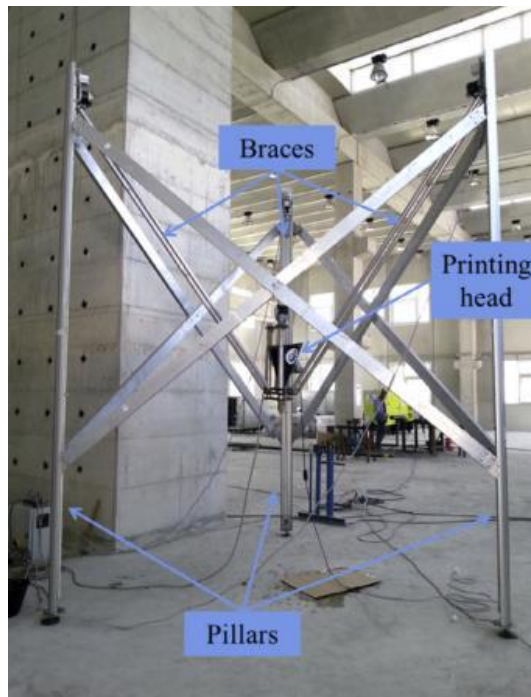


Figure 3.15. BigDelta WASP

By controlling the movement of the braces the printing head moves horizontally and vertically, reaching a maximum height of 1.5 m, Figure 3.16 depicts a phase of the printing process. The printing head is composed of a conical hopper with maximum capacity of about 20 litre of fresh concrete. The concrete is extruded by means of an endless screw towards the circular nozzle of 30 mm diameter. The printing head movement is controlled by a control unit which processes the G-Code file, the input file for the 3D-printer. The input file contains the planar print path, the relative height of subsequent concrete layers and the speed of the printing head (deposition rate).



Figure 3.16. Printing process

Every print has one parameter in common, namely the flow speed which refers to the speed of extrusion process. The flow speed is controlled by tuning the rotational speed of the endless screw in the printing head, in fact by increasing its rotational speed the material is ejected quicker.

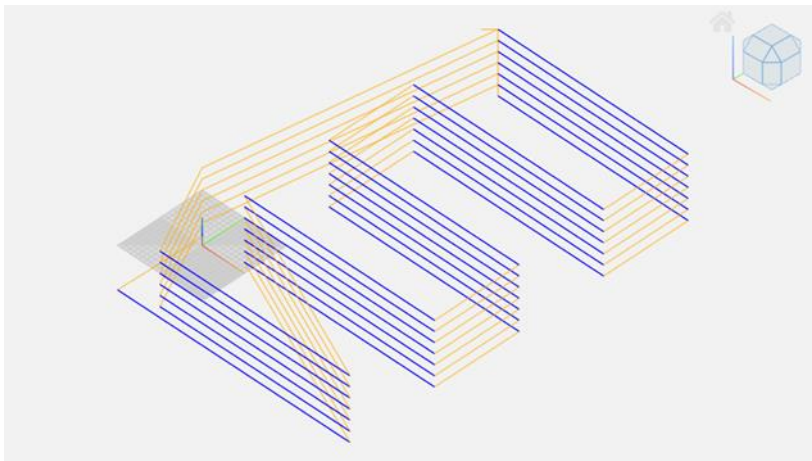


Figure 3.17. Printing Scheme

### 3.2.3. *Specimen production*

In order to carry out the experimental tests, prismatic specimens have been tested. In particular, 20 samples of 14 cm of length, 14 cm of width and 5 cm of thickness have been printed.

The printing settings aren't the same for all the specimens. Indeed, 4 groups of specimens have been made, varying different parameters, such as the building rate, the resting time and the time after the mixing process at which the printing started. The resting time, i.e. the time that elapses between the print of two subsequent layers, is one of the most important variables that influences mostly the process of cold joints' formation: higher is the time of overlapping lower is the level of connection between layers. This is the reason why different delay times, 100 s and 200 s, indicated as  $t_{r1}$  and  $t_{r2}$  respectively, have been used. In order to show better the influence of waiting time in the printing of the consecutive layers, the other two groups of specimens, characterized by higher overlapping times, specifically by waiting times of 30 min ( $t_{r3}$ ) and 60 min ( $t_{r4}$ ) have been printed.

Every printed element is made of 7 layers, of 2cm each, reaching a total height of 14 cm, and thick about 5cm. Furthermore, each print has one parameter in common: the flow speed. This parameter refers to the speed of extrusion process and it is controlled by tuning the rotational speed of the endless screw in the printing head; in fact by increasing its rotational speed the material is ejected quicker. The printing process is started immediately after the mix procedure. The printed elements have been compared with a reference bulk group, made of casting material.

The characteristics of four groups of print are summarized in the Table 3.4, while the dimensions and the print mode are schematically represented in the Figure 3.18, Figure 3.19, Figure 3.20, Figure 3.21.



Group of specimens	ID Elements	H (cm)	h (cm)	d (cm)	Waiting time (s)	Printing Speed (mm/m)
Reference	1_bk	14	2	5		
	2_bk					
	3_bk					
	4_bk					
A	A1	14	2	5	100	2000
	A2					
	A3					
	A4					
B	B1	14	2	5	200	2000
	B2					
	B3					
	B4					
C	C1	14	2	5	1800	2000
	C2					
	C3					
	C4					
D	D1	28	2	5	3600	2000
	D2					
	D3					
	D4					

Table 3.4. Main features of specimens

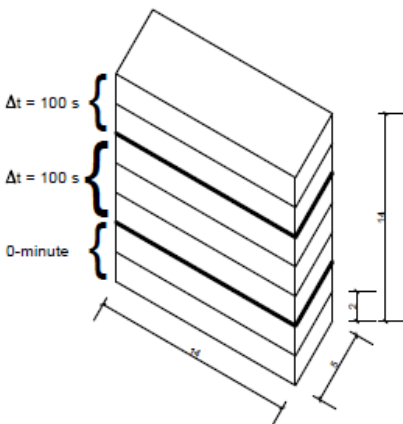


Figure 3.18. Printing Mode\_ Group A

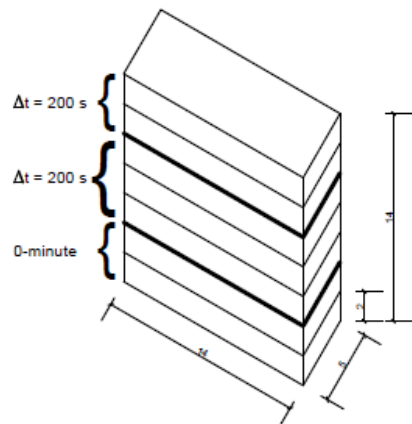


Figure 3.19. Printing Mode\_ Group B

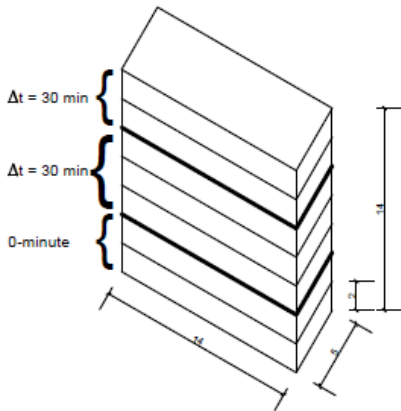


Figure 3.20. Printing Mode\_ Group C

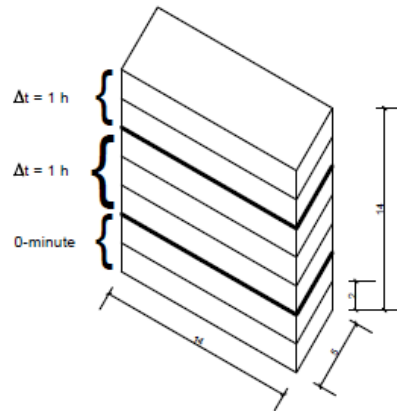


Figure 3.21. Printing Mode\_ Group D

### 3.2.4. *Interface Measurement systems*

The mechanical characterization is dependent on achieving consistent interface properties and in particular strain degree exhibited in correspondence of the interfaces making up the specimen, if subjected to increasing loads. For this reason the measurement is a phase critically important.

Firstly the acquired data comes out of the application of LVDT to the load cell, embedded in the MTS810, placing between the loading plate and the support girder (see following Figure).



Figure 3.22. LVDT application

LVDT stand for “linear variable differential transformer”, also called linear variable displacement transformer, and it is a type of electrical transformer used for measuring linear displacement. LVDT converts a position or linear displacement from a mechanical reference into a proportional electrical signal containing phase (for direction) and amplitude (for distance) information. The LVDT operation does not require an electrical contact between the moving part (probe) and coil assembly, but instead relies on electromagnetic coupling.

Concerning the strain of the specimens, another measurement instrument was used: the Digital Image Correlation technique. Digital image correlation or DIC is an optical method that employs tracking and image registration techniques for accurate 2D and 3D measurements of changes in images. Compared to strain gauge and extensometers, the amount of information gathered about the details of deformation during mechanical tests increases manifold. DIC works by comparing digital photographs of a component or test piece at different stages of deformation. By tracking blocks of pixels, the system can measure surface displacement and build up full field 2D and 3D deformation vector fields and strain maps. For DIC to work effectively, the pixel blocks need to be random and unique with a range of contrast and intensity levels. Commonly, DIC relies on finding the maximum of the correlation array between pixel intensity array subsets on two or more corresponding images, which gives the integer

translational shift between them. It is also possible to estimate shifts to a finer resolution than the resolution of the original images, which is often called "subpixel" registration because the measured shift is smaller than an integer pixel unit. For subpixel interpolation of the shift, there are other methods that do not simply maximize the correlation coefficient. An iterative approach can also be used to maximize the interpolated correlation coefficient by using nonlinear optimization techniques. Many software have been developed most of which are based on Matlab codes offering also a Graphic User Interface (GUI), among which there are N-CORR (McCormick and Lord 2010) and a Matlab-based DIC code developed by Elizabeth Jones (2015) from University of Illinois at Urbana-Champaign, which is the code used in the herein work. There are four main components to this code, each with its own GUI. To run these GUIs, simply type the name of the GUI in the Matlab command window and press enter.

- `Image_setup_GUI`: Prepares images
- `Correlate_images_GUI`: Performs the image correlation and outputs displacements
- `Compute_data_GUI`: Smooths displacements, and interpolates displacements and calculates strains using finite element shape functions
- `Visualize_data_GUI`: Displays displacements and strains in a variety of formats

The purpose of `Image_setup_GUI` is to prepare a list of the images the user wishes to correlate at once, saved as a Matlab variable name `filenamelist.mat` in the current working directory (Figure 3.23). In this part of the process all the images are converted in grey scale allowing the recognition of black and white pixel. In the `Correlate_images_GUI` (Figure 3.24) the analysis is set.

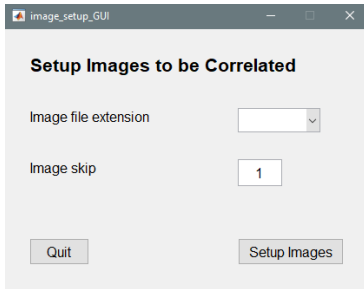


Figure 3.23. Image\_setup\_GUI

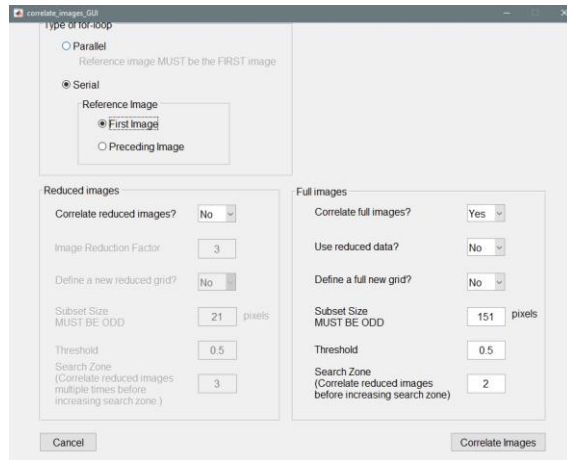


Figure 3.24. Correlate\_images\_GUI

This code has the option of running in serial (each image is correlated sequentially, one at a time) or in parallel (multiple images are correlated independently at the same time on separate processor cores). It can be chosen whether large displacements must be taken into account or not. The main parameters to define are the Subset size and the grid dimension. The subset is a rectangular zone of a defined size (number of pixels) in which the code detects a specific dots patterns which will be used as control points that are researched in the subsequent images and then the code correlates the control points of each image using specific algorithms. The size of such subset must be large enough to contain a consistent number of dots, in this way it will be possible to detect the same dots patterns from the software.

The Compute\_data\_GUI performs four main functions: it scales the displacement data from pixels to microns, smooths the displacement data, computes strains from the displacement data, and computes the deformed grids. These four functions are independent, but due to noise inherent in DIC displacements, the displacements should be smoothed before calculating strains and the deformed grid (Figure 3.25).

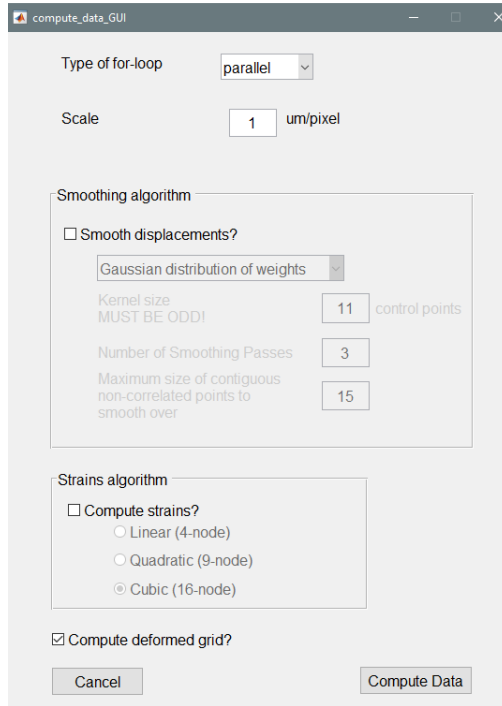


Figure 3.25. Compute\_data\_GUI

Finally the Visualize\_data\_GUI allows the user to get the results of the analysis. It is possible to extract vertical and horizontal displacement as well as vertical and horizontal strains. It is also possible to overlap the outcome on the starting photos obtaining a clear view of the strains and displacements distribution across the specimen.

In order to perform the DIC the specimens need to be prepared. Since the process is based on the recognition of pixel blocks, a high contrast between the background and a random pattern of dots is needed, therefore the specimens surface was firstly painted with a white non-acrylic paint and then a dots pattern was made on the same surface by using a simple black marker, in Figure 3.26 is reported a prepared specimen.

The images acquisition was done by means of a high resolution camera, which makes shots every 2 seconds. The images acquisition setup is shown in Figure 3.27.

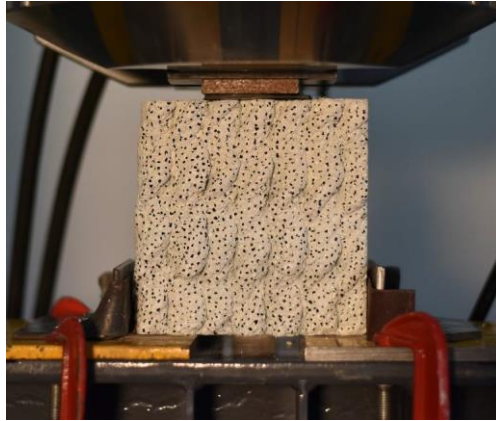


Figure 3.26. Specimen for Digital Image Correlation



Figure 3.27. Image Acquisition Setup

### 3.3 Punch-through shear test results

The main outcomes of the performed tests are Load-Displacement plots, which were evaluated by means of a load cell and a vertical LVDT. Besides, the deformations in both X (horizontal) and Y (vertical) directions were measured by digital image correlation technique.

Before describing the overall behaviour of the tested specimen, the results in term of load vs displacement are shown in order to give a visual supports which allows a better understanding of samples' response subjected to the tests.

All load vs displacement plots are affected by measurement errors at the begin due to little settlements between the load plate and the specimens therefore the initial part of every curve was corrected by considering that the real curves have not consistency until a load of 0.5 kN. This means that the part of the curves below the limit of 0.5 kN was considered as mere experimental error, thereby the displacement corresponding to 0.5 kN on the curve was erased and the entire curve was shifted toward a new value of zero.

Regarding the bulk concrete elements, in order to give a clear picture of the specimens' behavior, the plots are shown in Figure 3.28.

Looking at the curves, all the specimens show a comparable behaviour, namely there is an initial linear branch until reaching a slight discontinuity which refers to the crack onset (see point O in Figure 3.28), afterwards, the loading starts again to grow up to the load that refers to the complete failure of the element (see point F in Figure 3.28). It is worth noticing that the rate at which the load increases is almost identical; this means that the overall stiffness does not change, whether there are cracks or not.

As for the mode of fracture, all the specimens have exhibited a shear failure. The first cracks indeed arose at the inner edge of the supports, subsequently the propagation of the fractures happens along the surfaces located between the supports and the loading platen. A confirmation of this type of failure is provided by the strain distribution achieved via the Digital Image Correlation. For instance, the distribution of the transversal strains at the cracks' onset and at complete failure with regards to the bulk specimen ID 2\_bk as an example are shown in Figure 3.29.



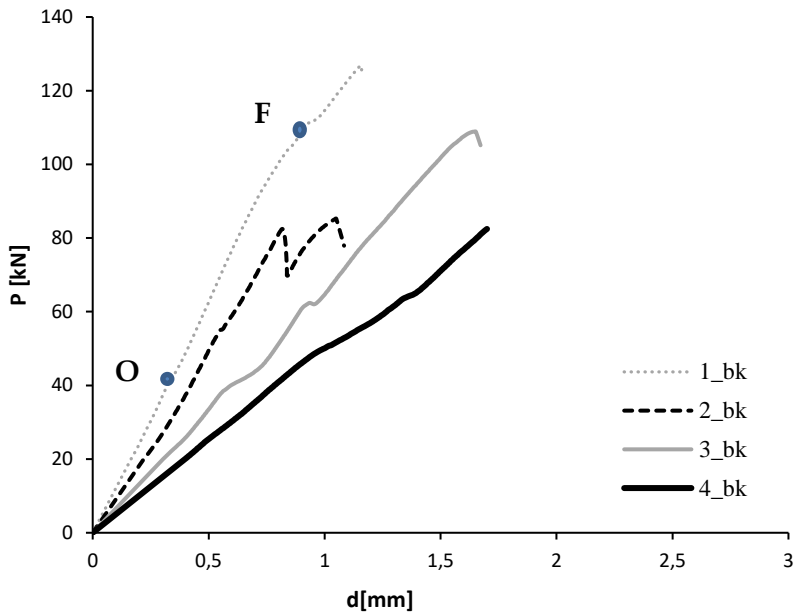


Figure 3.28. P-d Plots of Bulk Concrete Specimens

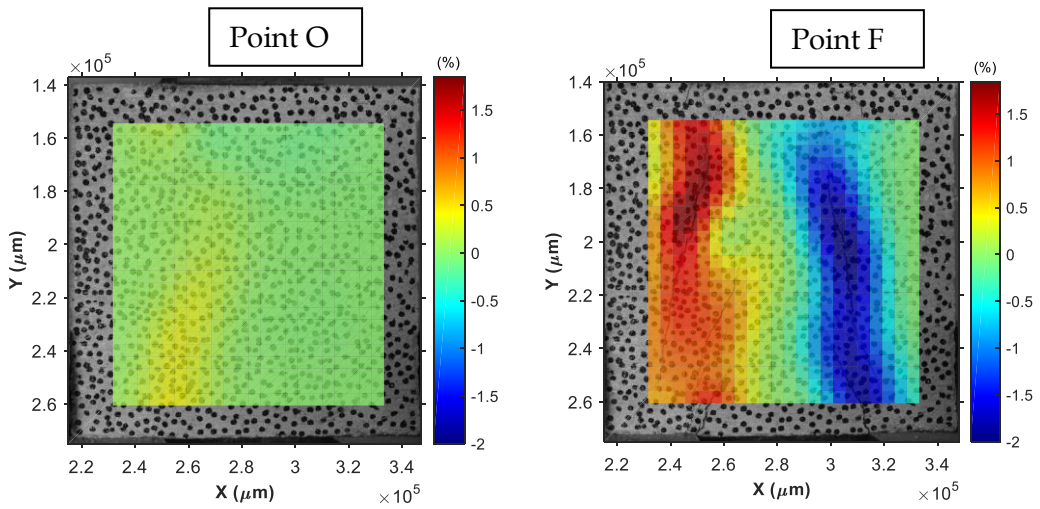


Figure 3.29. left:  $\gamma_{xy}$  distribution at the cracks onset, (bulk specimen 2\_bk, point O); right:  $\gamma_{xy}$  distribution at the failure, (bulk specimen 2\_bk, point F)

The findings of the tests carried out on printed elements are reported in the following plots, where the different curves for each specimen of the same group

and the relative average curve are presented.

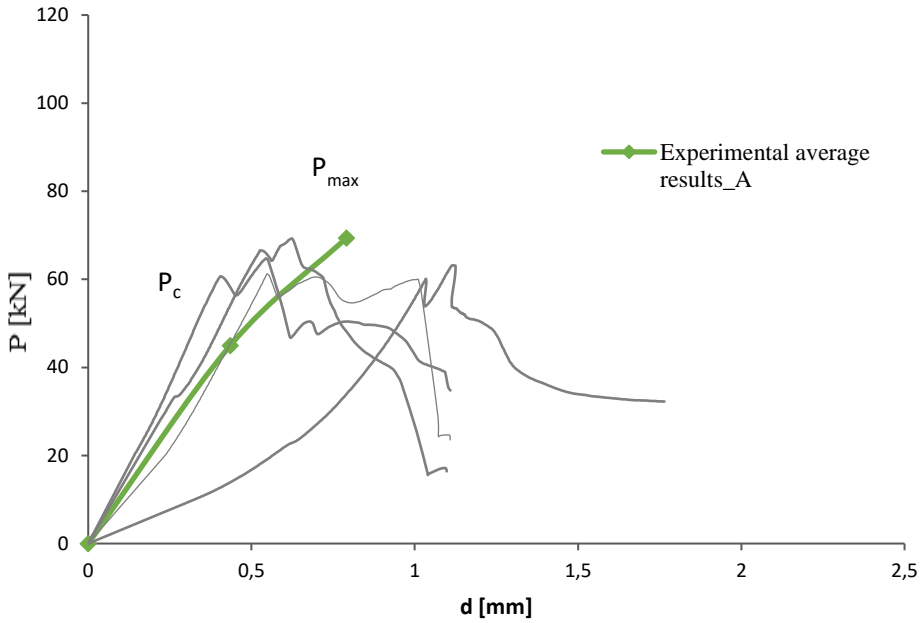


Figure 3.30 Load-displacement curve, specimens group A ( $t_{r1}=100s$ )

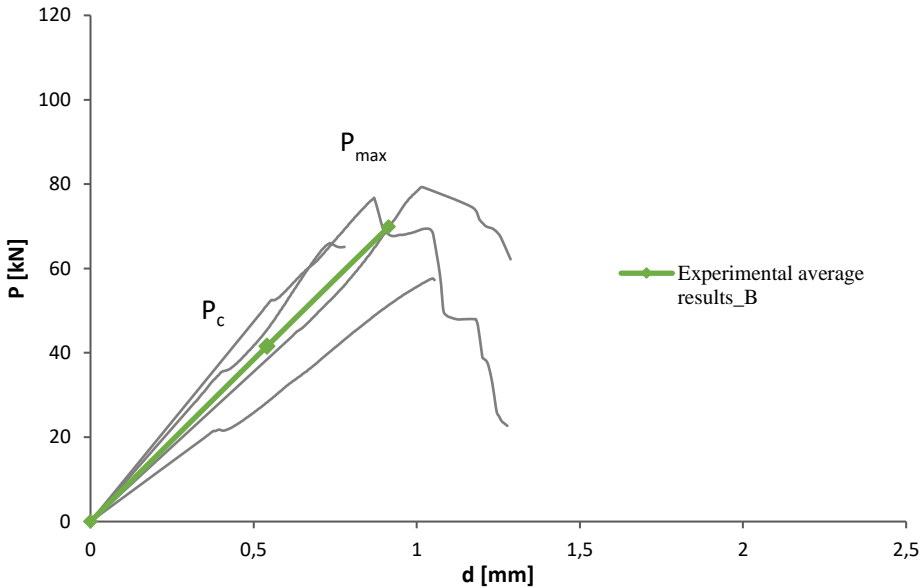


Figure 3.31 Load-displacement curve, specimens group B ( $t_{r2}=200s$ )

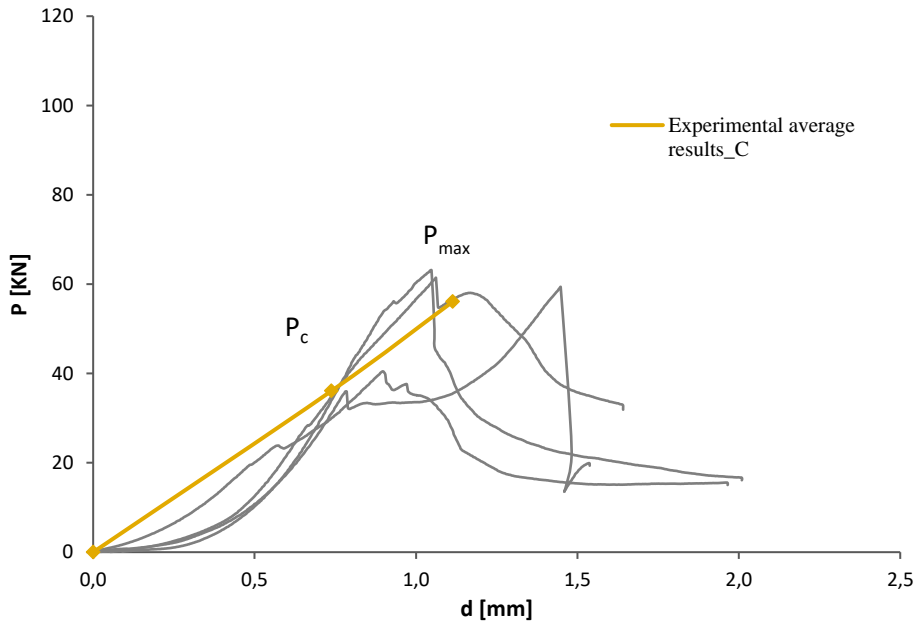


Figure 3.32 Load-displacement curve, specimens group C ( $t_{r3}=1800s$ )

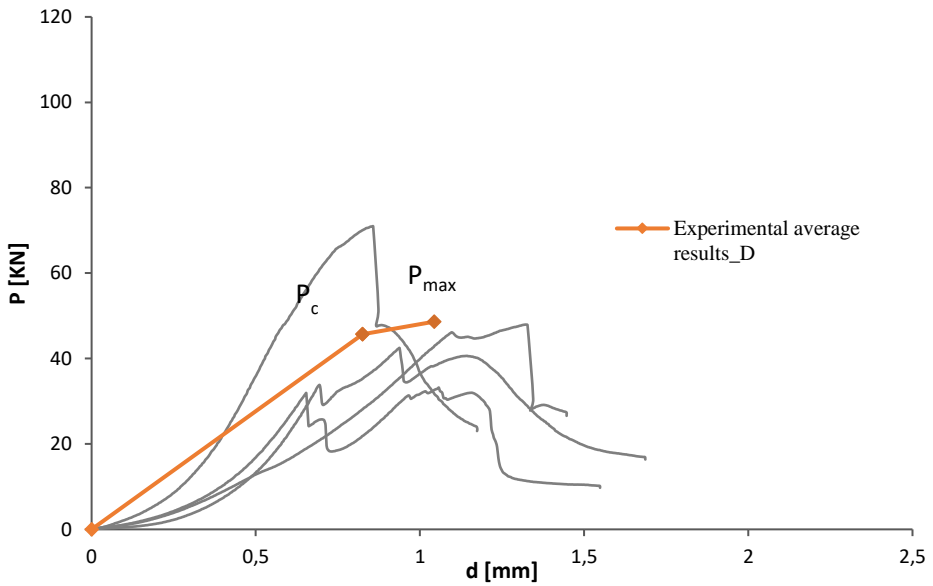


Figure 3.33 Load-displacement curve, specimens group D ( $t_{r4}=3600 s$ )

From the analysis of the results, the trend of the curves is about the same for every sample, characterized by two main stages, as in the case of bulk elements, but now the first linear part ends with the occurrence of a clear discontinuity that corresponds to the onset of the first crack in the interface surfaces and the relative load is called critical load,  $P_c$ . Subsequently, in the final part the load increases until its maximum value,  $P_{max}$ , which represents the complete propagation of the shear failure.

In tabular form, the values of maximum and critical loads and the corresponding displacements are reported. The critical energy release rate  $G_{IIc}$  is also computed. The way by which  $G_{IIc}$  was evaluated from the experimental results is described in the previous chapter. Briefly, the ratio between the area under the load-displacement curve prior to the load that corresponds to the cracks onset and the area of the failure surface provides the value of  $G_{IIc}$  (see Table 3.5).

The difference between the  $P_{max}$  and  $P_c$  is evaluated in order to assess the growth of the load starting from the cracks initiation and the complete propagation of such fractures.

The graph in Figure 3.34 shows a certain dissimilarity in terms of  $P_{max}$  values between the first two investigated groups of specimens (Series A and Series B), characterized by similar overlapping times and between the last ones (Series C and Series D). The same analysis involves  $P_c$  values of two groups, confirming that differences in the waiting time imply appreciable differences in terms of reached load, weakening the printed element.

Series	Label	$P_{max}$ (kN)	$d(P_{max})$ (mm)	$P_c$ (kN)	$d(P_c)$ (mm)	$G_{IIC}$ (N/mm)
A	A1	64,74	0,55	60,39	0,90	1,08
	A2	69,28	0,62	32,60	0,26	0,63
	A3	70,77	1,58	26,67	0,62	1,33
	A4	72,70	0,55	60,27	0,68	2,00
<b>mean values</b>		<b>69,37±3,39</b>	<b>0,83±0,50</b>	<b>44,98±0,61</b>	<b>0,61±0,26</b>	<b>1,26±0,57</b>
B	B1	76,70	0,87	52,39	0,55	2,22
	B2	79,29	1,02	45,15	0,63	2,13
	B3	65,97	0,73	35,74	0,41	1,71
	B4	57,58	1,05	32,99	0,62	1,62
<b>mean values</b>		<b>69,89±10</b>	<b>0,92±0,15</b>	<b>41,57±0,55</b>	<b>0,55±0,10</b>	<b>1,92±0,30</b>
C	C1	40,49	0,90	23,85	0,58	0,83
	C2	61,41	1,06	28,44	0,67	0,68
	C3	63,11	1,05	56,18	0,93	2,06
	C4	59,37	1,45	35,95	0,78	2,52
<b>mean values</b>		<b>56,09±10,5</b>	<b>1,11±0,23</b>	<b>36,10±14,3</b>	<b>0,74±0,15</b>	<b>1,52±0,91</b>
D	D1	33,21	31,91	1,06	0,65	0,86
	D2	70,95	70,95	0,86	0,86	3,42
	D3	42,44	33,78	0,94	0,69	1,20
	D4	47,94	46,15	1,32	1,10	3,25
<b>mean values</b>		<b>48,64±16</b>	<b>45,70±0,20</b>	<b>1,04±17,9</b>	<b>0,83±0,20</b>	<b>2,18±1,34</b>

Table 3.5. Experimental results for printed specimens

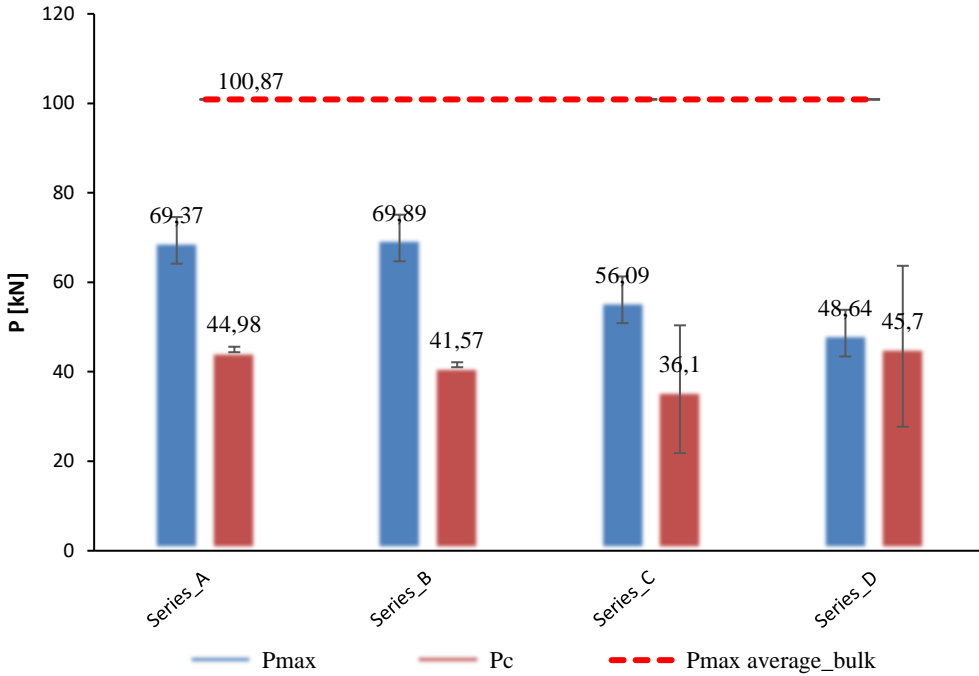
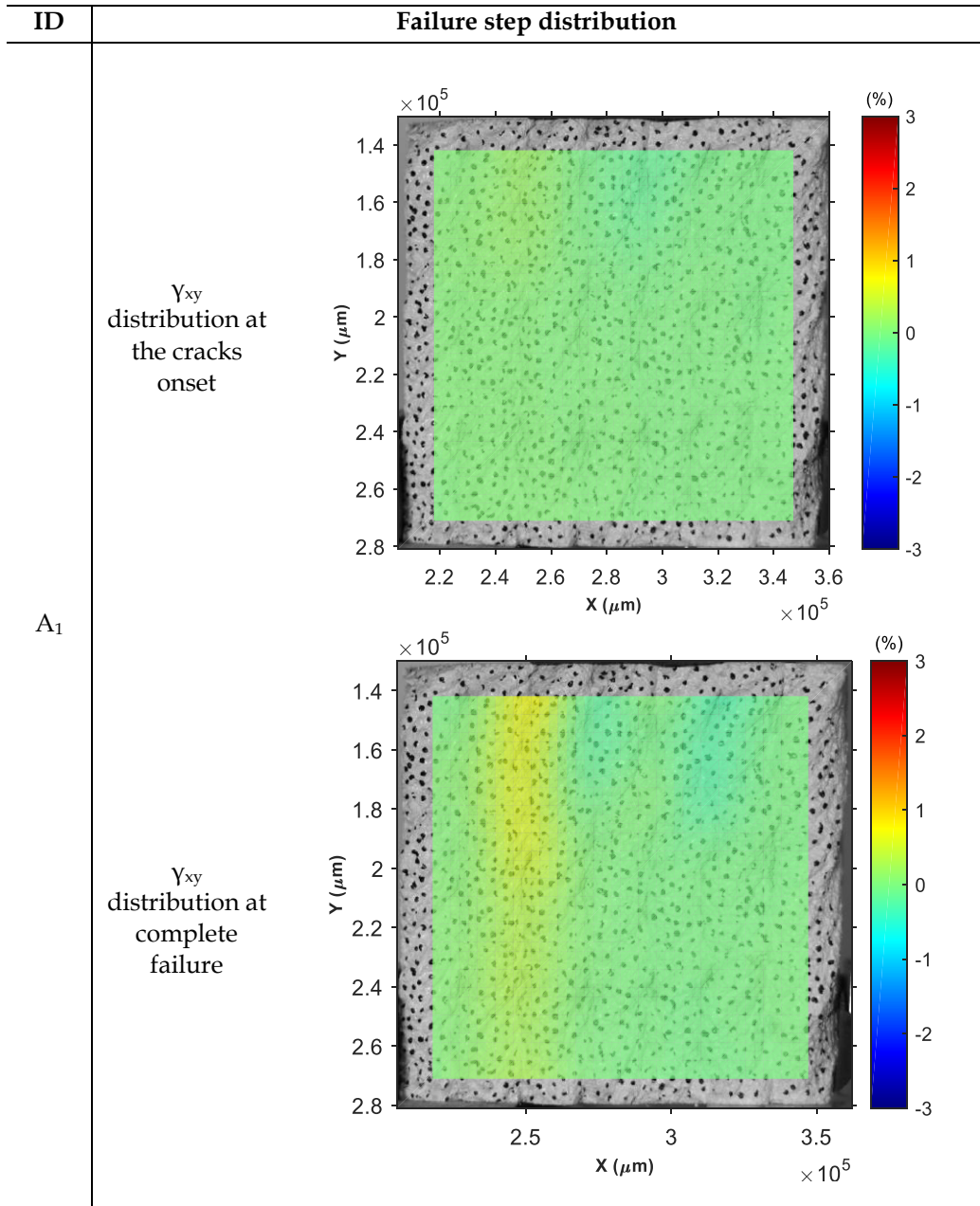


Figure 3.34 Comparison between average values of  $P_{max}$  and  $P_c$

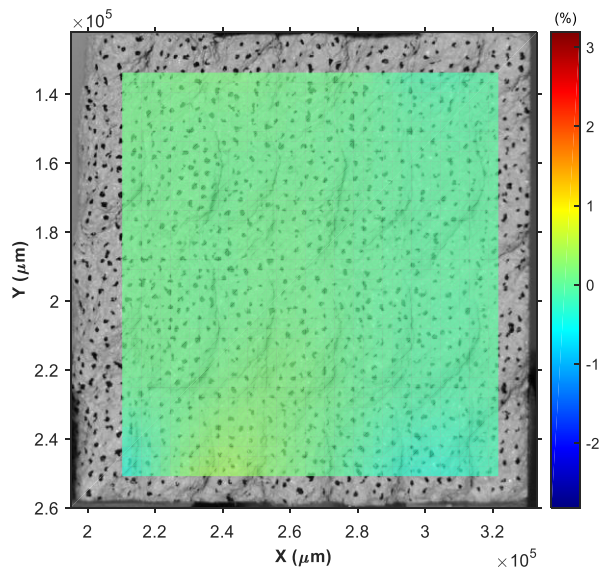
The presence of shear failure mechanisms highlighted by the trend of the curves is also confirmed by DIC technique, which exhibits in the case of printed elements an homogeneous strain distribution and consistent with the purpose of the test, i.e. enforce a pure shear failure across the prefixed surfaces of fracture. In the following table, the transversal strain distribution at the cracks onset and at the failure for a random specimen belonging to each type of the group are represented.

It is worthy to note that the difference between the maximum and critical load values tends to decrease as time gap increases. The reason is why the brittle behavior, exhibited by the reaching of failure as soon as the first crack occurs, is more remarkable in the case of elements with weaker interfaces.

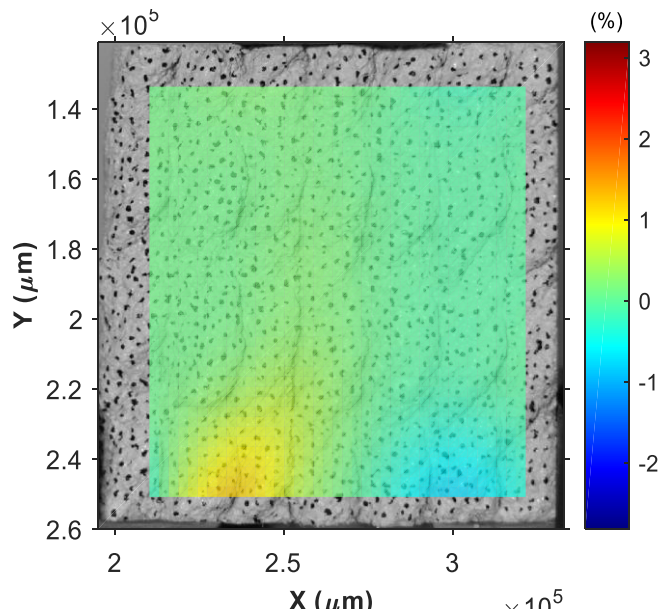


B<sub>1</sub>

$\gamma_{xy}$   
distribution at  
the cracks  
onset



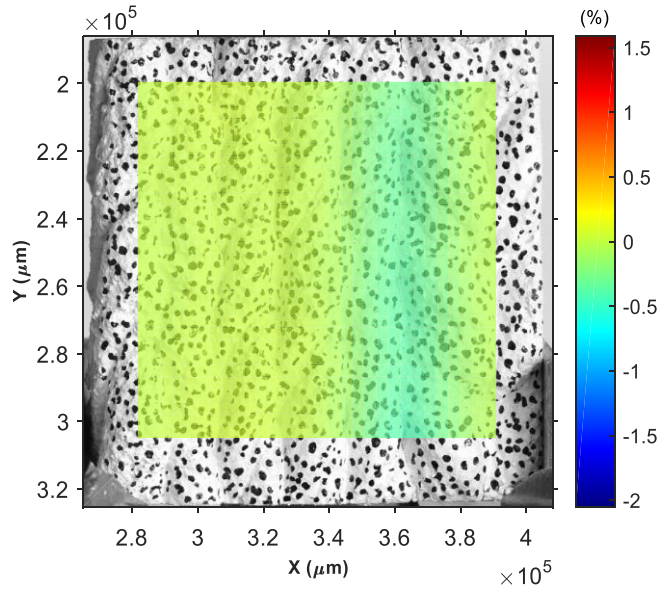
$\gamma_{xy}$   
distribution at  
complete  
failure



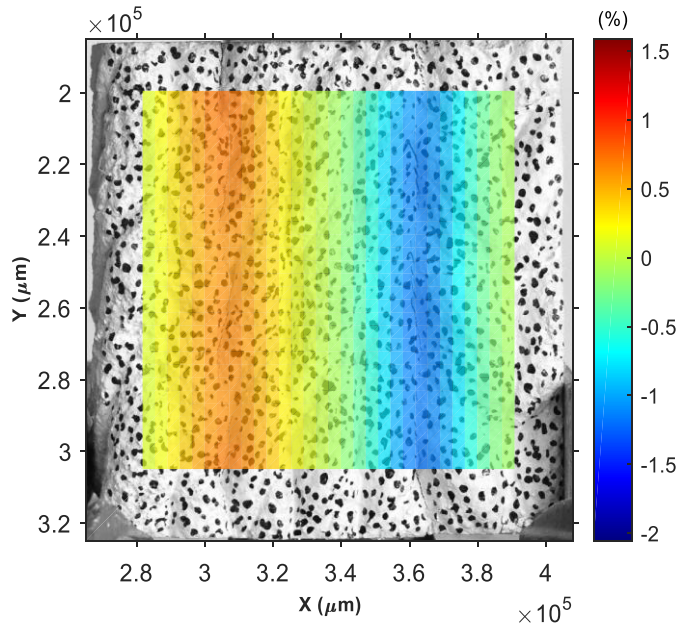


C<sub>1</sub>

$\gamma_{xy}$   
distribution at  
the cracks  
onset



$\gamma_{xy}$   
distribution at  
complete  
failure



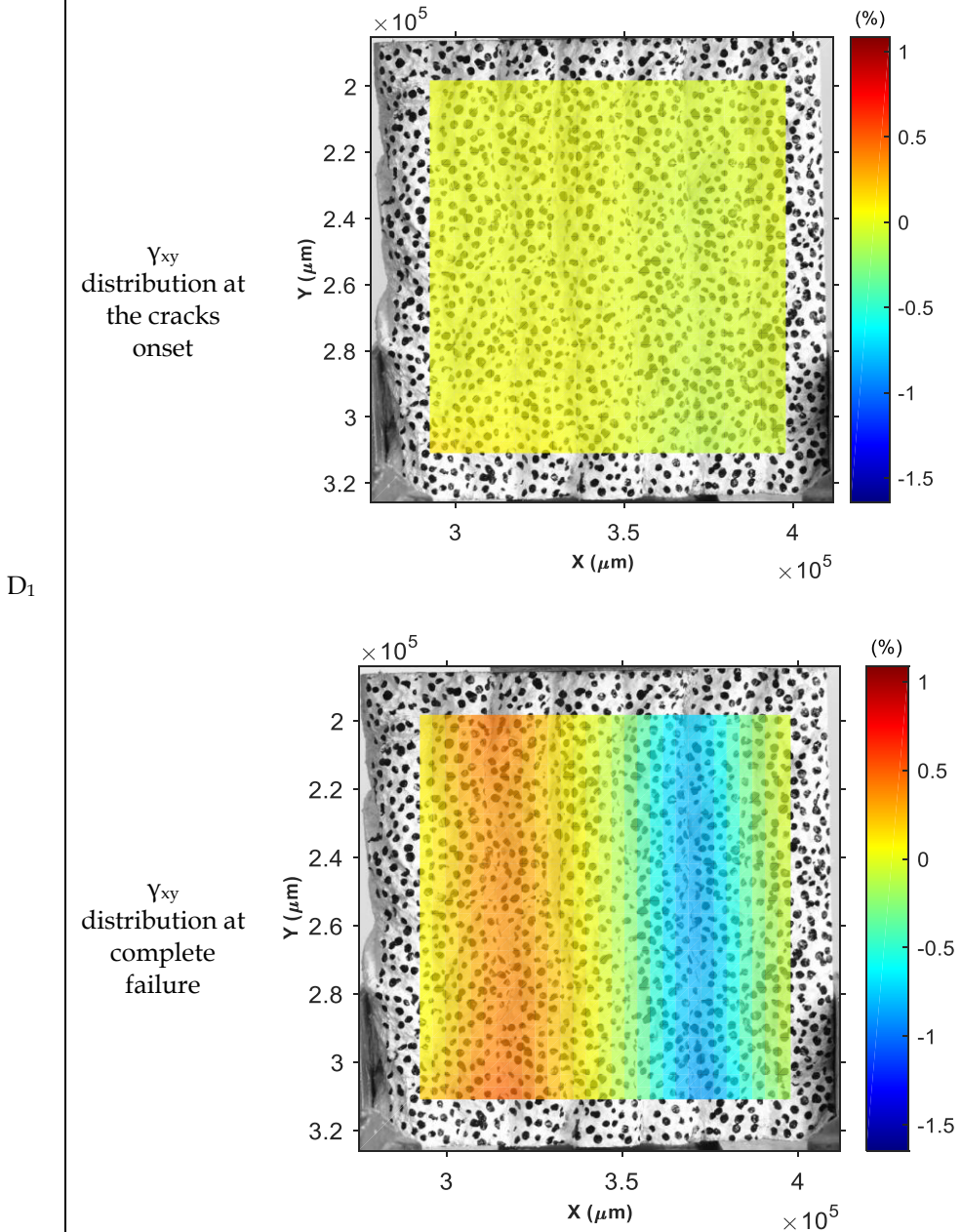



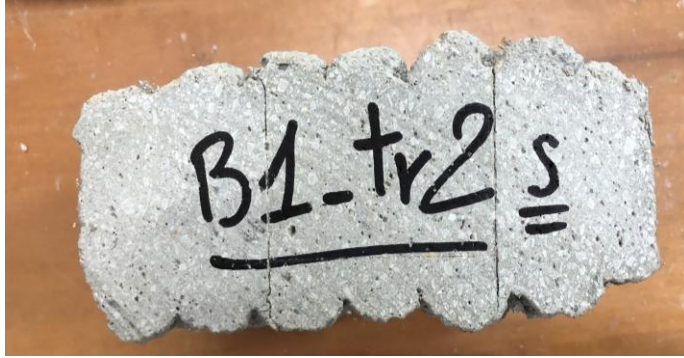
Table 3.6. The transversal strain distribution at the cracks onset and at the failure for a specimen (as an example) belonging to each group

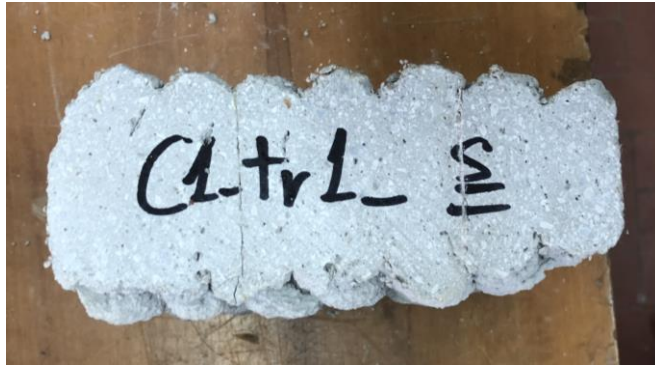
Thanks to the DIC it is possible to assert that the punch-through shear test enforces a pure shear failure, like in the original setup from the 1987 by

Davies (Davies, Yim, and Morgan 1987). In fact, the cracks start from the bottom surface and develop along two sliding surfaces, as demonstrate also the following pictures, exhibiting an representative specimen of each group after the complete failure.

ID	Failure picture
A <sub>1</sub>	

B<sub>1</sub>





C<sub>1</sub>



D<sub>1</sub>



Table 3.7. The images representing the failure for a specimen (as an example) belonging to each group

## References

- Asprone, D., Auricchio F., Menna C., and Mercuri V.. 2018. “3D Printing of Reinforced Concrete Elements: Technology and Design Approach.” *Construction and Building Materials* 165 (March): 218–31. <https://doi.org/10.1016/j.conbuildmat.2018.01.018>.
- “BS EN 12350-2:2009 Testing Fresh Concrete. Slump-Test (Withdrawn), British Standards Institution - Publication Index | NBS.” n.d. Accessed October 23, 2019. <https://www.thenbs.com/PublicationIndex/Documents/Details?DocId=288976>.
- Davies, J., Yim C. W.A., and Morgan T. G.. 1987. “Determination of Fracture Parameters of a Punch-through Shear Specimen.” *International Journal of Cement Composites and Lightweight Concrete* 9 (1): 33–41. [https://doi.org/10.1016/0262-5075\(87\)90035-2](https://doi.org/10.1016/0262-5075(87)90035-2).
- Kim, H., Park E., Kim S., Park B., Kim N., and Lee S.. 2017. “Experimental Study on Mechanical Properties of Single- and Dual-Material 3D Printed Products.” *Procedia Manufacturing* 10: 887–97. <https://doi.org/10.1016/j.promfg.2017.07.076>.
- Le, T. T., Austin S. A., Lim S., Buswell R. A., Gibb A. G.F., and Thorpe T.. 2012. “Mix Design and Fresh Properties for High-Performance Printing Concrete.” *Materials and Structures/Materiaux et Constructions* 45 (8): 1221–32. <https://doi.org/10.1617/s11527-012-9828-z>.
- Le, T. T., Austin S. A., Lim S., Buswell R. A., Law R., Gibb A. G.F., and Thorpe T.. 2012. “Hardened Properties of High-Performance Printing Concrete.” *Cement and Concrete Research* 42 (3): 558–66. <https://doi.org/10.1016/j.cemconres.2011.12.003>.
- Mccormick, N., and Lord J.. 2010. “Digital Image Correlation.” *NUMBER*. Vol. 13.
- Nerella, V. N., Krause M., Näther M., Mechtcherine V., Nerella V N, Krause M, and Näther M. 2016. “Studying Printability of Fresh Concrete for Formwork Free Concrete On-Site 3D Printing Technology (CONPrint3D) CONPrint3D® View Project Textile Reinforced Concrete View Project Studying Printability of Fresh Concrete for Formwork Free Concrete on-Site 3D Printing Technology (CONPrint3D).” <https://www.researchgate.net/publication/296817129>.
- Nerella, V.N., and Mechtcherine V.. 2017a. “MICRO-AND MACROSCOPIC INVESTIGATIONS ON THE INTERFACE BETWEEN LAYERS OF 3D-PRINTED CEMENTITIOUS ELEMENTS.” <https://www.researchgate.net/publication/319504633>.
- Panda, B. N., Bahubalendruni R. M.V.A., Biswal B. B., and Leite M.. 2017. “A CAD-Based Approach for Measuring Volumetric Error in Layered Manufacturing.” *Proceedings of the Institution of Mechanical Engineers, Part C: Journal of Mechanical Engineering Science* 231 (13): 2398–2406. <https://doi.org/10.1177/0954406216634746>.
- Rahul, A.V., Santhanam M., Meena H., and Ghani Z.. 2019. “Mechanical Characterization of 3D Printable Concrete.” *Construction and Building Materials* 227 (December): 116710.

<https://doi.org/10.1016/j.conbuildmat.2019.116710>.

Wolfs, R. J.M., Bos F. P., and Salet T. A.M.. 2018. “Early Age Mechanical Behaviour of 3D Printed Concrete: Numerical Modelling and Experimental Testing.” *Cement and Concrete Research* 106 (April): 103–16. <https://doi.org/10.1016/j.cemconres.2018.02.001>.

Zareiyan, B., and Khoshnevis B.. 2017. “Effects of Interlocking on Interlayer Adhesion and Strength of Structures in 3D Printing of Concrete.” *Automation in Construction* 83 (August): 212–21. <https://doi.org/10.1016/j.autcon.2017.08.019>



## Chapter 4

# **NUMERICAL SIMULATION OF THE INTERFACE BEHAVIOUR OF 3D PRINTED CONCRETE ELEMENTS**

This chapter deals with the numerical finite elements modelling of the printed multilayers structure behavior. Specifically the adopted three-component model is described and analyzed, focusing on details and formulations, in order to provide the background for the understanding of the analysis results.

Following the choice of constitutive law on the basis of the numerical model and the calibration of the input material parameters, different simulations have been performed, varying the structure of the elements (printed or not printed) with the aim to reproduce the experimental shear response of the test specimens (reference series and A, B, C, D groups), described in the previous section.

## 4.1 Numerical analysis

The implementation of an interface behavior model in a finite element method (FEM) aims to simulate printed elements subjected to increasing loads. A model which takes into account the overall anisotropic behaviour and the occurrence of cold joints is needed.

The performed approach is based on the treatment of the “bulk concrete”, i.e. the core of the concrete which constitutes every layer, and the interface links separately.

The research of a consistent modelling of the joints is a challenge which requires an initial assumption, i.e. the joints establish a weak surface whose strength is lower than the bulk concrete one. Therefore, cracks are going to onset and propagate along the interfaces. Starting from this hypothesis, the models refer to Fracture Mechanics which is the field of study that concern the cracks onset and their propagation.

Usually, three crack patterns are identified, namely Mode I, Mode II and Mode III, which are depicted in Figure 4.1.

Mode I, also known as “opening mode”, features plane stresses and symmetric stresses which produce the crack opening, i.e. normal displacements of the faces of the crack. Mode II, called “in-plane shear/sliding mode”, refers to a plane stress stresses state and antisymmetric stresses which cause a relative displacement of the crack faces.

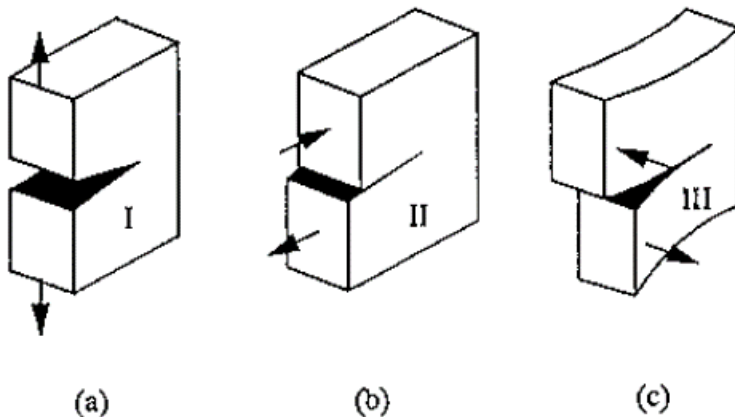


Figure 4.1. a) Mode I “opening mode”, b) Mode II “sliding mode”, c) Mode III “tearing mode”

By analyzing the Fracture Mechanic methods referred to the failure of brittle-like materials as concrete, the model by Griffith (Griffith 1995) introduced Linear Elastic Fracture Mechanics (LEFM), suggesting that the gap between computed strength and real strength of brittle materials was related to the stress concentration that arise at the tips of of presents flaws and providing reliable result if the material around the crack keeps an elastic behaviour. According to this work, three possible situations can occur:

$G < G_c$	$da = 0$	No fracture propagation (stable)
$G = G_c$	$da \geq 0$	Quasi-static fracture propagation
$G > G_c$	$da > 0$	Dynamic fracture propagation (instable)

where  $G$  is the strain energy release rate or driving force of the crack,  $G_c$  is the fracture resistance and  $da$  is the crack length increase.

Irwin (Irwin 1968), indeed pointed out how a crack within an element modifies the linear elastic behaviour in the close proximity of crack tips, stating that the fracture propagation in brittle material occurs when the stress intensity factor  $K_I$  reaches a critical value  $K_{Ic}$ ,  $K_{IIc}$  or  $K_{IIIc}$ , called fracture toughness, for Mode I, Mode II and Mode III respectively.

Furthermore, he found a relationship between the energy strain release rate  $G$ , which is equal to the variation of total potential energy of the system against a unitary increment of the crack length, and the stress intensity factor  $K_{I,II,III}$  which defines the stress state at the apex of the crack:

$$G_i = \frac{K_i^2}{E'} \quad i = I, II, III \text{ for the Mode } I, II, III \quad (34)$$

Indeed, the approach developed by non-linear fracture mechanics suggests the increase in plastic deformations near the crack apex, estimating the length of the plastic zone. In the following table are reported some values of such characteristic length measured by means of experimental tests carried out by some authors (Karihaloo and Nallathambi 1991).

Material	l (mm)	Author
Mortar	100 - 200	(Hillerborg A. 1983)
High Strength Concrete (<100 MPa)	150 - 300	(Hilsdorf and Brameshuber 1991)
Concrete	200 - 500	(Hillerborg A. 1983)

Table 4.1. Estimated values of characteristic length

The value of characteristic length defines whether a linear elastic model can be used or not. Indeed, according to Bažant et al. (Bažant et al 2001) depending on structure size  $D$ , understood as the dimension of the cross-section, different theories are appropriate for analysing failure. They may be delineated as follows:

$$D/l \geq 100 \quad \text{Linear Elastic Fracture Mechanics} \quad (35)$$

$$5 \leq D/l < 100 \quad \text{Non-linear quasi-brittle fracture mechanics} \quad (36)$$

$$D/l < 5 \quad \text{Non-local damage plasticity} \quad (37)$$

In this context, the Cohesive Model was the most suitable for purposes of this research.

#### 4.1.1. Cohesive Model

The cohesive zone model is a model in which fracture formation is regarded as a gradual phenomenon and the separation of the surfaces involved in the crack takes place across an extended crack tip, or cohesive zone, and is resisted by cohesive tractions. In cementitious materials in the near tip zone of cracks called fracture process zone microcracks and damages take place and microscopic dissipative and non-linear phenomena occur. In Figure 4.2 is depicted the process zone which is seen as fictitious extension of the crack.

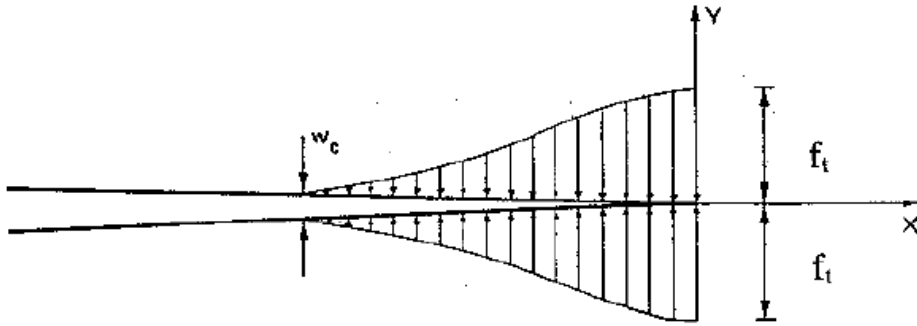


Figure 4.2. Cohesive forces in the fracture process zone

The point that separates the process zone from the real fracture is called crack tip whereas the point that separates the process zone from the intact material is called fictitious crack tip.

The basic hypothesis of the cohesive model are the following (Hillerborg, Mod er, and Petersson 1976):

- the process zone starts developing when the tensile principal stress achieves the tensile resistance of the material  $f_t$  and it propagates in the direction normal to  $f_t$ ;
- the material in the process zone is partially damaged but it can still transfer stresses;
- out of the process zone the material behaves as linear-elastic material;
- the model is accepted if outside the process zone the tensile principal stress doesn't reach the tensile resistance of the material.

The cohesive forces acting in the process zone are decreasing function of the distance  $w$  between two faces of the fracture. There are some assumptions in the study of cohesive model:

- non shear stresses are considered,
- a softening law between cohesive stresses  $\sigma$  and  $w$ , which could be linear, bilinear or exponential, is considered;
- the existence of a value  $w_c$  called critical fracture opening, after which no stresses can be transferred, is assumed;
- the area under the  $\sigma$ - $w$  is equals to the fracture energy  $G_f$ .

The surface-based cohesive interaction is founded on traction-separation law (see Figure 4.3), where the traction represents the stress which arises between two

points of adjacent surfaces and the separation stands for the relative displacement between two points of head-to-head surfaces.

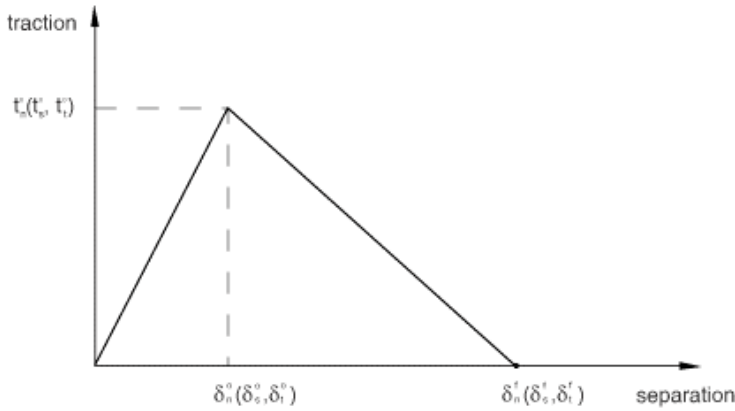


Figure 4.3. Traction-separation law, cohesive model

In the traction-separation law plot, the principal parameters can be identified, namely the initial stiffness  $K$ , the damage-initiation stress and the fracture energy which is given by the area under the curve. These parameters have to be determined for each mode of fracture, i.e. Mode I, Mode II and Mode III. Therefore, it shall be  $K_n$ ,  $K_s$  and  $K_t$  for initial stiffness of Mode I, II and III respectively;  $t_n$ ,  $t_s$  and  $t_t$  for what concerns damage-initiation stress and  $G_{Ic}$ ,  $G_{IIc}$  and  $G_{IIIc}$  for critical energy strain release rate. The determination of the critical fracture energy must be based on the load when the first crack appears. This load  $P$  is termed the 'pop-in' load, as shown in Figure 4.4. Extensive micro-cracking occurs beyond this load and the corresponding energy is not associated with the material fracture toughness. The crack growth beyond this point represents latent strength in the material. The knowledge of these parameters and the choosing of softening law of the curve allow the defining of cohesive surface-based model properly.

Among the defining parameters of cohesive model, the attention has been focused on  $G_{IIIc}$ , which represents the energy required for cracks propagation for sliding mode only (Figure 4.5). The choice of starting from shear behaviour lies on the fact that shear failure must be avoided.

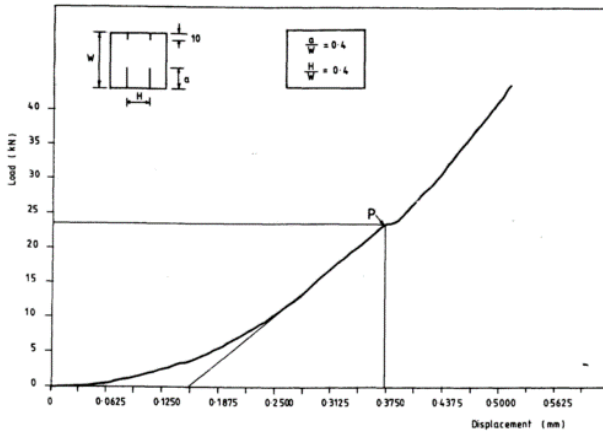


Figure 4.4 Typical load-displacement curve from the punch-through test

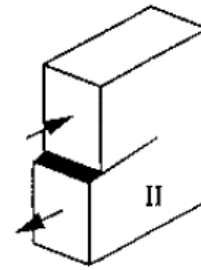


Figure 4.5. Mode II, sliding mode

Specifically, in every structures shear failures have always been critical aspects due to the type of failure which they lead to. Indeed, a shear failure is essentially brittle which means that the overall structure's integrity will be completely overcome once this type of failure will occur. In order to avoid brittle failures a thorough understanding of shear mechanism are needed. The last statement is valid for every type of structures and structural elements, ranging from steel structures to 3D-printed concrete elements. Moreover, concrete elements are generally subjected to compressive loads since their low tensile strength. Indeed, concrete elements usually design to avoid excessive tensile stress and undergo mainly compressive stresses instead. Concerning the shear strength of concrete elements, they have not such a high shear strength, however it is basically impossible to avoid shear stresses arising. The latter observation leads to focus on a shear/sliding mode of fracture.

In particular, the area under the load-displacement curve showed in Figure 4.4, in correspondence with the load of cracks onset, called  $P_c$ , divided by area of the failure surface, given by the depth of the specimen multiplied for its height, results the wanted value of  $G_{IIc}$ .

In practice, interfaces joints can be seen like distinct elements of the system, which behaves in a completely different way compared to plain concrete. The word "joints" refers to the links between two elements, in this case two layers of concrete, to consider separately. Firstly, known the link thickness, a FEM method

could be implemented just setting a sheet of material with specific properties between two concrete layers. The use of specific sheets of material fulfills the description of element-based interaction in the Finite Element Methods analysis. In order to use the latter method, it would be needed an analysis on the link sheet thickness which is related to hardening features and time gaps. A way to get around the problem is to use nodes-based interaction instead of element-based interaction. Node-based interaction stands for contact interaction, namely the behaviour of two surfaces entering in contact. In this type of interaction a constitutive equation must be defined between nodes of two surfaces in contact.

Once chosen the node-like contact interaction, the properties of such connection must be understood in order to pick the right interaction method within the FEM software (i.e. Abaqus/Standard).

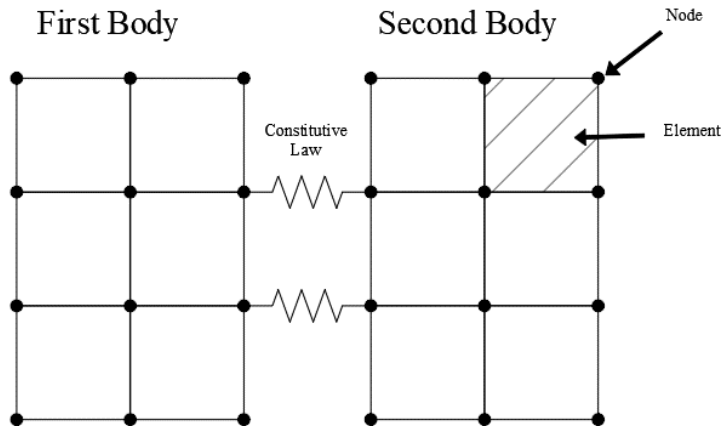


Figure 4.6. Schematic of node-based interaction

Commercial software such as Abaqus allows to model different types of node-based interaction contact, and they differentiate each other mainly depending on how the nodes of any surface are related to the nodes of the other surface, in other words depending on which type of interactions are used node-to-surface or surface-to-surface. The latter has been proved to fit well in modelling surfaces which slide over one. Surface-to-surface discretization considers the shape of both the slave and master surfaces in the region of contact constraints, where some penetration could be observed at individual nodes.



#### 4.1.2. Cohesive Model calibration

The cohesive model calibration consists in the check of input material data.

The nonlinear behaviour of the cementitious materials is modelled using the concrete damage plasticity (CDP) model (Lee, Fenves, and Member, 1998). It assumes as main failure mechanisms the tensile cracking and the crushing of the concrete and allows to characterise the post-elastic concrete's behaviour defining hardening and softening branches of the stress-strain curve of concrete. In order to define the biaxial and triaxial behaviour of the material, the work of T. Jankowiak and T. Lodygowski (Jankowiak and Lodygowski, 2005) was considered as a reference. In the Table 4.2 parameters utilized are shown.

Dilatation Angle	Eccentricity	$\sigma_{b0}/\sigma_c$	$K_c$
38°	1	1.12	2/3

Table 4.2. CDP model parameters

A model debugging has been performed, using a single element of mesh, with specific boundary conditions and subjected to the loading conditions in displacement control. As can be seen from the following figures, the input data and the output data correspond perfectly, so the material parameters can be confidently used.

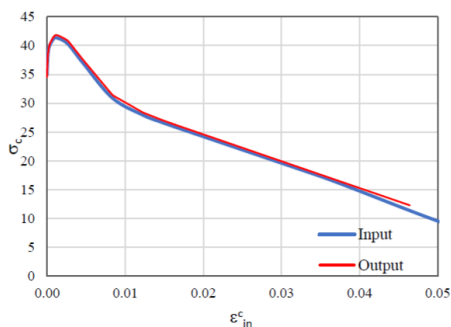


Figure 4.7 Comparison Compressive Curve, input vs output

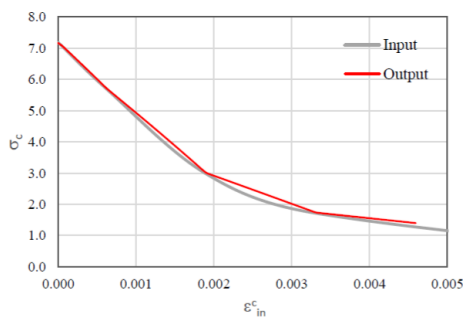


Figure 4.8 Comparison Tensile Curve, input vs output

Whereas, as for the uniaxial mechanical properties of the material, uniaxial compression test and three-point bending test have been performed to obtain the

Young Modulus ( $E$ ) and so the shear modulus ( $G=E/2(1-\nu^2)$ ), the maximum compressive strength ( $f_{c,max}$ ), the compressive strength at the end of the linear branch of the  $\sigma$ - $\epsilon$  curve ( $f_{c,linear}$ ) and maximum tensile strength ( $f_{ct}$ ).

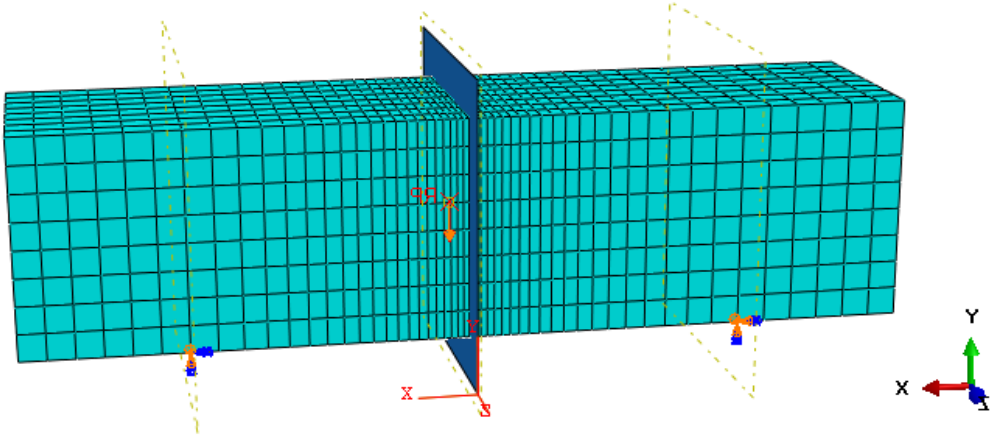


Figure 4.9 Three Point Bending test Simulation

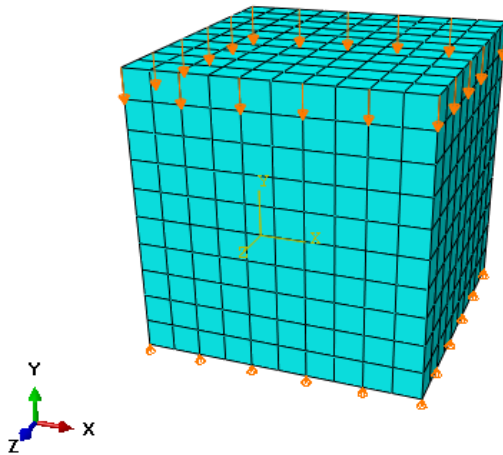


Figure 4.10 Uniaxial compressive test Simulation

It has been picked the average values of the test outcomes (see Table 4.3).

$f_{c, \max}$ (MPa)	$f_{c, \text{linear}}$ (MPa)	$f_{ctm}$ (MPa)	E (MPa)	$\nu$	G (MPa)
41.3	3.96	7.19	3455	0.3	1330

Table 4.3. Main mechanical parameters

## 4.2 Numerical results

The numerical simulation of the punch-through shear test aims at reproducing the behavior of the tested specimen using as input parameter the experimental results. Specifically, since the main focus is on the evaluation of the “cold joints” behavior, i.e. the material which composes the link between two layers of concrete, the punch-through test was carried out in order to measure the value of the critical energy release rate of Mode II, i.e.  $G_{IIc}$ , that is the parameter which the mechanical performances of joints are inherently dependent from. Therefore, a cohesive surfaced based model is used to simulate the joints’ behaviour (see §4.1.1). Besides, the same test is simulated on an element without joints, i.e. made out of plain concrete, in order to assess the influence and the effects of interfaces on a concrete element.

The analyses are modelled by means of a FEM software, i.e. ABAQUS.

### 4.2.1. Bulk concrete Element

The first simulation refers to the punch-through shear test on a plain concrete specimen. The modelling task starts with the definition of the parts which makes up the body, in this case only one part is created whose dimension are 140 x 140 x 50 mm (Figure 4.11). These dimension are exactly the height, the width and the average depth of the tested specimens.

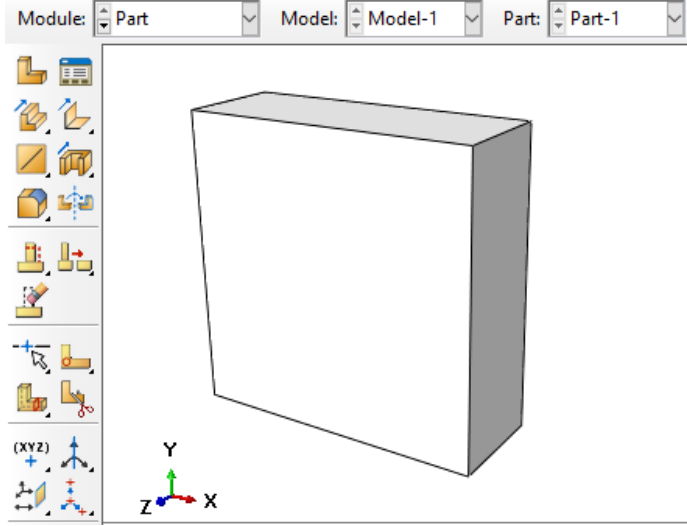


Figure 4.11 Bulk concrete element implemented in Abaqus

Afterwards, the material properties module is filled out using the CDP model for the nonlinear part of the material behaviour (model which is described in the previous section of this dissertation). For the elastic parameter a Young's modulus of 3455 MPa and a Poisson's coefficient of 0.3 are adopted. For simplicity the main parameters of both the elastic and non-elastic behaviour of the modelled material are reported in the following tables.

$f_{c, \max}$ (MPa)	$f_{c, \text{linear}}$ (MPa)	$f_{ctm}$ (MPa)	$E_{cm}$ (MPa)	$\nu$	$\rho$ (g/mm <sup>3</sup> )
41.3	3.96	7.19	3455	0.3	2.60E-05

Table 4.4. Mechanical material properties

Tension Stiffening		Tension Damage	
Stress (MPa)	Cracking Strain	Damage	Cracking Strain
7.190	0.000	0.000	0.000
5.6854	0.0006	0.0418	0.0006
3.0007	0.0019	0.1165	0.0019
1.7259	0.0033	0.1519	0.0033

0.4526	0.0081	0.1874	0.0081
0.1132	0.0128	0.1968	0.0128

Table 4.5. Tensile Strength input data for CDP model

Compression Stiffening		Compression Damage	
Stress (MPa)	Crushing Strain	Damage	Crushing Strain
34.964	0.0000	0.000	0.000
37.776	0.00007	0.000	0.00006
38.039	0.00009	0.000	0.00009024
38.336	0.00010	0.000	0.00010427
39.817	0.00028	0.000	0.00027544
41.245	0.00086	0.000	0.00086220
41.359	0.00123	0.000	0.00122900
40.331	0.00263	0.025	0.00262666
36.998	0.00459	0.105	0.00459143
30.946	0.00834	0.252	0.00834310
27.994	0.01220	0.323	0.01219736
26.748	0.01456	0.353	0.01455800
26.192	0.01572	0.367	0.01571898
26.029	0.01607	0.370	0.01606615
25.966	0.01618	0.372	0.01618438
25.917	0.01630	0.373	0.01629868
25.865	0.01641	0.374	0.01641364
25.812	0.01653	0.375	0.01652900
17.694	0.03418	0.572	0.03417876
4.428	0.06302	0.893	0.06301823
2.000	0.09453	0.951	0.09453

Table 4.6. Compressive Strength input data for CDP model

The next module refers to the assignment of a loading step in which also the loading typology is specified. A static load is adopted and besides the nonlinear geometry option is ticked, the latter refers to whether the little displacement hypothesis should be considered or not by the software. Concerning the time of the simulation, has been adopted 100 s with an increment size for each step of 0.5 s.

The next step is the mesh size definition, in which a variable size is adopted, indeed since a concentrated nonlinearity is expected in specific zones of the specimen the density of the mesh is increased in order to achieve the numerical convergence without numerical instabilities.

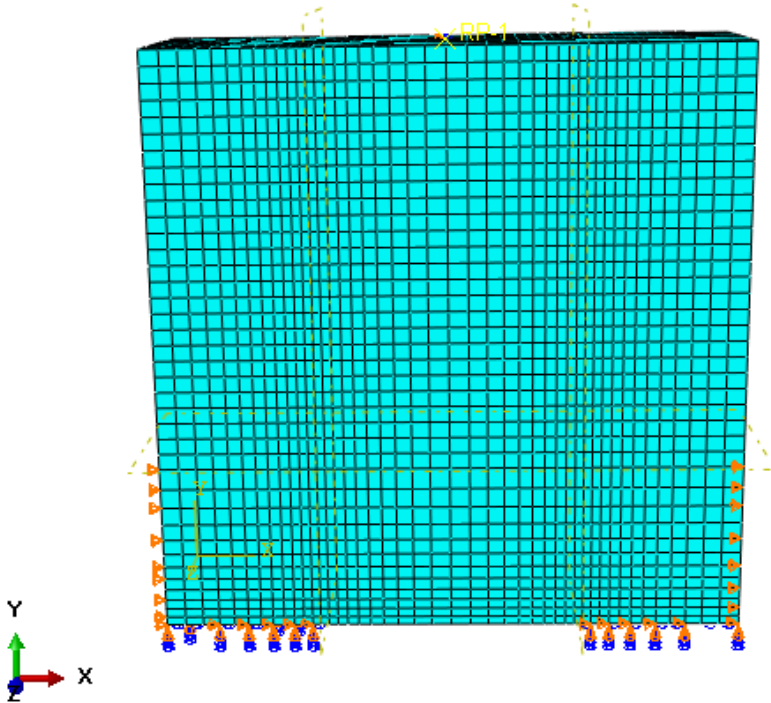


Figure 4.12 Plain concrete specimen: mesh and boundary conditions

In Figure 4.12 the mesh sizes and the boundary conditions are shown. The mesh size, along the X axis, starts from 5mm at the exterior vertical edges ending to 2mm at the two YZ planes located at the inner edges of the bottom supports. The same range of mesh size is adopted from the centre of the specimen to the same two YZ planes. Throughout the height of the specimen the mesh size is uniform and equal to 5mm except for the bottom part in which the mesh size is 2mm.

The boundary conditions (shown in Figure 4.13) are manifold. At the bottom there are two support zones, in detail they are two surfaces of 38mm by 50mm placed symmetrically to the two ends of the base, these two surfaces are constrained in direction  $U_1$  and  $U_2$ , besides the rotation around Z axis is inhibited. Moreover, all the nodes included in the two exterior surfaces, from the bottom to

40mm height are inhibited to move in the X direction. The last constrain is applied to two nodes included in the lower face along the direction Z in order to prevent rigid body motions.

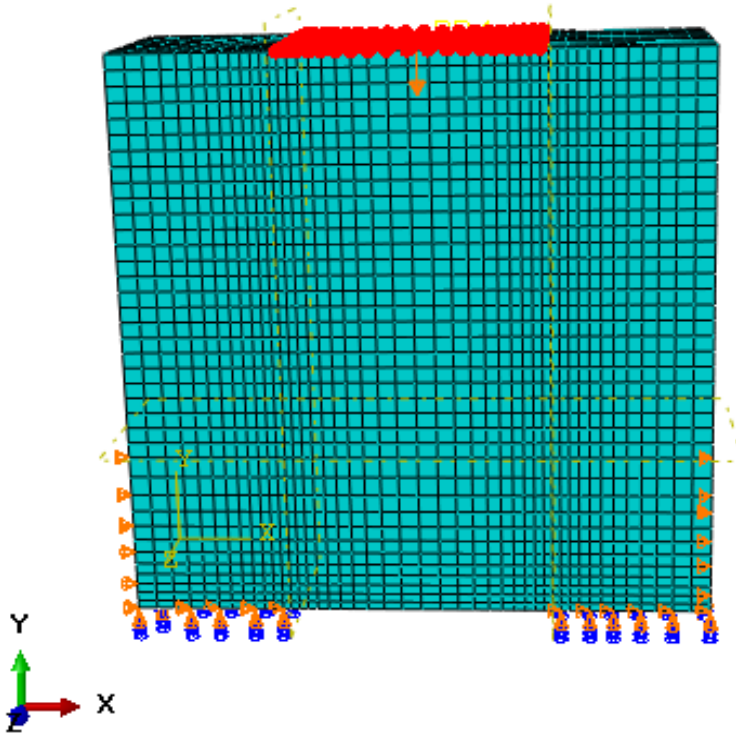


Figure 4.13 Upper rigid body which simulates the loading plate

The loading is performed in displacement control, i.e. a displacement is applied, in correspondence to each displacement incrementation step the load is computer as sum of the vertical reaction acting at the nodes of the supports. A maximum displacement of 1.5mm is applied at a reference point placed at the centre of the upper face of the element.

The reference point is linked to a set of nodes creating a rigid body able of moving in a rigid way without deformations, this rigid body stand for simulating the loading platen of the experimental test.

Besides, constrain in the X direction and another constrain for the rotation around the Z axis are applied to avoid rigid body motion (see Figure 4.13).

At this point the input file was ready to be submitted to the processing stage and then it was possible to evaluate the results. In Figure 4.14 the Load vs

Displacement curve is presented.

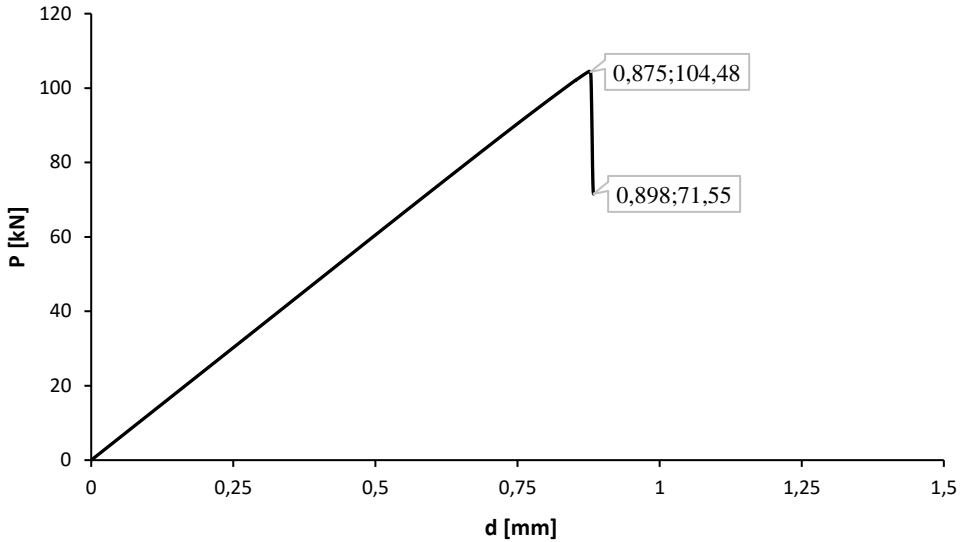


Figure 4.14 Load-displacement curve of Punch-Through test simulation of plain concrete

The peak of the curve occurs at the 98th step of the analysis and is equal to 104.48 kN, whereas the quasi-horizontal branch happens at the 71.55 kN at the 196th step.

In the following figures the evolution of the vertical displacement is presented first, then the propagation of cracks is pictured, in particular in correspondence with 3 steps, i.e. Step 37 (cracks opening), Step 98 (at the maximum load) and Step 538 which is the last one of the analysis.



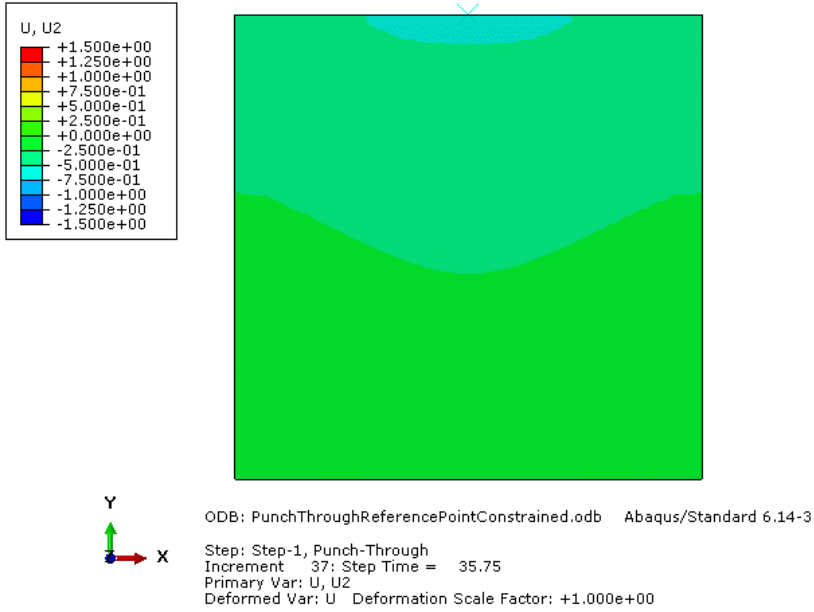


Figure 4.15 U2 evolution in Punch-through test simulation, plain concrete at 37th step

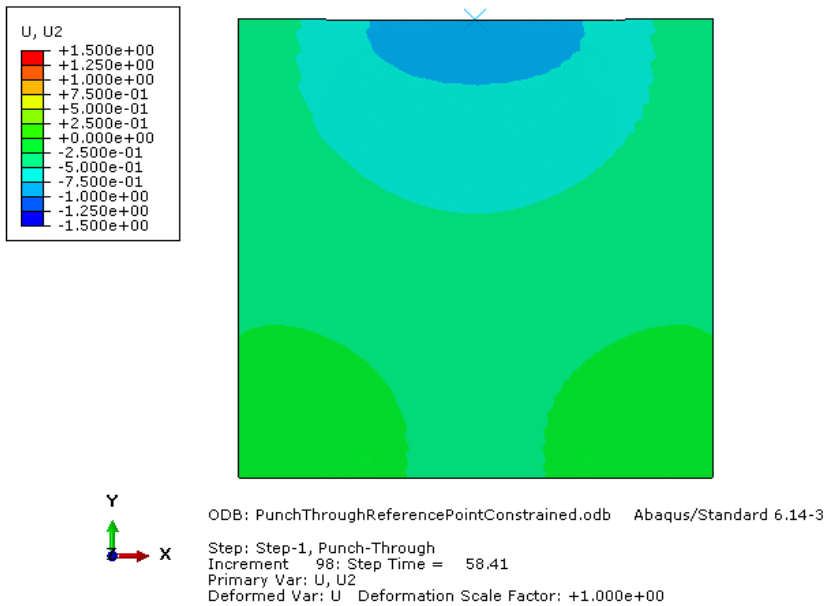


Figure 4.16 U2 evolution in Punch-through test simulation, plain concrete at 98th step

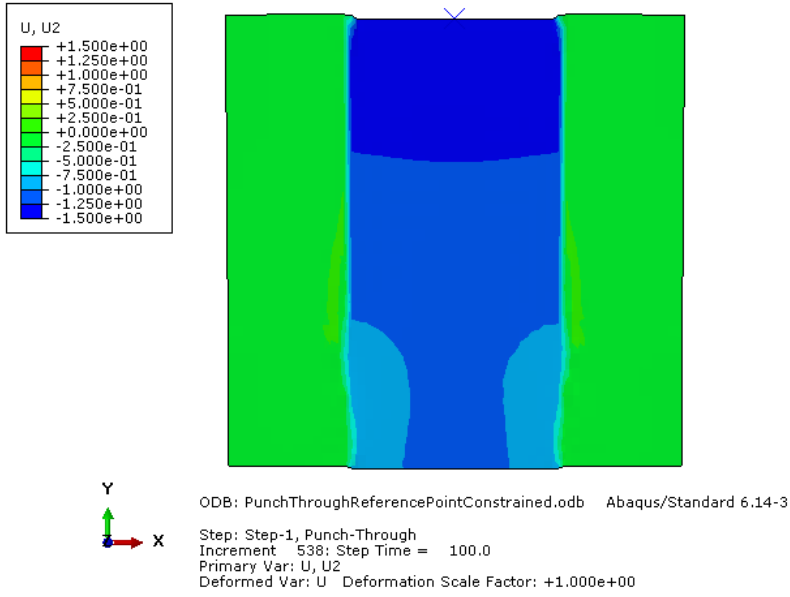


Figure 4.17 U2 evolution in Punch-through test simulation, plain concrete at 538<sup>th</sup> step

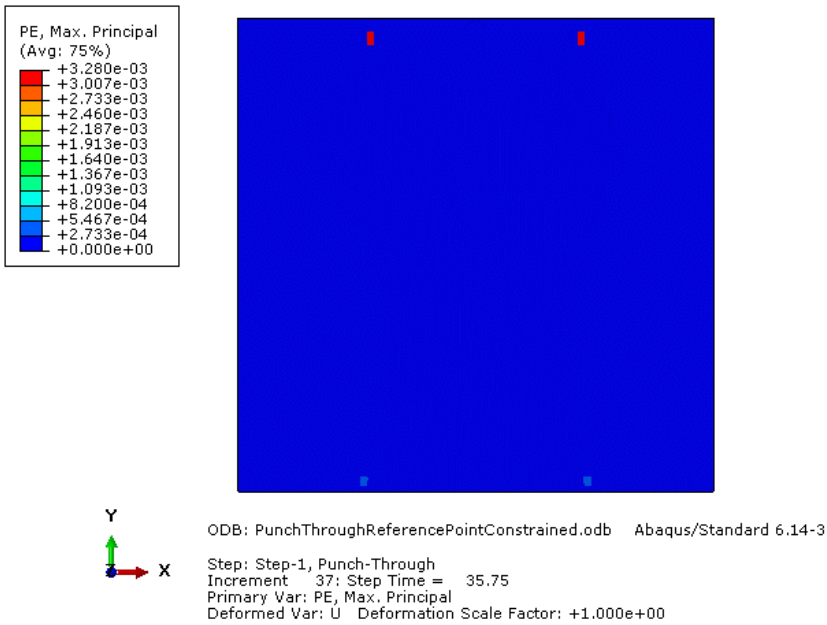


Figure 4.18 Cracks evolution, punch-through test simulation, plain concrete at 37<sup>th</sup> step

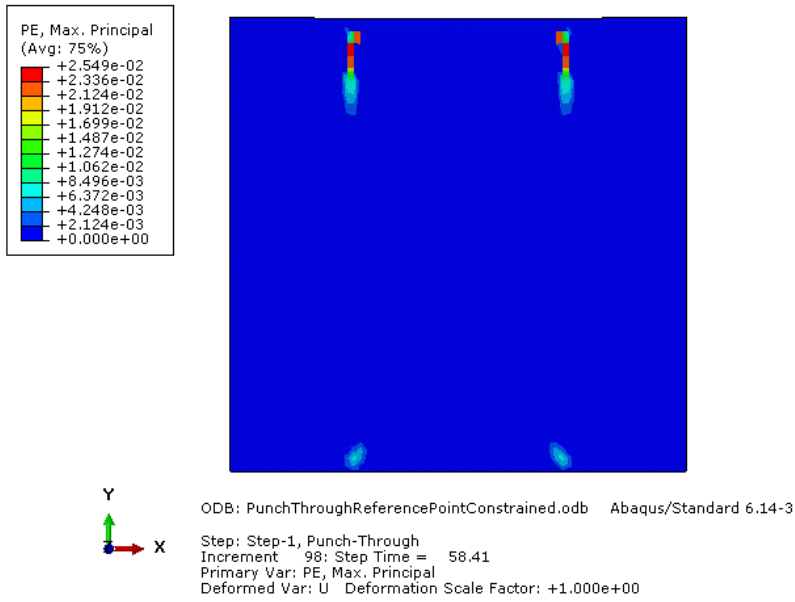


Figure 4.19 Cracks evolution, punch-through test simulation, plain concrete at 98th step

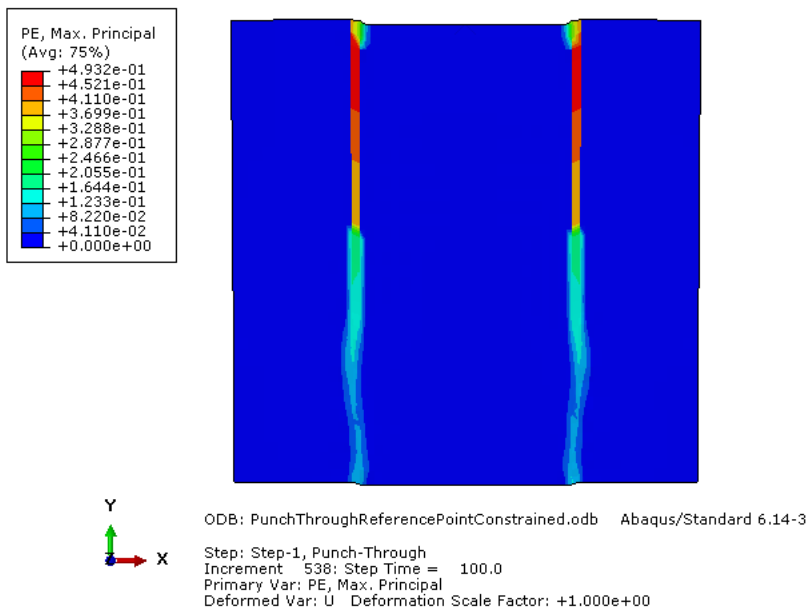


Figure 4.20 Cracks evolution, punch-through test simulation, plain concrete at 538th step

The previous figures show how the cracks start and propagate along the expected planes of fracture, namely the planes between the end of the bottom supports and the upper loading plate. Moreover, the cracks diffusion in correspondence to the maximum load in the load vs displacement curve is confined to a narrow portion of the fracture planes. This means that the failure is attained before the cracks diffuse through the entire height of the body. After the stage of the maximum load an almost vertical drop is observed in term of bearing capacity of the body, which corresponds to the propagation of the cracks until the entire body is teared apart across the planes of fracture. Seeing the distribution of the vertical displacement in Figure 4.15, it is possible to notice that at the beginning of the simulation the vertical displacement are distributed by levels like a common compressive test in which the body is compressed and it deforms accordingly, hence a maximum displacement at the top, followed by a decreasing displacement along the vertical direction. In step 98th (Figure 4.16) the distribution of displacement changes, the maximum value of  $U_2$  is still beneath the “loading plate” but this this is confined between the two planes of fracture. Besides, the displacement above the supports are zero whereas the middle section of the body starts to experience some vertical displacement. In Step 538 (Figure 4.20) the vertical displacement distribution clearly shows that the entire volume under the loading plate has a quasi-rigid shift compared to the lateral parts of the body.

#### ***4.2.2. Layered concrete Element***

The second simulation is about the layered element aimed to reproduce the tested punch-through shear specimen. The body was modelled as seven distinct parts, each of which is 20mm wide, 140mm high and 50mm deep (Figure 4.21left).

Afterwards, the parts are assembled side by side in order to create the final shape of the specimen, i.e. 140 x 140 x 50 mm (Figure 4.21 right).

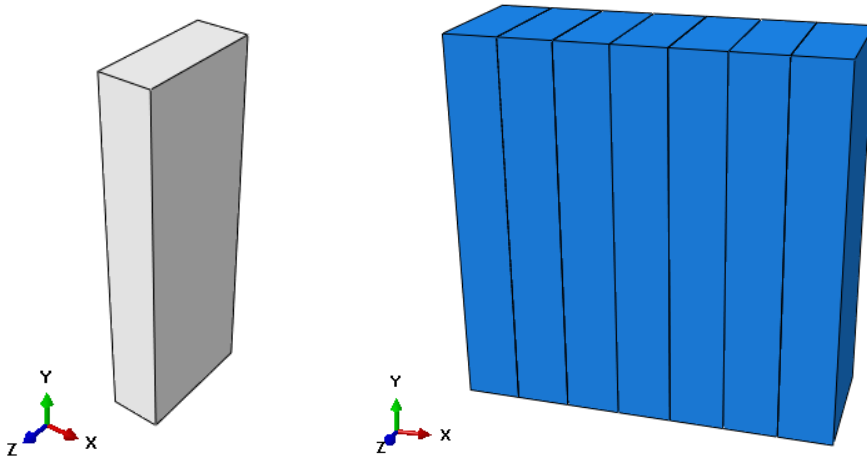


Figure 4.21 left: Single element part; right: Assembly

The material that makes up each layer is the same adopted in the previous simulation, i.e. CDP model parameters. The difference with respect to the last simulation consists in the presence of contact surfaces which are indeed the core of such simulation since the main object of the herein thesis is to characterize the behaviour of the junctions between layers. In order to define the interaction properties, the surfaces must be created therefore twelve surfaces are set, each one represent one out of the two surfaces that come in contact during the simulation (Figure 4.22).

Mesh-wise, each part has been divided in elements of 5 by 5 mm except for 5 mm of each side of the expected surfaces of failure where the elements are 1.25mm with respect to the x axis (Figure 4.23).

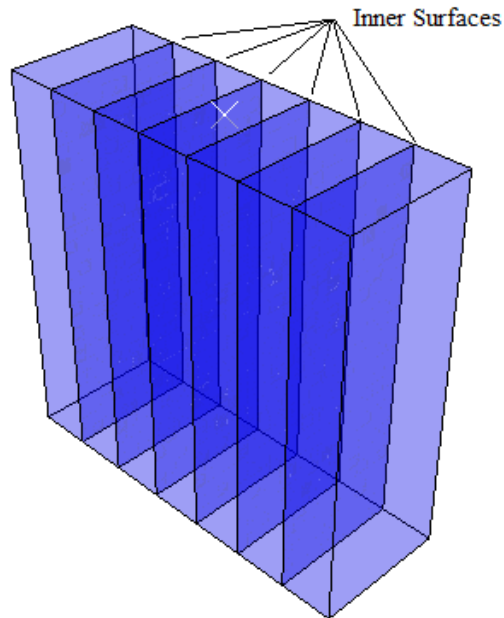


Figure 4.22 Surfaces

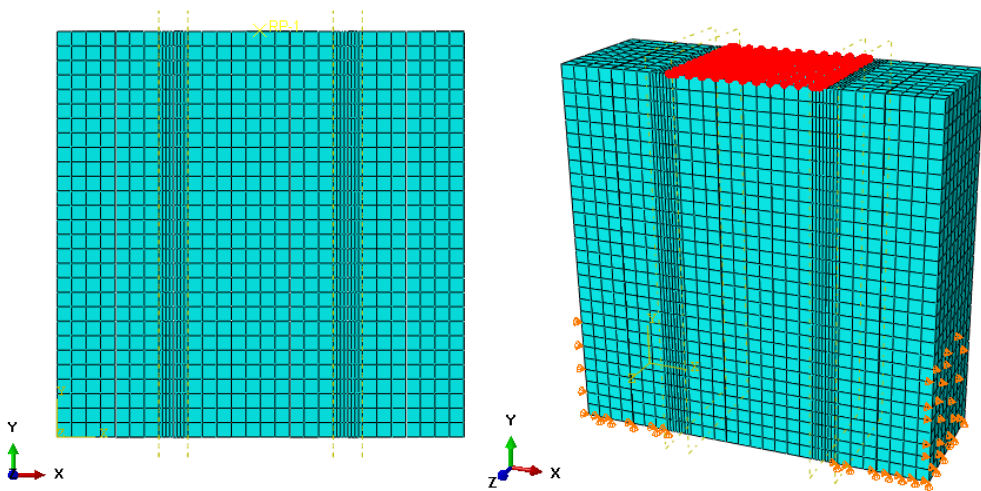


Figure 4.23 left: Mesh size of the specimen; right: Boundary conditions of the layered specimen

The boundary conditions are quite similar to those applied for the simulation of the plain concrete specimen. Indeed, at the bottom two supports are applied from the exterior edges of the body to the node before the failure surfaces, constraining the vertical displacement. The lateral supports are set to the lateral surfaces from the bottom to the height of 40mm, constraining the movement along the X axis. Besides, two points included in the bottom face of the body are constrained to move along the Z axis in order to avoid rigid body motion. At the top a rigid plane of 57.5 mm large aimed to simulate the loading plate is set. Its width corresponds to the width of the 3 middle layers minus the size of two mesh elements (Figure 4.23 right).

The testing process is simulated in displacement control, i.e. a growing displacement is applied at the upper rigid surface. The applied displacement grows linearly up to 3 mm of downward displacement. The loading process develops in 10 seconds, which is the time set for the fulfilment of the simulation.

Afterwards, the interaction properties are defined. These properties govern the behaviour of the layers interaction, i.e. joints of the specimen. The adopted interaction is the cohesive surface-based model which requires the definition of the traction-separation law, as described in section §4.1.1.

Therefore, multiple parameters must be defined: the initial stiffness of the traction-separation laws with refer to the three modes of fracture; then the damage initiation stresses and the critical energy.

The initial stiffnesses  $K_{nn}$ ,  $K_{tt}$  and  $K_{ss}$ , that refer to Mode I, Mode II and Mode III respectively, are defined as the material stiffness divided by the thickness (hereafter referred to as  $s$ ) of the cohesive layer. More precisely:

$$K_{nn} = \frac{E}{s} \quad (38)$$

$$K_{tt} = K_{ss} = \frac{G}{s} \quad (39)$$

The Young's modulus is equal to 3455 MPa whereas the shear modulus is computed by using the elastic relation  $G=E/2(1-\nu^2)$  and it is equal to 1330 MPa. Since it is used a surface based model instead of having a cohesive element with a defined thickness, the interaction is modelled as a sticky surface with no thickness. Therefore a very small thickness is hypothesised, i.e. 0.01mm for each

surface. With the latter assumption the resulting stiffnesses of the traction-separation laws are:

$$K_{nn} = 172750 \frac{MPa}{mm} \quad (40)$$

$$K_{tt} = 66500 \frac{MPa}{mm} \quad (41)$$

$$K_{ss} = 66500 \frac{MPa}{mm} \quad (42)$$

The critical energy release rate  $G_{IIC}$  is taken equal to the  $1.7 \text{ [J/mm}^2\text{]}$ , i.e. the mean value experimental results. This critical energy is supposed equal to the total critical energy which considers the three modes of fracture altogether. This assumption is based on the fact that the Mode II of fracture is the predominant mechanism implying that the other two modes are negligible.

The last parameters to be defined are the damage initiation stresses,  $t_n$ ,  $t_t$  and  $t_s$ , which refer to the damage initiation stresses of Mode I, Mode II and Mode III respectively. These parameters refer to the uniaxial tensile strength with regards to Mode I and the pure shear stress for Mode II and Mode III. Given that,  $t_n$  is equal to the tensile strength evaluated from the experimental tests;  $t_t$  and  $t_s$  are estimated by using a relation given by I. Yoshitake et al. (2011) (Yoshitake et al. 2011), i.e.  $\text{ShearStrength} = 0.83 \text{ TensileStrength}$ . In definitive:

$$t_n = 7.19 \text{ MPa} \quad (43)$$

$$t_t = t_s = 5.9 \text{ MPa} \quad (44)$$

At this point the input database are ready to be submitted to the Abaqus processing stage then the results of the simulation can be viewed.

The first result herein showed is the distribution of the vertical displacement at different steps of the analysis and the vertical stress, i.e. along the Y axis (Figure 4.24, Figure 4.25, Figure 4.26, Figure 4.27). Four principal steps are taken into account: 1<sup>st</sup> step, 12<sup>th</sup> step, 27<sup>th</sup> step and 83<sup>rd</sup> step which refer to the first step, the step at which respectively the fractures begin, the step corresponding to the peak of the load vs displacement curve and the step before the complete failure.



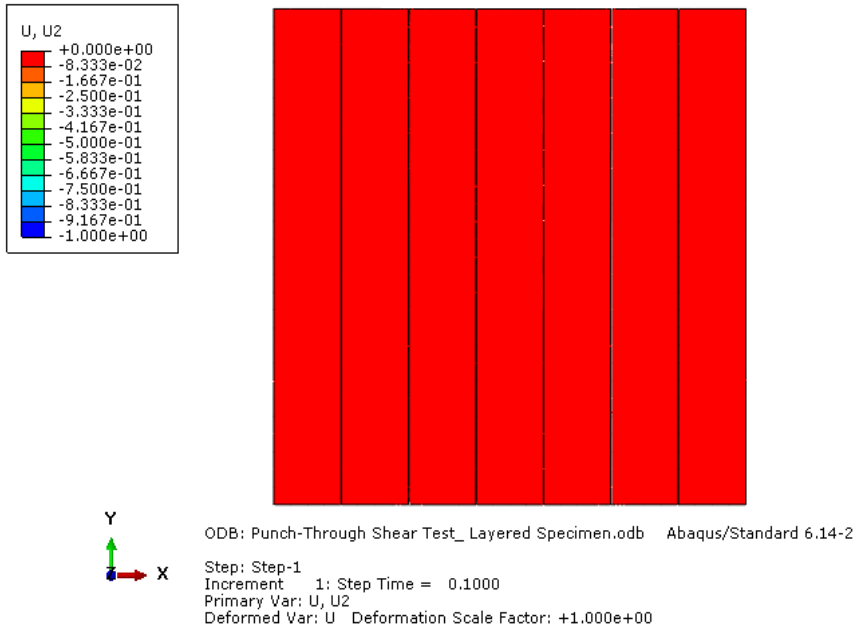


Figure 4.24 Vertical displacement distribution 1<sup>st</sup> Step

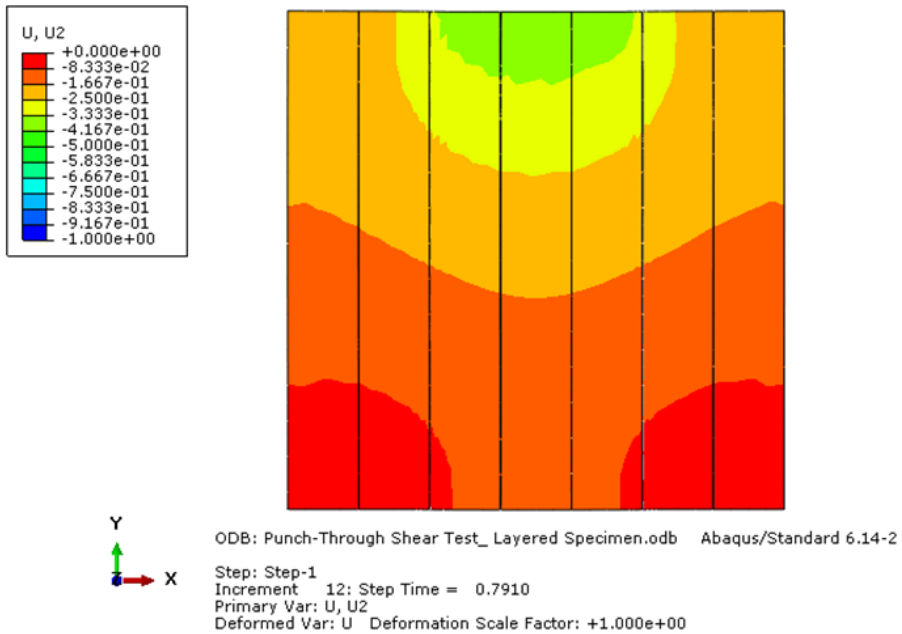


Figure 4.25 Vertical displacement distribution 12<sup>th</sup> Step

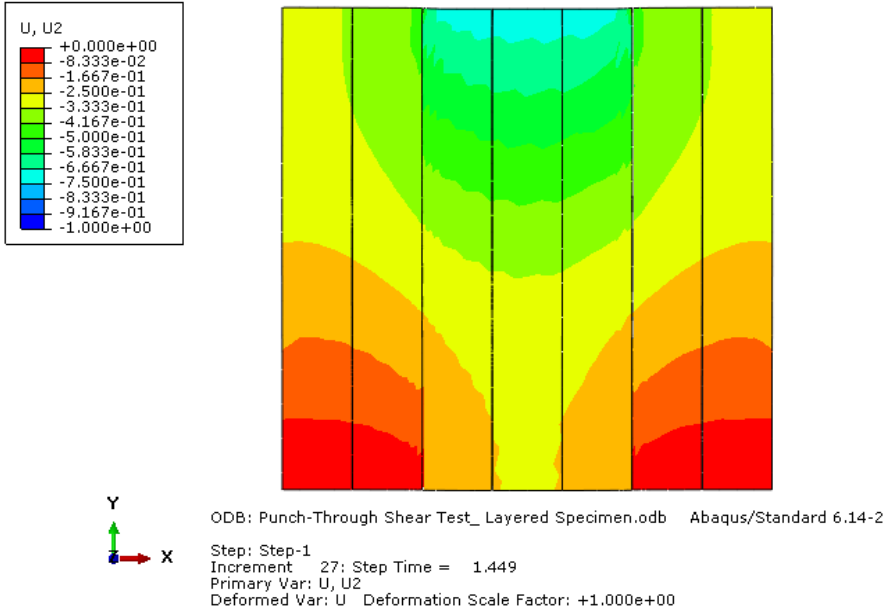


Figure 4.26 Vertical displacement distribution 27<sup>th</sup> Step

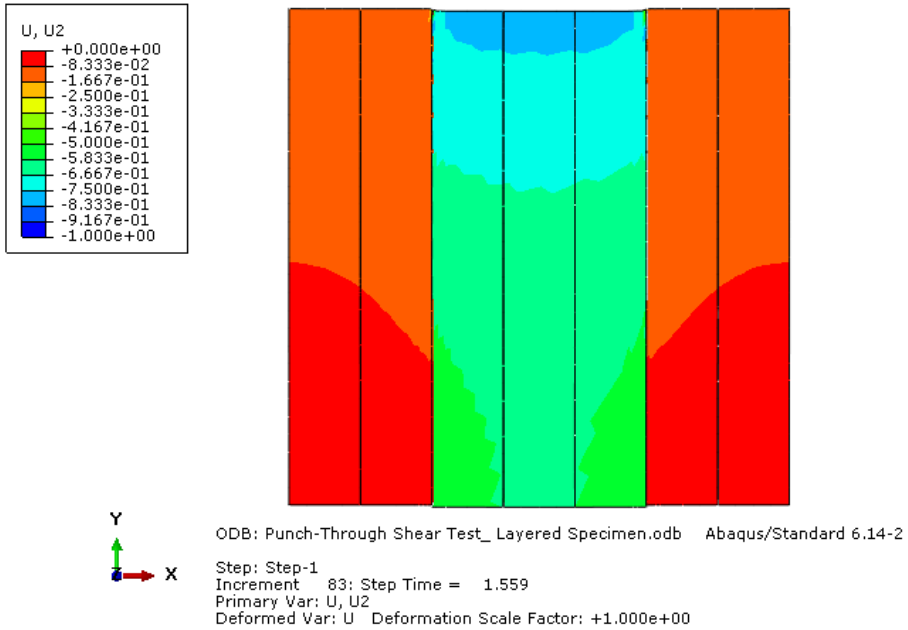


Figure 4.27 Vertical displacement distribution 83<sup>rd</sup> Step

As can be noticed from the figures the vertical displacement distribution is continuous and homogeneous in step 1 and 12 which means that the specimen behaves like a plain concrete element until the cracks occur. In the 27<sup>th</sup> step the distribution is not continuous, it is discrete instead, and continuous only within the three layers in the middle and in the two edge layers, at each side of the specimen. In the last step the middle layers are completely separated from the rest of the body implying that no equilibrium can be reached since there is no means of transferring stresses across the interfaces. In the following figures the shear stress distribution along the axis Y on the fracture surfaces are shown with refers to the same time steps.

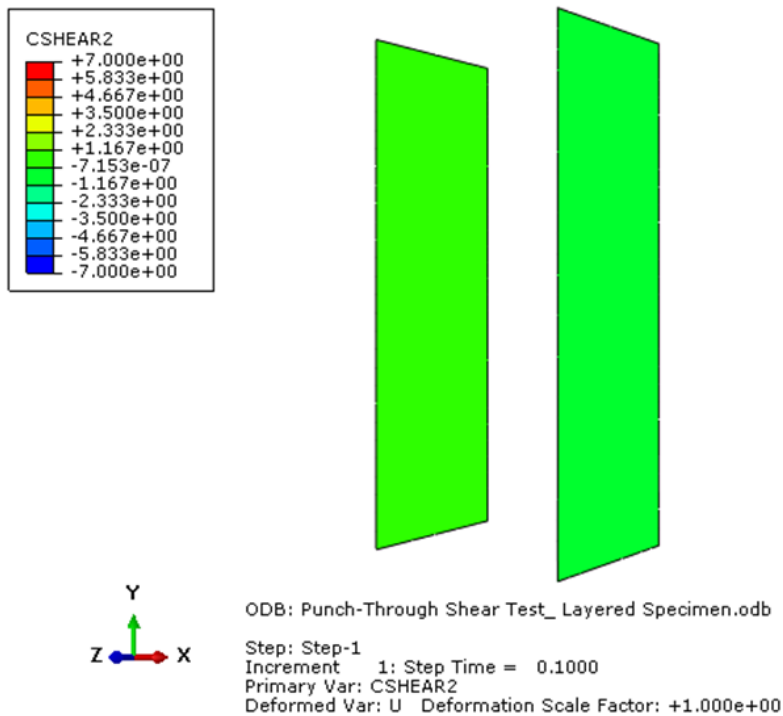


Figure 4.28 Shear stress distribution through fracture surfaces at 1<sup>st</sup> Step

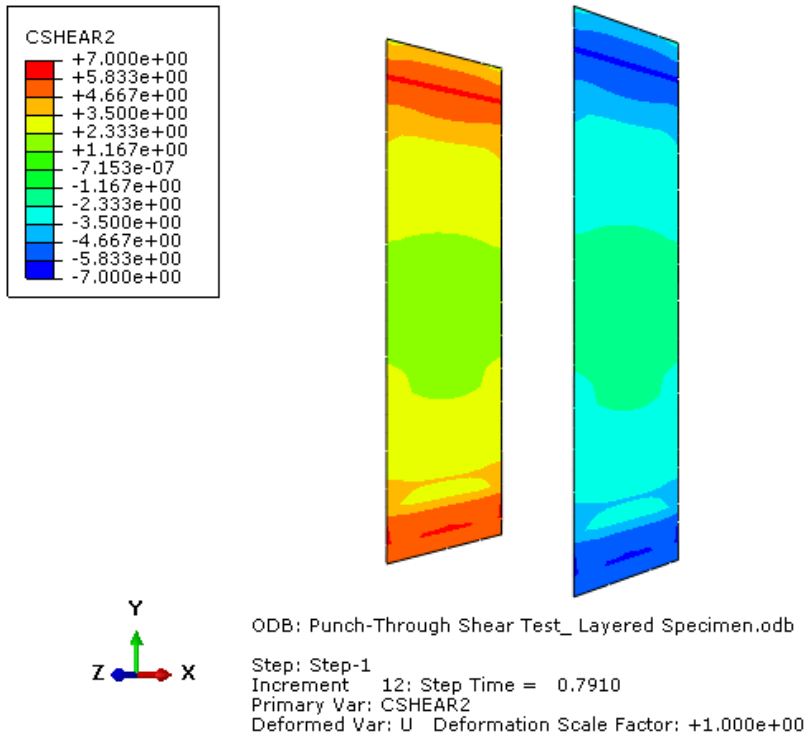


Figure 4.29 Shear stress distribution through fracture surfaces at 12<sup>th</sup> Step

In the 12<sup>th</sup> time step (Figure 4.29), which refers to the cracks initiation, shear stress accumulates at the border of the surface attaining the damage initiation stress of 5.9 MPa. This means that fractures begin at the top and at the bottom of the body at the same time. At the 27<sup>th</sup> step the maximum shear stresses are located in the middle side of the surfaces meaning that the fracture have propagated toward the centre of the body. The part of the surfaces that have already been affected by the fractures are not free of stresses, instead they show post-failure stress stresses. This behaviour reflects the adopted interaction model, in fact cohesive surfaces can transfer stresses after the crack opening according to the softening branch of the traction-separation law.

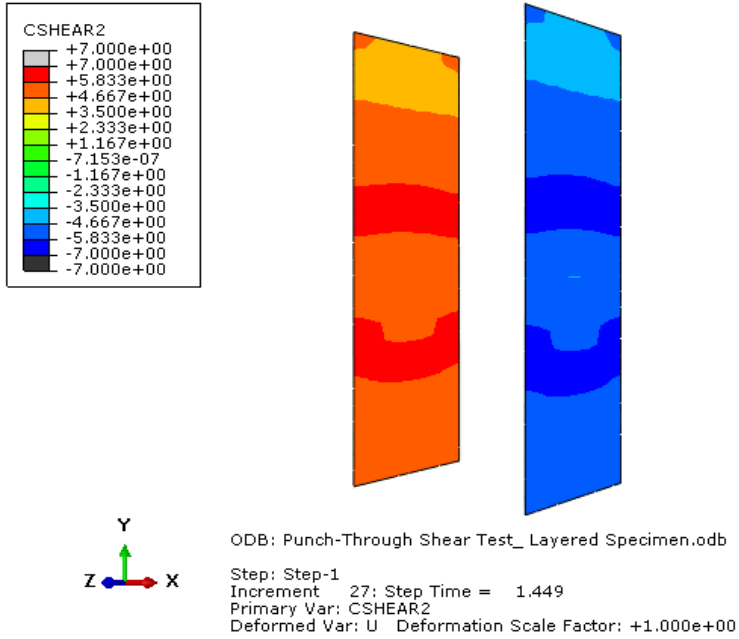


Figure 4.30 Shear stress distribution through fracture surfaces at 27<sup>th</sup> Step

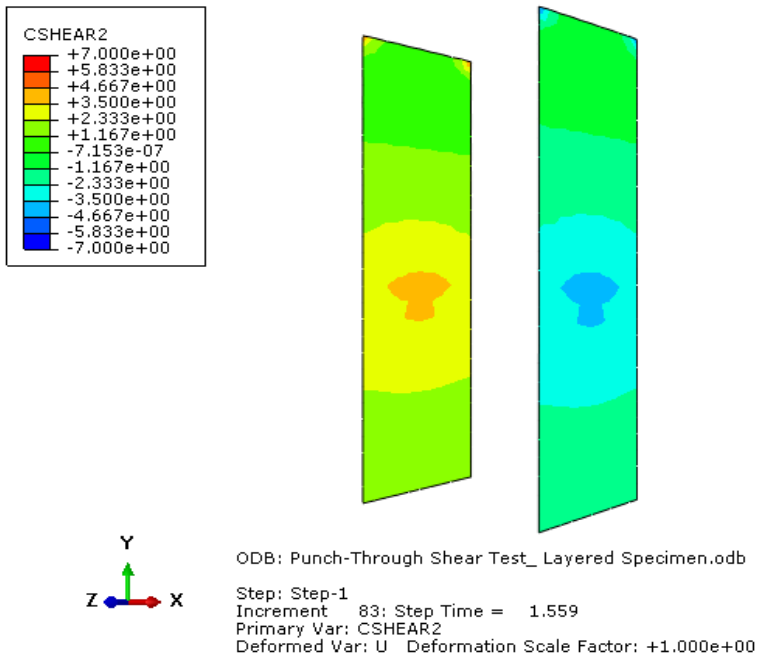


Figure 4.31 Shear stress distribution through fracture surfaces at 83<sup>rd</sup> Step

At the 83<sup>rd</sup> step, shear stress is near to zero over the entire failure surfaces except for the centre of them where there still is 3.5 MPa of shear stress. At 84<sup>th</sup> step no stresses are acting on the failure surfaces as result of the complete detachment of the layers.

The principal outcome of the simulation is the load vs displacement plot which is the reference curve for both the experimental and the numerical test. Since the simulation is performed in displacement control the load is computed as sum of the vertical reaction at each node of the bottom supports whilst the vertical displacement is evaluated at the central node of the upper surface.

In Figure 4.32 the load vs displacement is reported, on which the points corresponding to the cracks initiation step and the maximum load are marked. The values of the crack initiation load and the maximum load are reported in Table 4.7.

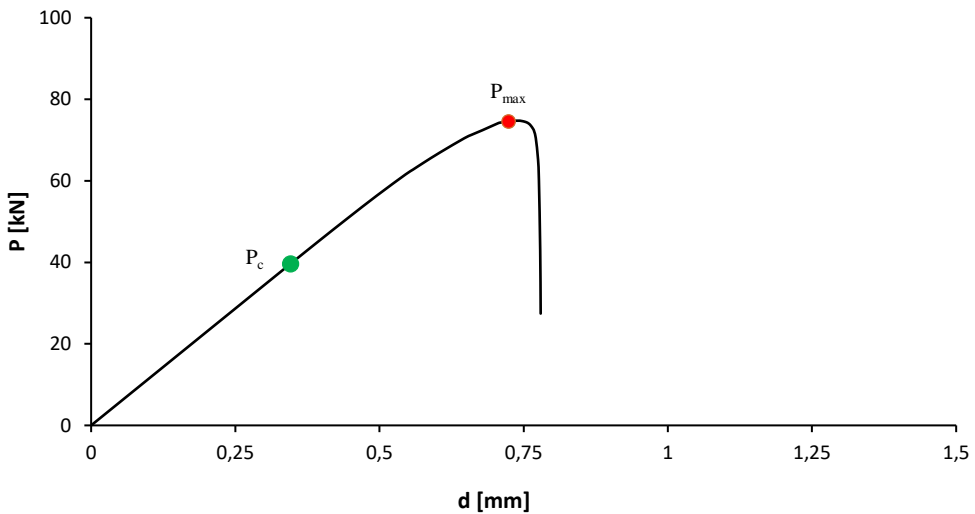


Figure 4.32 Load vs Displacement curve, layered specimen simulation

$P_c$	$d(P_c)$	$P_{max}$	$d(P_{max})$
(kN)	(mm)	(kN)	(mm)
39.61	0.35	74.75	0.74

Table 4.7. Crack initiation load and maximum load

## References

- Bažant, Z. P. 2001. "Concrete Fracture Models: Testing and Practice." *Engineering Fracture Mechanics* 69 (2): 165–205. [https://doi.org/10.1016/S0013-7944\(01\)00084-4](https://doi.org/10.1016/S0013-7944(01)00084-4).
- Griffiths, A. A. 1995. "The Phenomena of Rupture and Flow in Solids." *Masínovedenie C* (1): 9–14. <https://doi.org/10.1098/rsta.1921.0006>.
- Hillerborg, A., Modéer M., and Petersson P. E.. 1976. "Analysis of Crack Formation and Crack Growth in Concrete by Means of Fracture Mechanics and Finite Elements." *Cement and Concrete Research* 6 (6): 773–81. [https://doi.org/10.1016/0008-8846\(76\)90007-7](https://doi.org/10.1016/0008-8846(76)90007-7).
- Irwin, G. R. 1968. "Linear Fracture Mechanics, Fracture Transition, and Fracture Control." *Engineering Fracture Mechanics* 1 (2): 241–57. [https://doi.org/10.1016/0013-7944\(68\)90001-5](https://doi.org/10.1016/0013-7944(68)90001-5).
- Jankowiak T, Lodigowski T. 2005 Identification of Parameters of Concrete Damage Plasticity Constitutive Model. *Foundation of civil and environmental engineering*, 2005, No. 6
- Karihaloo, B. L., and Nallathambi P.. 1991. "Test Methods for Determining Mode I Fracture Toughness of Concrete." In *Toughening Mechanisms in Quasi-Brittle Materials*, 91–124. Springer Netherlands. [https://doi.org/10.1007/978-94-011-3388-3\\_7](https://doi.org/10.1007/978-94-011-3388-3_7).
- Lee, J., Fenves G. L, and Member. 1998. "PLASTIC-DAMAGE MODEL FOR CYCLIC LOADING OF CONCRETE STRUCTURES."
- Yoshitake, I., Uno T., Scanlon A., Asce F, and Hamada S.. 2011. "Simplified Test of Cracking Strength of Concrete Element Subjected to Pure Shear." [https://doi.org/10.1061/\(ASCE\)MT.1943-5533.0000259](https://doi.org/10.1061/(ASCE)MT.1943-5533.0000259).





# Chapter 5

## INTERLAMINAR REINFORCEMENT SYSTEM

This chapter attempts to provide a solution for improving the interface bond between the layers by the definition of a strategy of interlaminar reinforcement implementation, since extrusion based 3DCP deposits the cementitious material layer by layer, forming a weak bond at interface.

Most current reinforcement concepts in additive manufacturing rely on conventional approaches, which unfortunately pose critical issues to the digitalization and automation of fabrication techniques. Some digital fabrication techniques using reinforced concrete have been developed, such as Smart dynamic casting, Mesh mould, External reinforcement, Printable fibre reinforced concrete (Asprone et al. 2018), but there is also a lack of specific focuses about the enhancing the interlayer strength in 3D printed concrete elements. Recently, efforts have been made to improve the bond between consecutive layers by increasing the mechanical contact between the layers (Zareiyan and Khoshnevis 2017) or applying a low-viscous mineral-based primer before deposition of each subsequent layer (Sanjayan et al. 2018), in order to increase surface area and mechanical anchorage for generating a bond strength of about 120% -180% higher than the no paste samples.

In this chapter, so a possible reinforcement system is proposed and tested. The adopted method consists of applying steel rods that pass across the junctions to investigate the effect of the steel elements on the shear resistance of joints.

The same experimental setup used to investigate the shear behavior of unreinforced printed elements is been adopted. The relative results have been correlated and validated by numerical simulation, showing an encouraging

increase in shear strength with respect to 3D elements without interlaminar reinforcement.

Finally, a comparison between experimental and numerical results is presented in terms of load-displacement plots and visualized through correlation of digital and simulated damage evolution.

Let's first see the results obtained from the experimental tests and the numerical simulations on the elements without reinforcement. The comparison between the different results showed that the response of tested specimens corresponds to the real behaviour effectively, relative to the mechanisms of failure exhibited and mechanical properties obtained, but mainly the results highlight the need of an approach for increasing the bond strength between layers.

In order to explain clearly this positive similarity, in the following figures are displayed the trend of the average experimental -acquired in terms of average values of stiffness- and numerical curves in the case of bulk material elements and for each group of specimens, characterized by the waiting time of 100s , 200s, 1800s and 3600s.

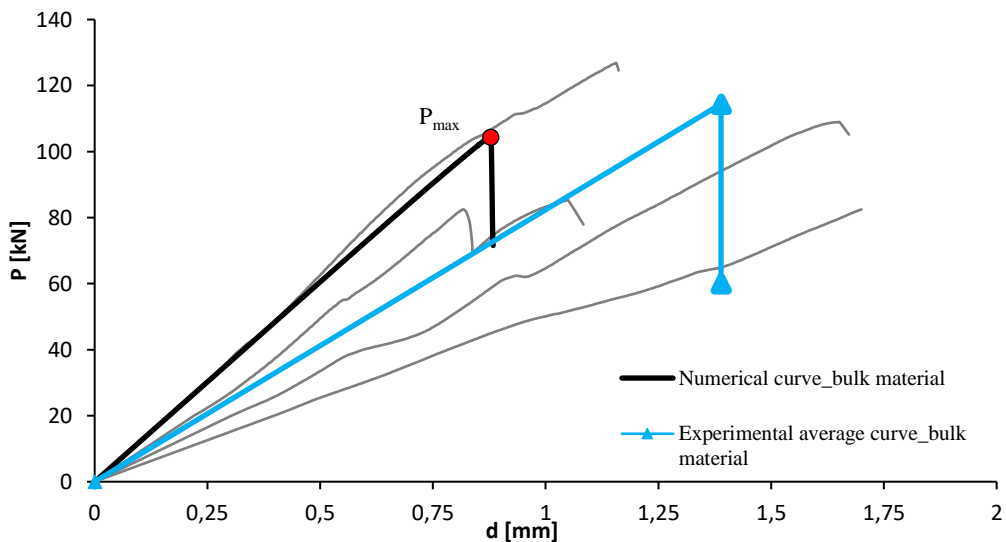


Figure 5.1 Experimental and numerical curve, bulk material specimen

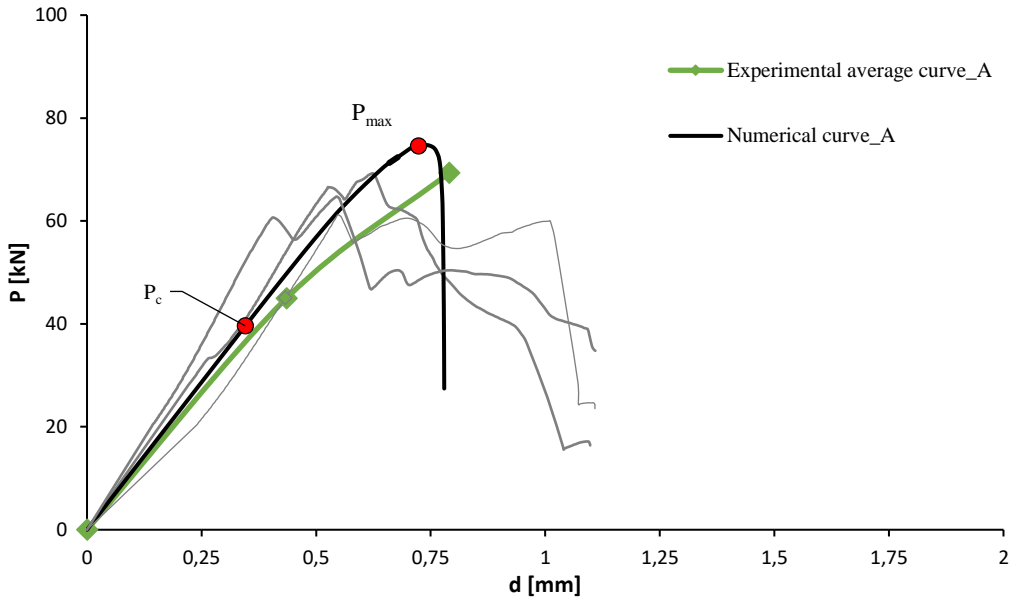


Figure 5.2 Experimental and numerical curve, un-reinforced specimen group A

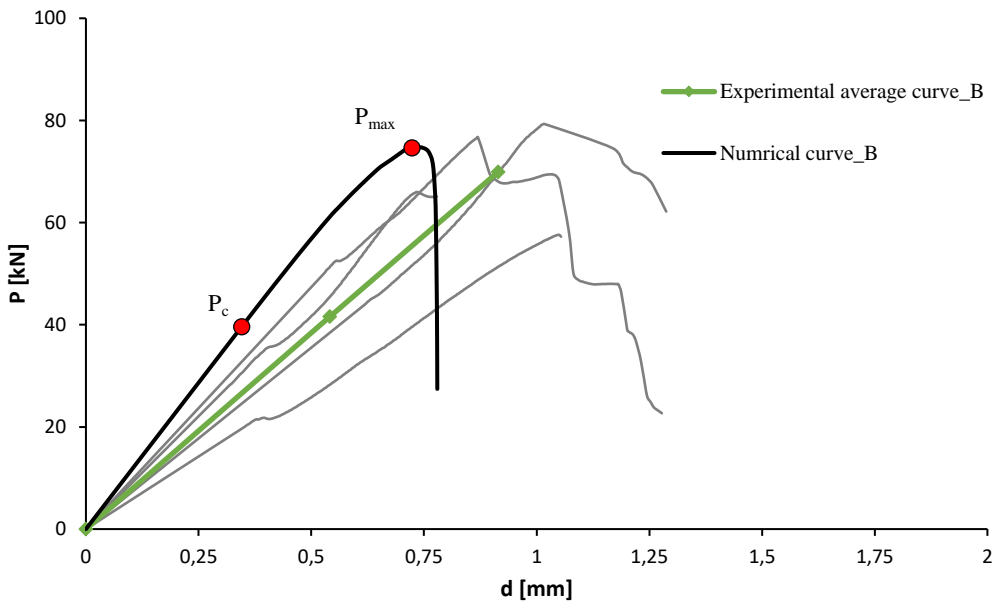


Figure 5.3 Experimental and numerical curve, un-reinforced specimen group B

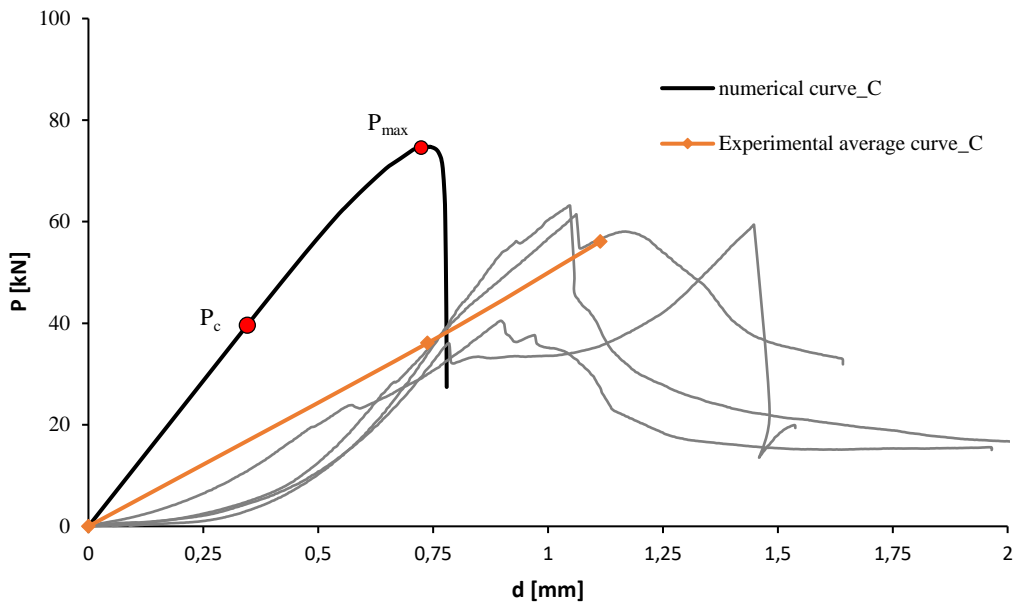


Figure 5.4 Experimental and numerical curve, un-reinforced specimen group C

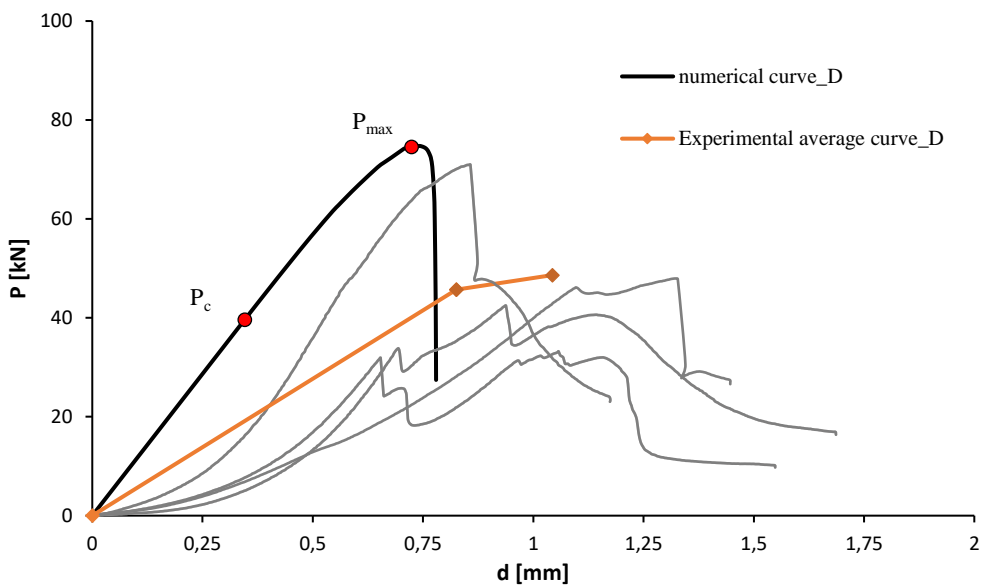


Figure 5.5 Experimental and numerical curve, un-reinforced specimen group D

From an initial mere visual analysis of data, the outcomes of the experimental test seem well approximate the numerical simulation of the elements, with regards to critical and maximum load, as also \* Subscript "ave" indicate average values

Table 5.1 confirms.

ID	Mean Experimental Results				Numerical Simulation			
	$P_{c,ave}^*$ (kN)	$dP_{c,ave}^*$ (mm)	$P_{max,ave}^*$ (kN)	$dP_{max,ave}^*$ (mm)	$P_{max}$ (kN)	$dP_{max}$ (mm)	$P_c$ (kN)	$dP_c$ (mm)
Series A	44,98	0,61	69,37	0,83	74,75	0,74	39,61	0,35
Series B	41,57	0,55	69,89	0,92				
Series C	36,1	0,74	56,09	1,11				
Series D	45,7	0,83	48,64	1,04				
Bulk	-	-	100,87	1,39				

\* Subscript "ave" indicate average values

Table 5.1. Critical and Maximum Load average values comparison

Specifically, the difference between experimental and numerical results is in the order of 6% in terms of maximum loads for elements with multiple layers and of around 10% in terms of critical loads.

Moreover, the simulation underestimates the displacement related to the  $P_c$  and  $P_{max}$ , nonetheless the experimental outcomes have shown a certain variability in term of displacement that could be ascribed to some experimental errors. In Table 5.1 is also reported the maximum load reached by the bulk material elements in the numerical simulation and experimental test, showing an inappreciable percentage difference and confirming the validity of the mathematical model proposed.

Another important data concern the higher maximum load value exhibited by the bulk material elements with respect to the printed elements, demonstrating the weakness of the joints in the 3D concrete structure and its influence on the mechanical performances, but mainly the actual need to study a reinforcement system, due to the low strength exhibited by the un-reinforced elements.

## 5.1 Experimental test and results

The entire experimental campaign to evaluate shear behavior of 3D printed elements with reinforcement was conducted at the Department of Structures of the University of Naples Federico II.

In order to carry out the experimental tests, prismatic specimens have been tested. In particular, 16 samples of 14 cm of length, 14 cm of width and 5 cm of thickness have been printed.

The material properties used for all specimen and the printing machine assets are described in §3.2.1 and in §3.2.2 respectively, but the printing settings aren't the same for all the specimens. Indeed, 4 groups of specimens, characterized by different resting times ( $t_{r1}=100s$ ,  $t_{r2}=200s$ ,  $t_{r3}=30min$  and  $t_{r4}=60min$ ) have been made.

Every printed element is made of 7 layers, of 2cm each, reaching a total height of 14 cm, and thick about 5cm. Furthermore, the printed samples are reinforced by inserting 5cm steel rods through the concrete layers and the layers joints. The steel rods are placed in such a way that every concrete layers' conjunction is crossed at least by 2 of them, as shown in the following figure.

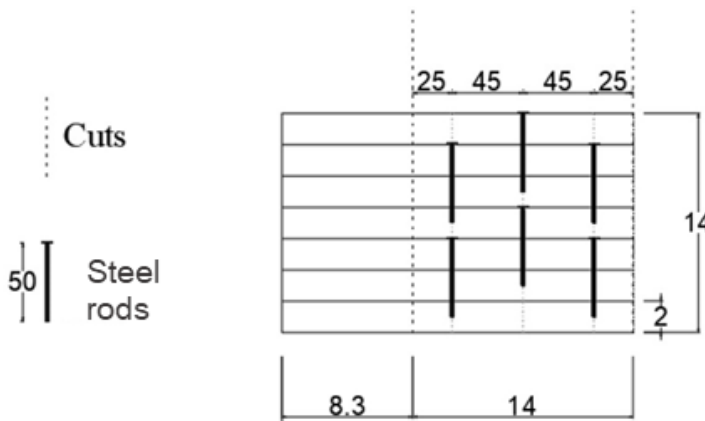


Figure 5.6. Rods system

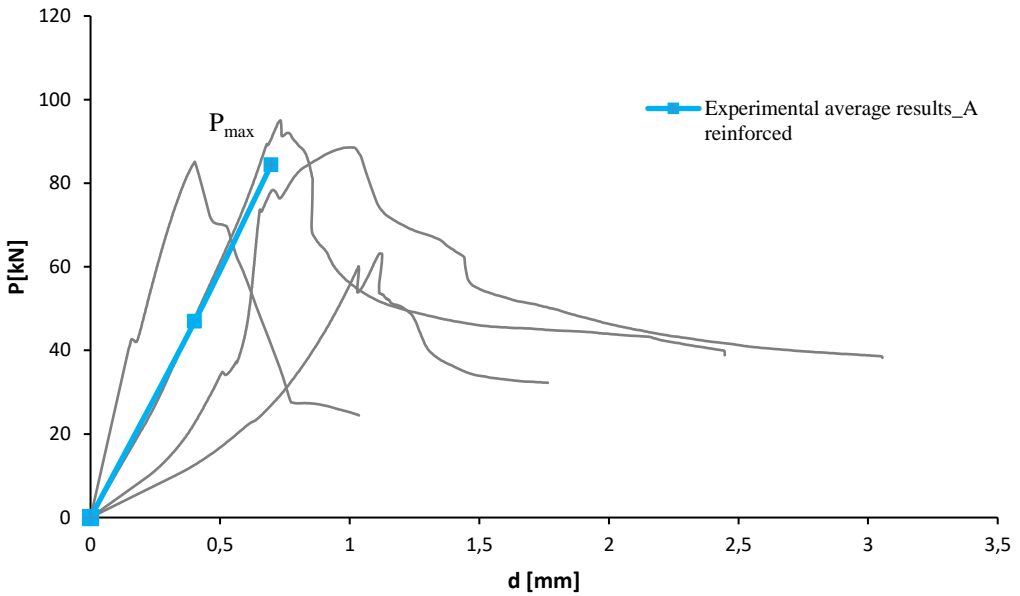
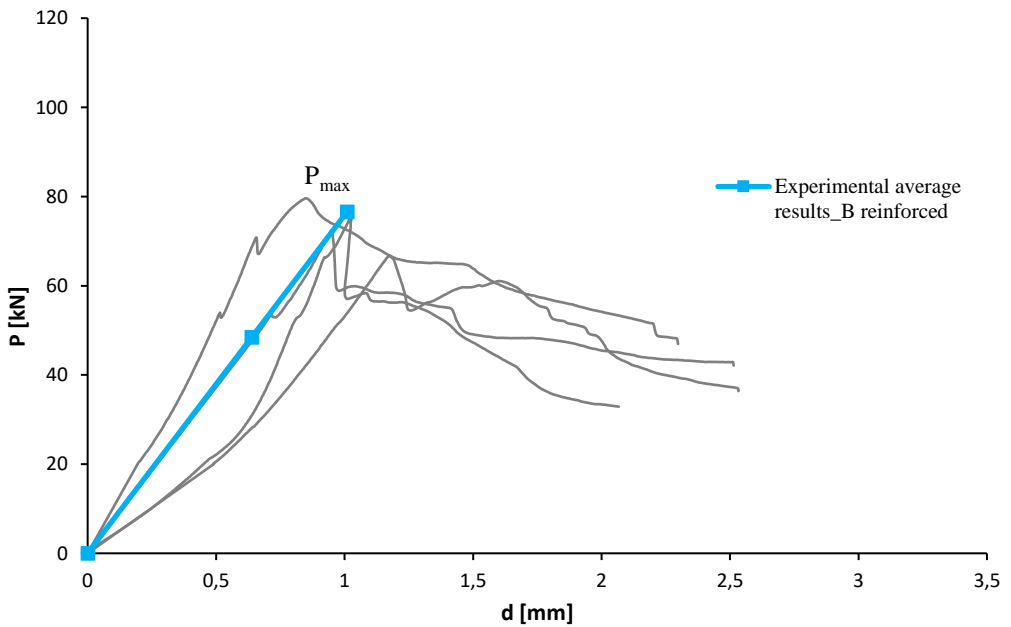
Table 5.2 shows clearly the characteristics of each reinforced sample, in terms of dimensional properties (total height  $H$ , layer height  $h$ , thickness  $d$ ) and process properties.

<b>Group of specimens</b>	<b>ID Elements</b>	<b>H (cm)</b>	<b>h (cm)</b>	<b>d (cm)</b>	<b>Waiting time (s)</b>	<b>Printing Speed (mm/m)</b>
A	A1_r	14	2	5	100	2000
	A2_r					
	A3_r					
	A4_r					
B	B1_r	14	2	5	200	2000
	B2_r					
	B3_r					
	B4_r					
C	C1_r	14	2	5	1800	2000
	C2_r					
	C3_r					
	C4_r					
D	D1_r	28	2	5	3600	2000
	D2_r					
	D3_r					
	D4_r					

Table 5.2. Main features of reinforced specimens

The specimens were subjected to the punch-through shear test (§3.1.1), in order to investigate the increase in shear strength due to the presence of rods system, bu using a vertical LVDT and digital image correlation technique (Mccormick and Lord 2010).

The findings of the tests carried out on printed reinforced elements are reported in the following plots in terms of Load-Displacement, where the different curves for each specimen of the same group and the relative average curve are presented.

Figure 5.7 Load-displacement curve, specimens group A\_reinforced ( $t_{r1}=100s$ )Figure 5.8 Load-displacement curve, specimens group B\_reinforced ( $t_{r2}=200s$ )



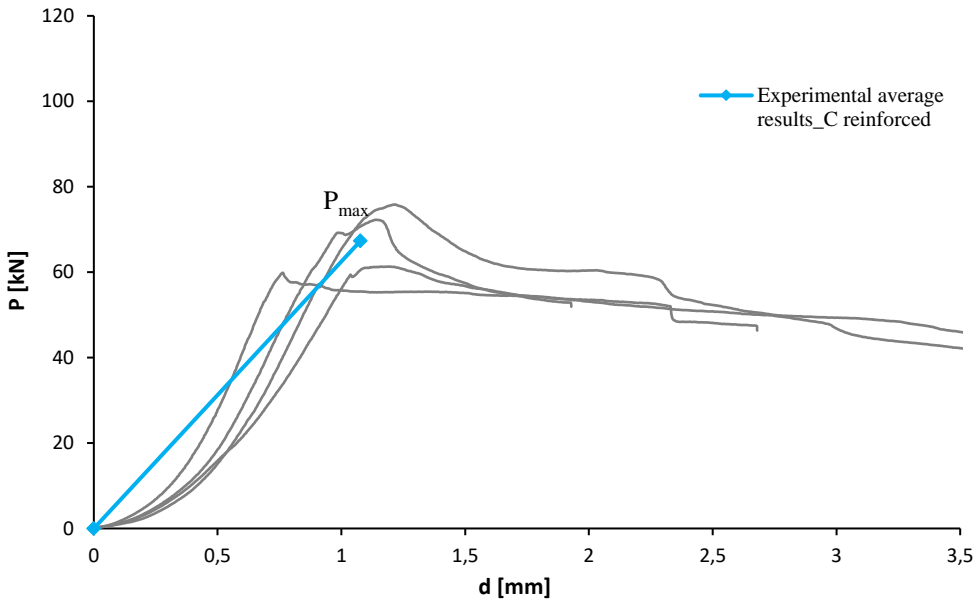


Figure 5.9 Load-displacement curve, specimens group C\_reinforced ( $t_{r3}=1800s$ )

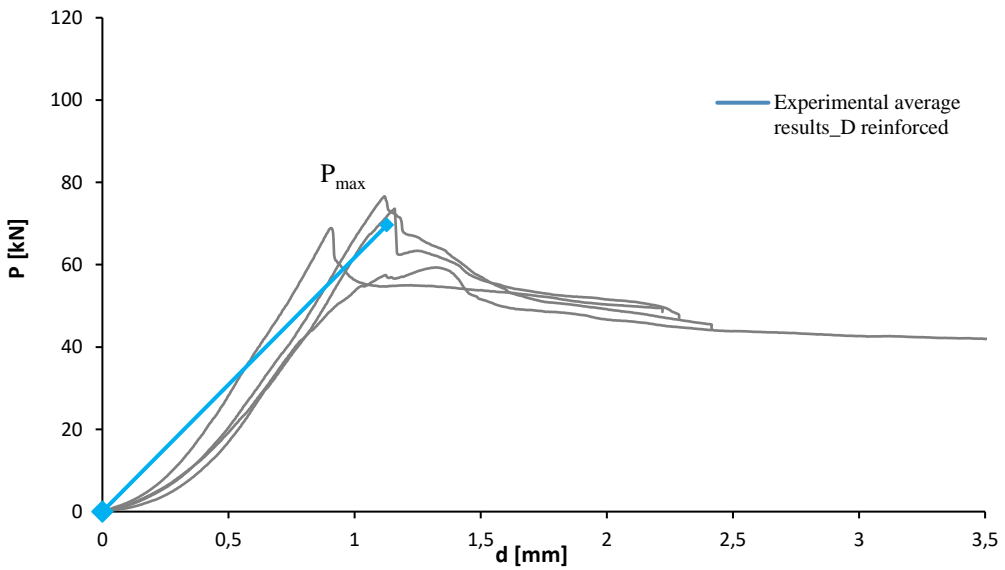


Figure 5.10 Load-displacement curve, specimens group D\_reinforced ( $t_{r4}=3600s$ )

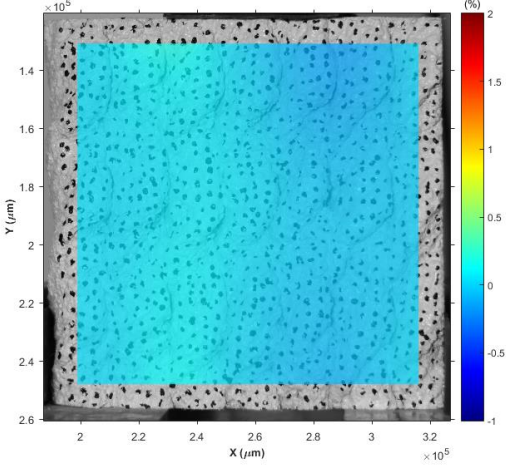
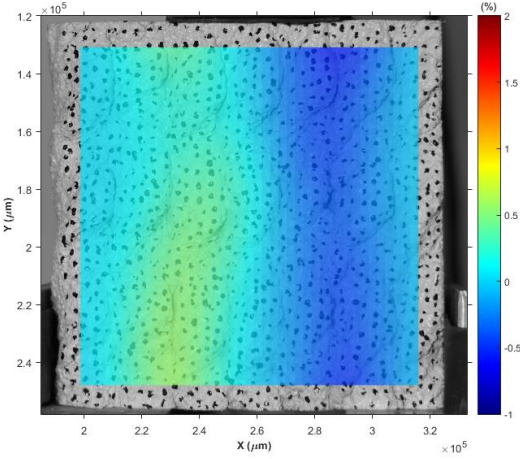
From the analysis of the results, the trend of the curves is about the same for every sample, characterized mainly by an increase in load until its maximum value,  $P_{max}$ , which represents the complete propagation of the shear failure, and then by a post-peak phase of residual strength, showing a clear ductile behavior.

In tabular form, the values of maximum loads and the corresponding displacements are reported (see Table 5.3).

ID	Label	$P_{max}$ (kN)	$d(P_{max})$ (mm)
A	A1_r	85,12	0,40
	A2_r	90,02	0,93
	A3_r	88,54	0,99
	A4_r	94,99	1,12
<b>mean value</b>		<b>89,67±4,09</b>	<b>0,86±0,31</b>
B	B1_r	88,75	1,35
	B2_r	75,28	1,02
	B3_r	72,23	1,29
	B4_r	79,61	2,30
<b>mean value</b>		<b>78,96±7,19</b>	<b>1,49±0,56</b>
C	C1_r	75,82	1,21
	C2_r	72,26	1,14
	C3_r	59,82	0,76
	C4_r	61,31	1,18
<b>mean value</b>		<b>67,31±7,93</b>	<b>1,07±0,21</b>
D	D1_r	59,32	1,32
	D2_r	76,61	1,12
	D3_r	68,87	0,91
	D4_r	73,59	1,16
<b>mean value</b>		<b>69,60±7,55</b>	<b>1,12±0,17</b>

Table 5.3. Experimental results for printed reinforced specimens

All the samples have exhibited a flexural cracks onset at the middle of the lower surface before the shear cracks arose and propagated, due obviously to the presence of rods. This implies that the rods also lead toward a different resistance mechanism, confirmed by the following pictures in Table 5.5 in which the breaking behavior of a random specimen of each group is presented. The results are confirmed by the transversal strain distribution at the failure of a random reinforced specimen (see Table 5.4)

ID	Failure step distribution
A <sub>1r</sub>	<p data-bbox="302 458 485 554"><math>\gamma_{xy}</math> distribution at complete failure</p> 
B <sub>1r</sub>	<p data-bbox="302 1043 485 1138"><math>\gamma_{xy}</math> distribution at complete failure</p> 

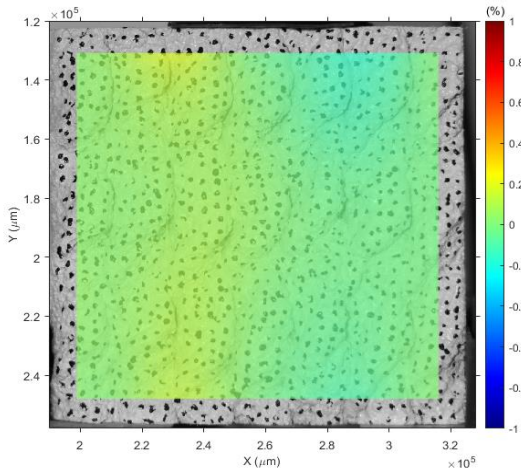
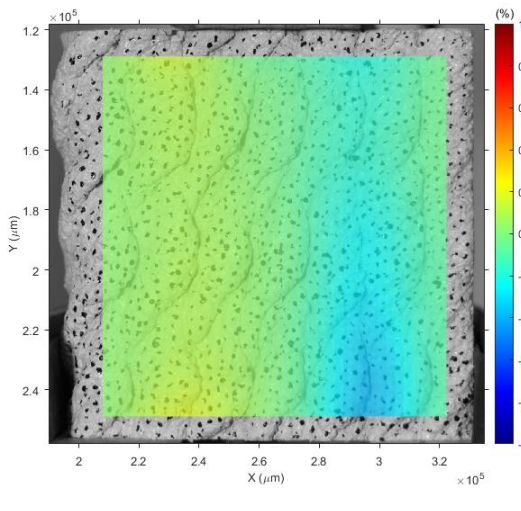

C <sub>1r</sub>	$\gamma_{xy}$ distribution at complete failure	
D <sub>1r</sub>	$\gamma_{xy}$ distribution at complete failure	

Table 5.4. The transversal strain distribution at the failure for a specimen (as an example) belonging to each group

ID	Failure picture
A <sub>1r</sub>	



$B_{1r}$



C<sub>1r</sub>

$D_{lr}$



Table 5.5 The images representing the failure for a specimen (as an example) belonging to each group



## 5.2 Numerical test and results

In this section, the simulation and the relative results of the reinforced layered elements' behavior is implemented and presented. The Finite Elements method is based on the same interaction model and critical energy value (the parameters adopted are summarized in the Table 5.6 obtained for the un-reinforced specimens.

$K_{nn}$ (MPa/mm)	$K_{tt}$ (MPa/mm)	$K_{ss}$ (MPa/mm)	$t_n$ (MPa)	$t_t$ (MPa)	$t_s$ (MPa)	$G_{IIC}$ (J/mm <sup>2</sup> )
172 750	66 500	66 500	7.19	7.19	7.19	1.7

Table 5.6. Parameters of the traction-separation law

This simulation features indeed the same same geometry, material model (CDP model), boundary conditions, loading and layers interaction model, i.e. surface based cohesive model, with respect un-reinforced element's modelling.

The only difference among the two models is the reinforcement which has been modelled through six rebars-like elements placed where the original reinforcement rods were located in the tested reinforced specimens (the location of the rebars-like elements is shown in Figure 5.6. The rebars' material have been assumed as linear elastic, therefore the only parameters needed to fully characterise the material were the Young' modulus, the Poisson's coefficient and the shear modulus, reported in the following table.

$E$ (MPa)	$\nu$	$G$ (MPa)
210 000	0.3	80 769.2

Table 5.7. Parameters for rebars material characterization

Three principal steps are taken into account: 1<sup>st</sup> step, 16<sup>th</sup> step and step 38<sup>th</sup> which refer to the first step, the step at which the fractures begin and the step corresponding to the complete failure.

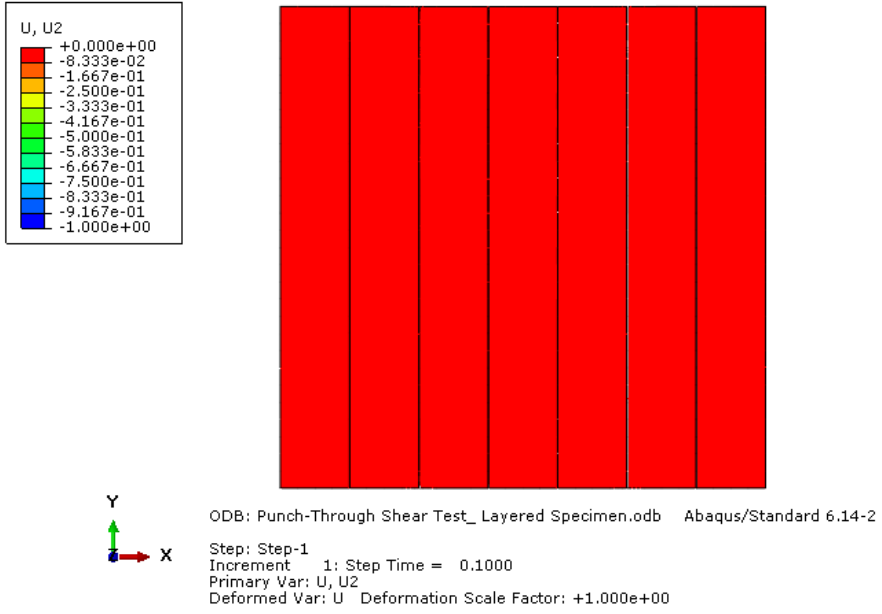


Figure 5.11 Vertical displacement distribution 1<sup>st</sup> Step

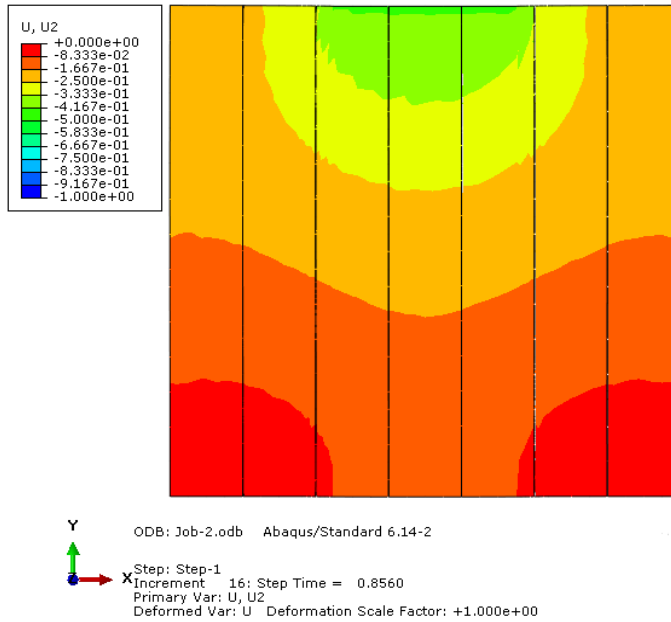


Figure 5.12 Vertical displacement distribution 16<sup>th</sup> Step

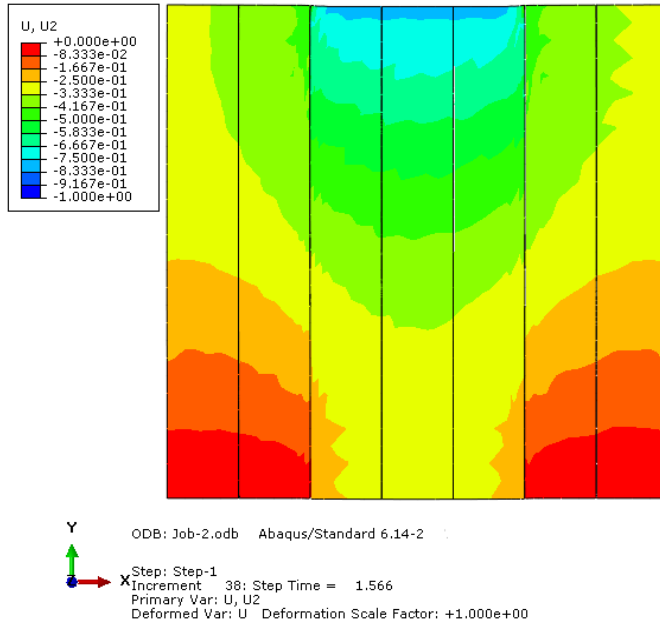


Figure 5.13 Vertical displacement distribution 38<sup>th</sup> Step

The principal outcome of the simulation is the load vs displacement plot which is the reference curve for both the experimental and the numerical test. Since the simulation is performed in displacement control the load is computed as sum of the vertical reaction at each node of the bottom supports whilst the vertical displacement is evaluated at the central node of the upper surface.

In Figure 5.14 the load vs displacement is reported, on which the points corresponding to the the maximum load are marked. The values of the crack propagation load are reported in Table 5.8.

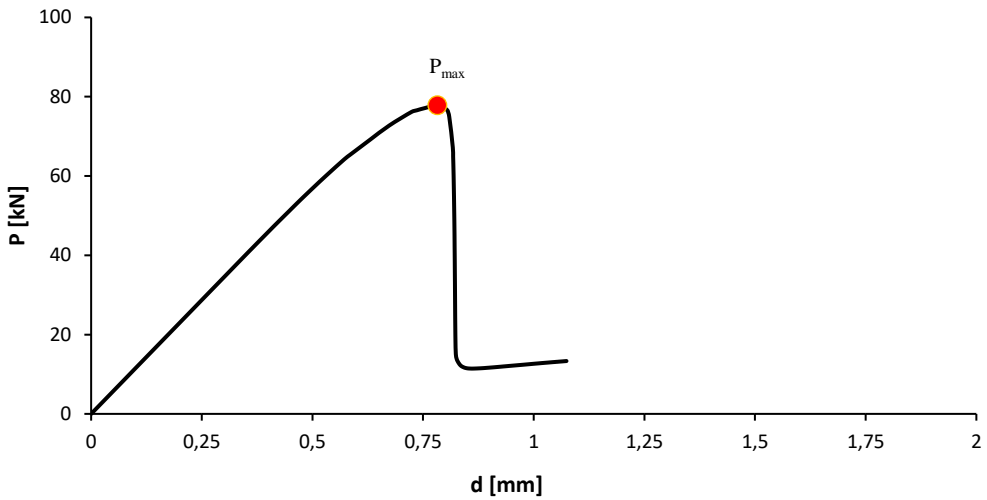


Figure 5.14 Load vs Displacement curve, reinforced layered specimen simulation

$P_c$	$d(P_c)$	$P_{max}$	$d(P_{max})$
(kN)	(mm)	(kN)	(mm)
-	-	79.5	0.78

Table 5.8. Crack initiation load and maximum load

### 5.3 Summary

This chapter has been focused on the modelling of the interlaminar reinforcement system, giving both the experimental and numerical results. In this section, finally, a discussion and comparison between the results is presented. Firstly, also in the case of reinforced specimens the different results are comparable, demonstrating the correspondence between the real behavior and the mechanical properties. This match is displayed in the following figures, presenting the trend of the average experimental -acquired in terms of average values of stiffness- and numerical curves in the case of each group of specimens, characterized by the waiting time of 100s, 200s, 1800s and 3600s.

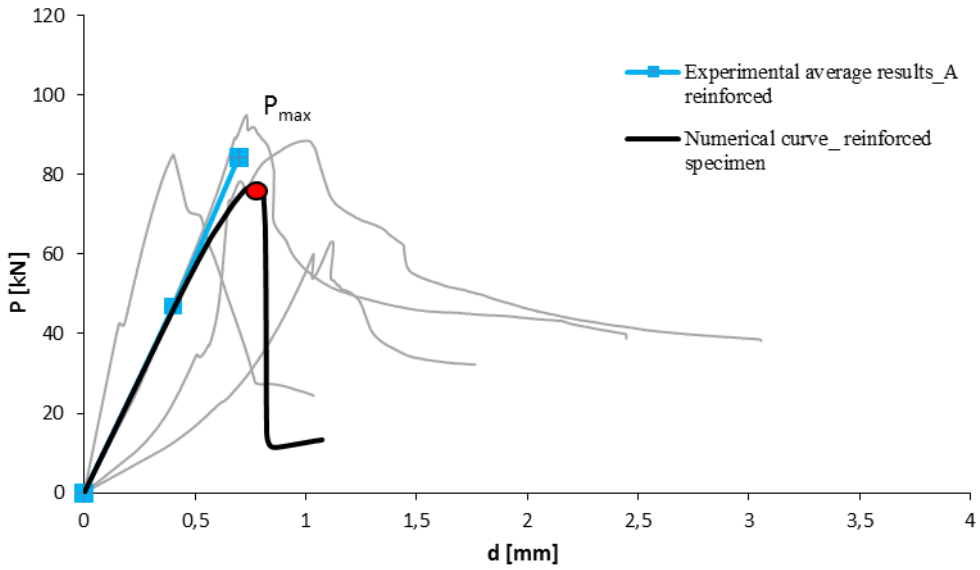


Figure 5.15 Experimental and numerical curve, specimen group A\_reinforced

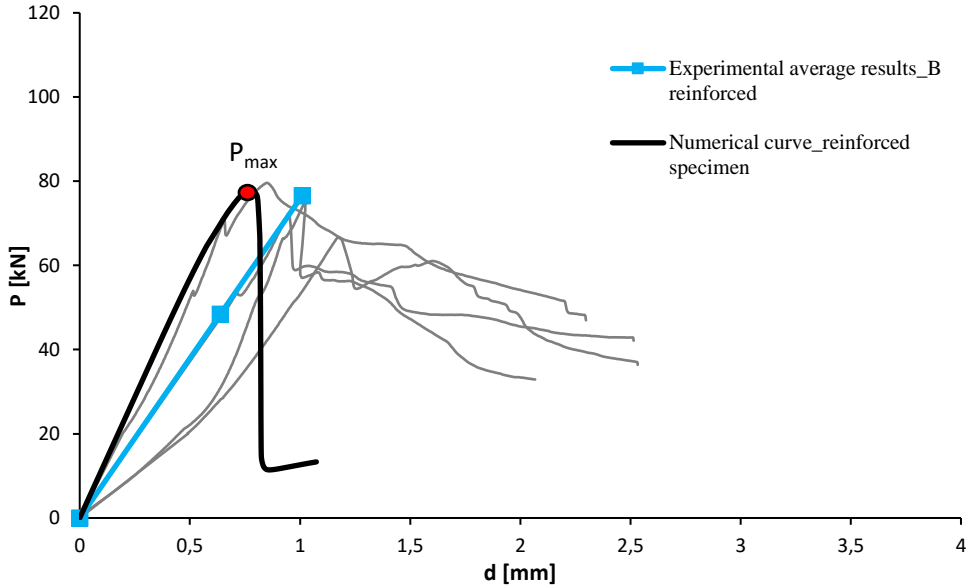


Figure 5.16 Experimental and numerical curve, specimen group A\_reinforced

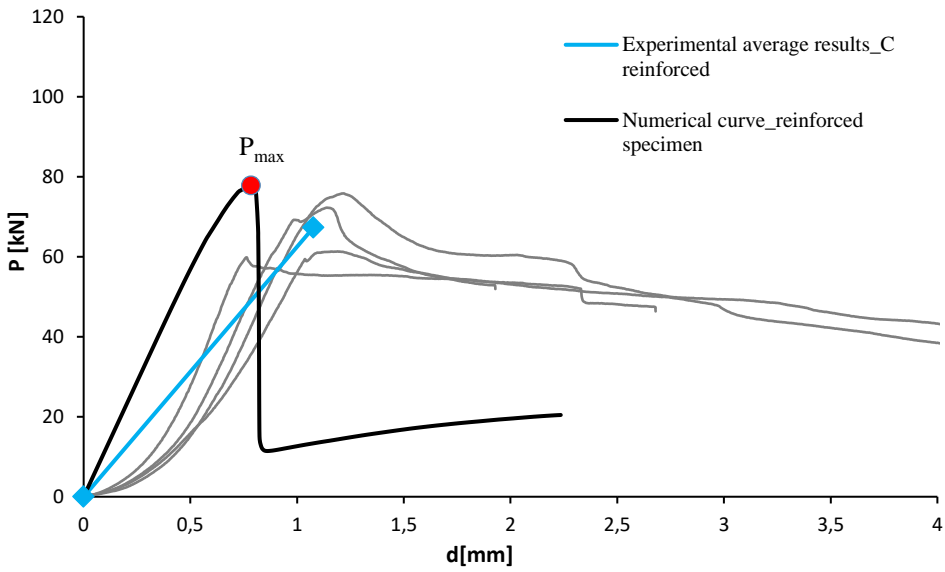


Figure 5.17 Experimental and numerical curve, specimen group C\_ reinforced

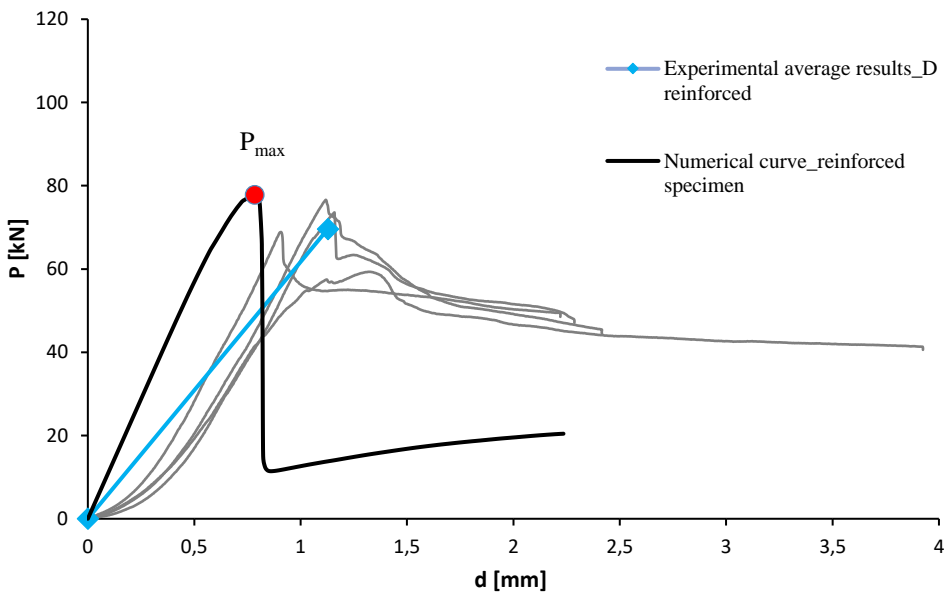


Figure 5.18 Experimental and numerical curve, specimen group D\_ reinforced

From an initial mere visual analysis of data, the outcomes of the experimental test seem well approximate the numerical simulation of the elements, with regards to maximum load, as also the \* Subscript "ave" indicate average values.

Table 5.9 confirms.

ID	Mean Experimental Results		Numerical Simulation	
	$P_{\max, \text{ave}}^*$ (kN)	$dP_{\max, \text{ave}}^*$ (mm)	$P_{\max}$ (kN)	$dP_{\max}$ (mm)
Series A	89,67	0,86	77,81	0,78
Series B	78,97	1,49		
Series C	67,30	1,07		
Series D	69,60	1,12		

\* Subscript "ave" indicate average values.

Table 5.9. Critical and Maximum Load average values comparison

Specifically, the difference between experimental and numerical results is in the order of 2% in terms of maximum loads for elements with multiple layers with steel rods embedded.

Another important data concerns the higher strength in terms of maximum load value exhibited by the printed reinforced elements with respect to the printed unreinforced elements, showing the influence and the benefits of the rods in the 3D concrete structure on the mechanical performances. In fact, the rods provide an increase in shear strength due to a sort of dowel action like in the common reinforced concrete elements, as the graph in Figure 5.19 shows.

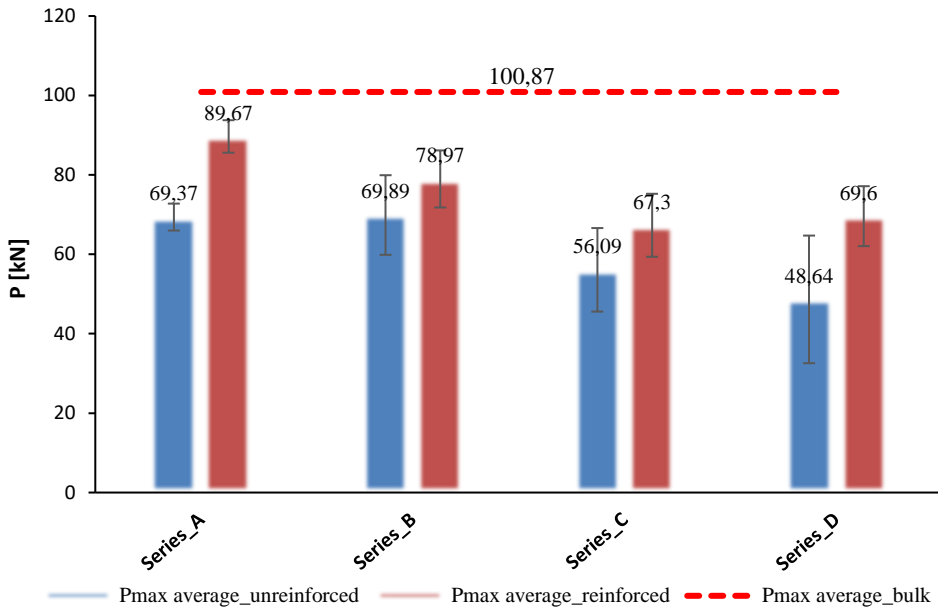


Figure 5.19 Comparison between average values of  $P_{\max}$  for unreinforced, reinforced and bulk material specimens

Furthermore, both unreinforced and reinforced elements cases present the lower shear strength than elements characterized by bulk material, confirming that the layers interfaces are weakness zones. In particular, the experimental results about the plain concrete elements show that the maximum load is about 45% higher than the maximum load of layered non reinforced elements, but about 20% bigger that deriving from reinforced elements.



## References

- Asprone D., Menna C., Bos F., Salet T., Mata-Falcon J., Kaufmann W., 2018 “Rethinking reinforcement for digital fabrication with concrete”, *Cem. Concr. Res.* 112 (C) 111–121.
- Mccormick, N., and Lord J.. 2010. “Digital Image Correlation.” *NUMBER*. Vol. 13.
- Sanjayan, J. G., Nematollahi B., Xia M, and Marchment T.. 2018. “Effect of Surface Moisture on Inter-Layer Strength of 3D Printed Concrete.” *Construction and Building Materials* 172 (May): 468–75. <https://doi.org/10.1016/j.CONBUILDMAT.2018.03.232>.
- Zareiyan, B., and Khoshnevis B.. 2017. “Effects of Interlocking on Interlayer Adhesion and Strength of Structures in 3D Printing of Concrete.” *Automation in Construction* 83 (August): 212–21. <https://doi.org/10.1016/j.autcon.2017.08.019>.



# Chapter 6

## **DYNAMIC CHARACTERIZATION OF 3D PRINTED CONCRETE ELEMENTS' INTERFACES**

From the experimental and numerical results displayed in the previous chapters on the elements characterized by casting material and on the printed elements, the weakness at the interface between different layers is demonstrated. Since these contact zones could potentially compromise the structural stability and also the durability of printed elements (Nematollahi et al., 2017), their behavior under high dynamic loads is fundamental to investigate the vulnerability of such elements under extreme dynamic events.

So far, no dedicated approaches were reported on the bond of interface between 3D printed layers to examine its dynamic characteristics, at different strain-rate levels, with respect to static conditions. Thus, this chapter investigates the aspects just presented with a focused view on future developments about the feasibility and the implementation of digital construction. Dynamic characterization was performed through high strain-rate failure tensile and shear tests.

The results revealed that elements produced through 3D-printing technique, when subjected to dynamic loads present a less performing shear and tensile behaviour as the waiting time increases, confirming the interface between layers as surface of weakness.

## **6.1 Experimental program**

The experimental campaign on printed elements has been implemented. Different sample manufacturing techniques have been used; specifically both the traditional and static casting process, where concrete material is poured into formwork and then allowed to solidify, and the novel extrusion-based 3D printing application, where the material is deposited layer-upon-layer without using mould. The single properties of specific material composition, printing machine and preparation of the specimen are described in the following sections.

### **6.1.1. *Material composition***

3DCP mix design choice is the most important issue for defining concrete as a material able to reach the feasibility of 3D printing method. Specifically, the material must be designed to fulfil certain target rheological properties for describing its fresh-state structural build-up and performance requirements for hardened state. The rheological properties of the cementitious material is a focal aspect for digital applications, as the potential success or failure of the element execution, and so the quality of interfaces and its strength, depend on controlling these parameters (Wangler et al., 2016; Marchon et al., 2018). The control and optimization rheology allows to make the material able to be pumped and simultaneously to sustain the weight of subsequent layer deposition with little or no deformation after extrusion, in other words to satisfy the extrudability and buildability properties (Buswell et al., 2018; Perrot et al., 2016). The adopted material, more like cement-based mortar, guarantees an optimal rheological balance.

The characteristics of the material is the same described in §3.2.1 and are briefly illustrated below. It is characterized by a low water/cement ratio of 0.38, in order to increase the buildability of the material. Cement CEM II/A-LL 42, 5 R and a 4mm maximum size aggregates because of the small nozzle diameter were used. The mixture contains also of polypropylene short fibres of 0.1% by weight, to prevent plastic shrinkage cracking in early stage of curing and after the deposition stage. A polycarboxylate based superplasticizer was added to the mixture for improving its workability, and a filler with maximum particles size lower that 0.067 mm was mixed aimed to fill the voids and reduce the overall porosity accordingly (Asprone et al., 2018).

### 6.1.2. Specimens preparation

The specimens, like those produced previously, were realized using a WASP printer by Italian CSP Company. The printer, of which a clear plan ad description is reported in §2.3.1, consists of 3 braces sliding along many pillars and controlling the printing head, made of a conical hopper in which the fresh concrete is pumped and extruded toward circular nozzle. A numerical controller defines exactly the printing head localization within the triangular printing work area. The mixture was extruded through the nozzle by moving the extruder with a constant speed of 40 mm/s.

To analyse the behaviour of the printed elements, the specimens were subjected to static and dynamic loading conditions. Specifically, three batches of three layered prismatic specimens were prepared with length and height of 60 mm and thickness of 40 mm, as the Figure 6.1 shows. Each batch is characterized by the same material specifications above-described and by different time intervals  $T_s$  between depositions of two subsequent layers ( $T_s=0\text{min}$ ,  $T_s=10\text{min}$ ,  $T_s=30\text{min}$ ). These specimen groups were compared with another reference group, defined as bulk hereafter, made of casting material and tested in both static and dynamic conditions. The total number of specimens used for shear characterization was of 24 specimens.

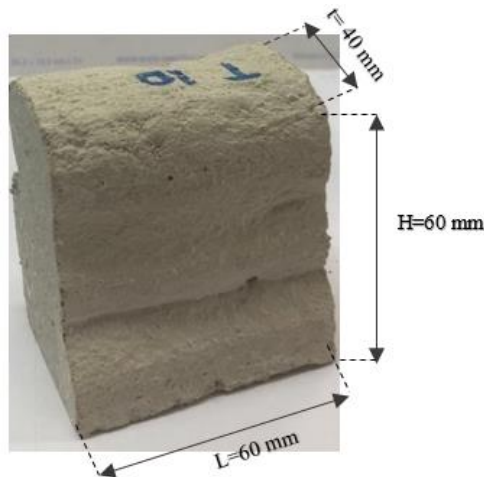


Figure 6.1. Size prismatic specimen

A further campaign was adopted in order to investigate the direct tensile

strength, in both static and dynamic configuration. For defining dynamic tensile behaviour, two tests at medium and high strain-rates were carried out on cylindrical specimens made of two layers with thickness of 10 mm and diameter of 20 mm.

The Figure 6.2 shows the size of specimens, where the thickness of the different layers is highlighted by the relative colors, created through the use of special pigments. This artifice has also been practiced to make the failure surface more evident after the tensile tests.

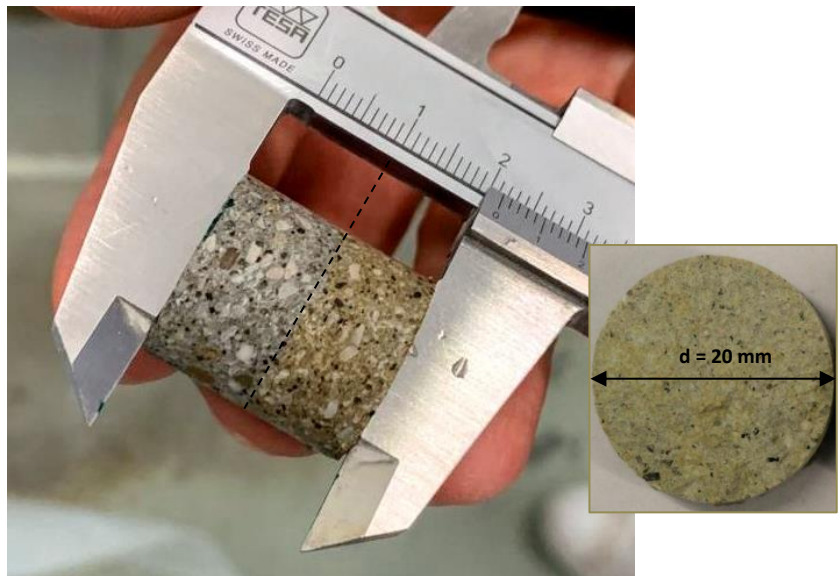


Figure 6.2. Size cylindrical specimen

The Table 6.1 shows clearly the labels given to each tested sample.

Loading condition		Bulk	T <sub>0</sub>	T <sub>10</sub>	T <sub>30</sub>
Static	Shear test	3L_001	3L_T <sub>0</sub> _001	3L_T <sub>10</sub> _001	3L_T <sub>30</sub> _001
		3L_002	3L_T <sub>0</sub> _002	3L_T <sub>10</sub> _002	3L_T <sub>30</sub> _002
		3L_003	3L_T <sub>0</sub> _003	3L_T <sub>10</sub> _003	3L_T <sub>30</sub> _003
	Direct tensile test	2L_001	2L_T <sub>0</sub> _001	2L_T <sub>10</sub> _001	2L_T <sub>30</sub> _001
		2L_002	2L_T <sub>0</sub> _002	2L_T <sub>10</sub> _002	2L_T <sub>30</sub> _002
		2L_003	2L_T <sub>0</sub> _003	2L_T <sub>10</sub> _003	2L_T <sub>30</sub> _003
Dynamic	Shear test	3L_004	3L_T <sub>0</sub> _004	3L_T <sub>10</sub> _004	3L_T <sub>30</sub> _004
		3L_005	3L_T <sub>0</sub> _005	3L_T <sub>10</sub> _005	3L_T <sub>30</sub> _005
		3L_006	3L_T <sub>0</sub> _006	3L_T <sub>10</sub> _006	3L_T <sub>30</sub> _006
	Direct tensile test medium strain-rate ( $\dot{\epsilon} = 50 \text{ s}^{-1}$ )	2L_001m	2L_T <sub>0</sub> _004m	2L_T <sub>10</sub> _004m	2L_T <sub>30</sub> _004m
		2L_002m	2L_T <sub>0</sub> _005m	2L_T <sub>10</sub> _005m	2L_T <sub>30</sub> _005m
		2L_003m	2L_T <sub>0</sub> _006m	2L_T <sub>10</sub> _006m	2L_T <sub>30</sub> _006m
	Direct tensile test high strain-rate ( $\dot{\epsilon} = 200 \text{ s}^{-1}$ )	2L_001h	2L_T <sub>0</sub> _004h	2L_T <sub>10</sub> _004h	2L_T <sub>30</sub> _004h
		2L_002h	2L_T <sub>0</sub> _005h	2L_T <sub>10</sub> _005h	2L_T <sub>30</sub> _005h
		2L_003h	2L_T <sub>0</sub> _006h	2L_T <sub>10</sub> _006h	2L_T <sub>30</sub> _006h

Table 6.1. Specimen labels

## 6.2 Experimental set-up

The entire experimental campaign, in both static and dynamic loading conditions, was conducted at the DynaMat Laboratory of the University of Applied Sciences and Arts of Southern Switzerland (SUPSI) of Lugano.

### 6.2.1. *Direct tensile setup*

Tensile failure tests were performed in according to European Standard EN1015-11 using a universal servo-controlled machine with a constant strain-rate of  $10^{-5}$ . Ordinary conditions, in terms of humidity and temperature, were adopted for conducting the tests. Quasi-static tests were performed by means of a universal electro-mechanical testing machine type Zwick/Roell-Z50 (maximum load capacity of 50 kN). A bi-component epoxy resin was used to glue the specimens to the supports. The required hardening time at room temperature is at least 8 hours.



Figure 6.3. Direct static tensile test setup

The main aim of tests under static conditions was to have reference data for the dynamic characterization. For investigating dynamic tensile behaviour, two different experimental setups were implemented. For medium strain-rate tests a Hydro-Pneumatic Machine (HPM) was used.



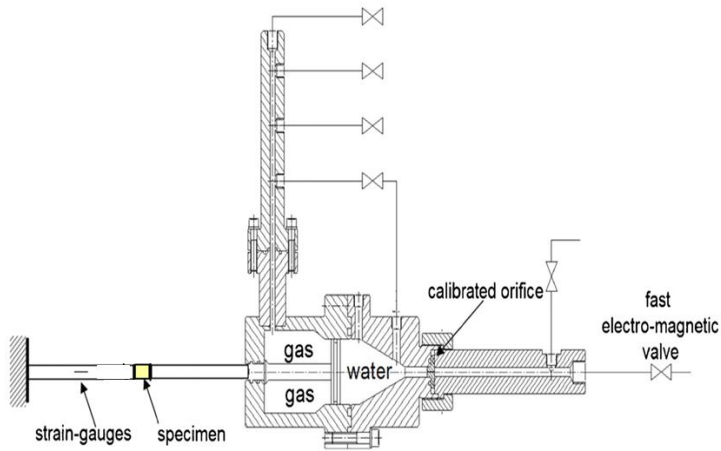


Figure 6.4. Hydro-Pneumatic Machine scheme

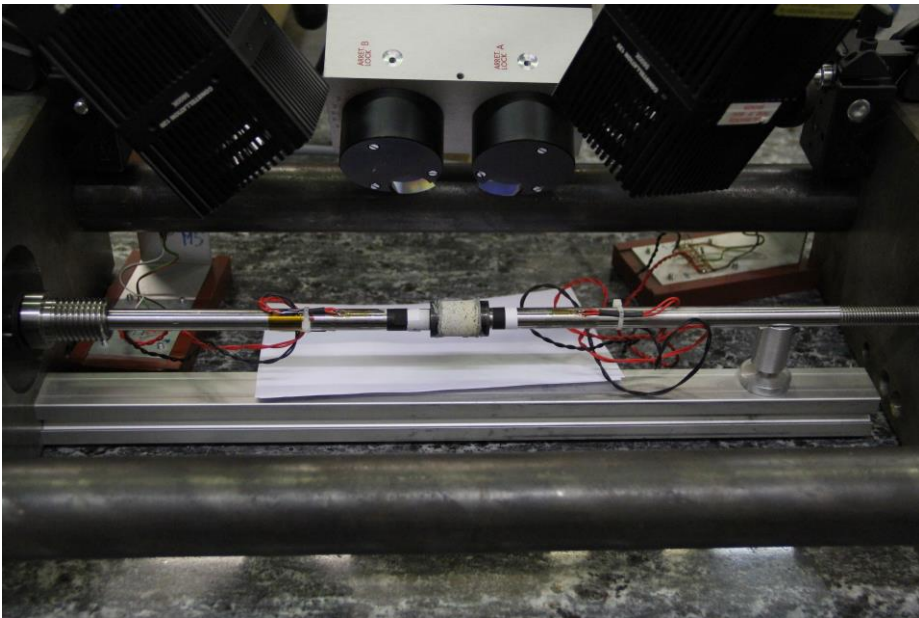


Figure 6.5. Hydro-Pneumatic Machine for medium strain-rate tests

The HPM is made of a cylindrical tank divided by a sealed piston in two chambers, filled with gas at high pressure (e.g. 150 bars) and water. The test starts when the equilibrium between two chambers is changed, i.e. the second chamber

discharges the water through a calibrated orifice, activated by a fast electromagnetic valve. Then, the piston starts moving expelling out the gas through a sealed opening, whose end is connected to the specimen; the specimen is linked to the other extremity to an elastic bar, rigidly fixed to the structure supporting the machine. When the piston shaft moves, the specimen is pulled at a fixed strain-rate level, depending on the velocity of the gas expelled from the chamber and so on the orifice size. The crack opening displacement was directly measured following the motion of two black and white edges painted on the bar ends, closer to the specimen (see Figure 6.5).

An electro-optical extensometer 200XR with a measuring range of 5mm (maximum resolution of  $5 \cdot 10^{-4}$  mm) and equipped by a gauge length adapter (1-25mm) was used. More details on the functioning of HPM can be found in different works (Cadoni et al, 2011; Cadoni 2010; Coppola et al., 2018).

Whereas a Modified Hopkinson tensile Bar (MHB) apparatus was used to conduct high train-rate tests.

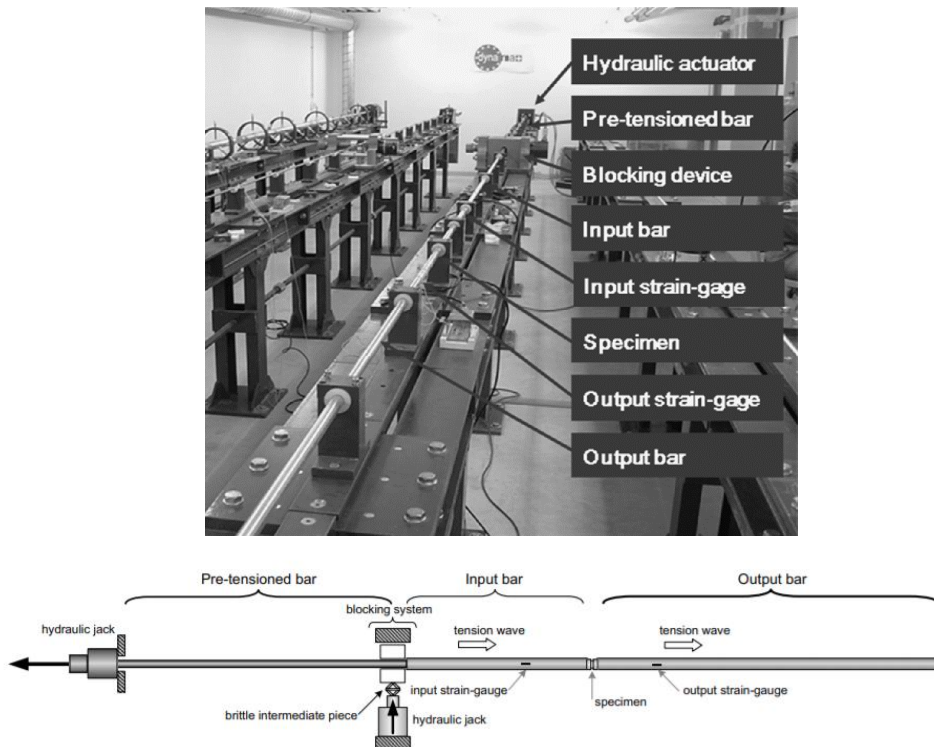


Figure 6.6. Modified Hopkinson Tensile Bar apparatus (Cadoni et al, 2011)



Figure 6.7. Specimen place in Modified Hopkinson Tensile Bar

The machine consists of two longitudinally aligned aluminum bars 20mm in diameter, the namely input bar and output bar, characterized by front and end surface contact, between which the specimen -with the same diameter as the input and output bar- is located, using a bi-component epoxy resin. The input and output bars were instrumented with strain gauges that measure the incident, reflected and transmitted pulses acting on the cross section of the specimen. The pre-tensioned bar was a high strength steel directly connected to the input bar.

The functioning scheme consists in: firstly a hydraulic actuator pulls end of the pre-tensioned bar, which is jammed on the other end by the blocking device. The pulse propagates along the input bar. When the incident pulse ( $\epsilon_I$ ) reaches the specimen, one part ( $\epsilon_R$ ) is reflected by the specimen and another part ( $\epsilon_T$ ) passes through the specimen propagating into the output bar. The amplitudes of the incident, reflected and transmitted pulses depend on the mechanical properties of the specimen. Strain-gauges placed on the input and output bars are useful for the measurement of the elastic deformation created on both halfbars, respectively, by the incident/ reflected and transmitted pulses (Cadoni 2010; Cadoni and Forni, 2015).

Starting from the acquired signals, the stress and strain history and so the strain-rate curves can be calculated, in order to describe the behaviour of the investigated concrete elements under extreme loading conditions.

### 6.2.1. *Shear tests setup*

The preliminary static shear response of printed elements was analysed considering as reference study the Punch-through shear test available in literature and proposed by J. Davies (Davies 1987), although some changes on the original set-up were produced, related to the printing process. The test imposes a sliding fracture along two identified surfaces and is based on plain concrete material with a shape ratio equal to 1 over 1, in order to make shear failure the superimposed mode of fracture.

In this work, the test was performed in the direction of parallel to the printed layers, since the main goal is the analysis of the shear behaviour, as the following figures exhibit.

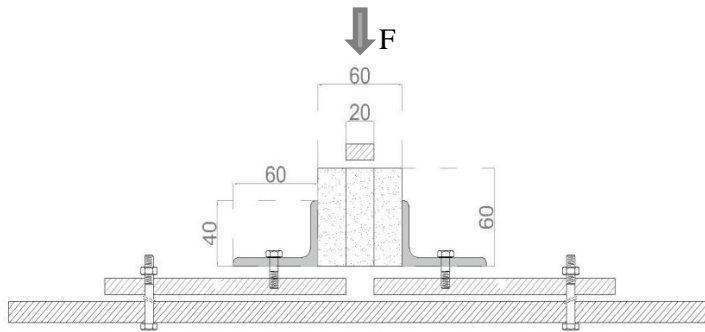


Figure 6.8. The design of Punch-through shear test setup

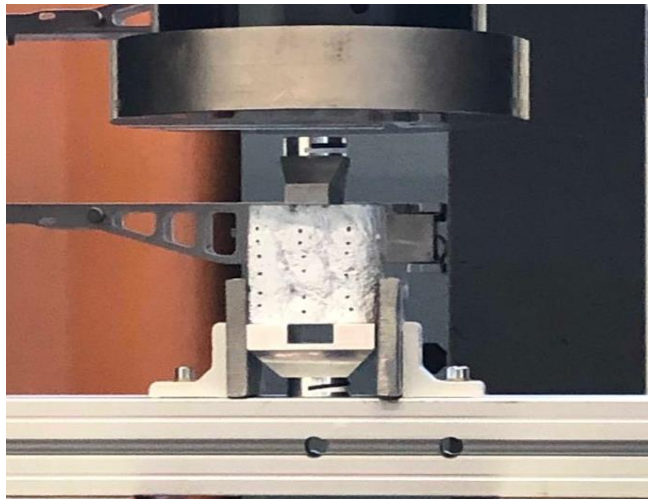


Figure 6.9. The design of Punch-through shear test setup

The samples made of layers were arranged in a way that the central layer is under the upper loading plate whereas the two external layers, on both sides of the sample, are in contact with the bottom supports. Besides, in order to ensure a fine contact between the irregular surfaces of printed elements and the lateral supports rubber sheets were used. Quasi-static tests were performed by means of a universal electro-mechanical testing machine type LFM 600, characterized by a maximum load capacity of 600 kN.

A Modified Hopkinson compression Bar (MHcB) apparatus, showed in Figure 6.10, was employed for testing the dynamic behaviour of the printed elements (Cadoni et al., 2006; Albertini et al., 1998). Unlike the standard Hopkinson bar characterized by a diameter in the range 10-20 mm, this machine is made of two aluminium bars 30 mm in diameter namely input and output bars, 3 meters long, with front and end surface contact, between which the specimen is located. The reason why the diameter of the standard bar is smaller lies in the fact that it is used for dynamic testing of ductile metals, while larger diameter bars are needed to load representative volumes of concrete which is quasi-brittle material.

The technique consists of applying a pressure stress wave by a pre-tension of a high-strength steel bar 6 m long, which is the physical continuation of the input bar and having a precise diameter of 12 mm (Lindhholm, 1971). During the experiment, the free end of the pre-tensioned bar is pulled by means of a hydraulic actuator, while the end connected to the input bar is fixed by a blocking device. The details of the working principle are reported here (Cadoni et al., 2009; Fenu et al., 2018).

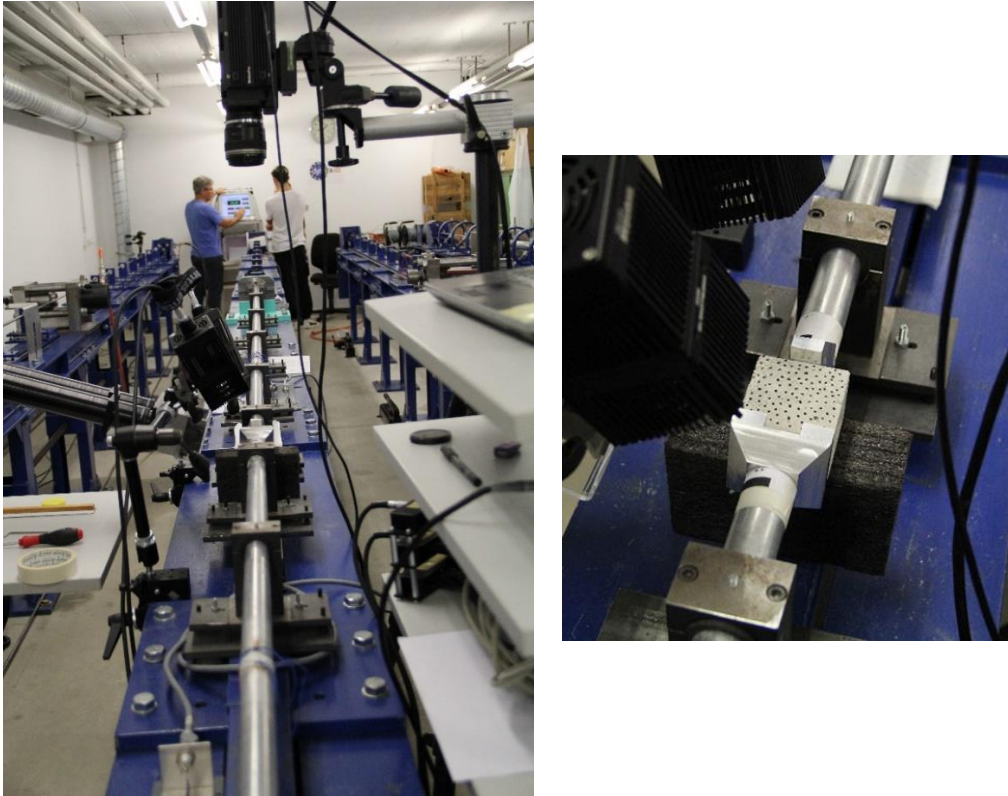


Figure 6.10. left: Modified Hopkinson compression Bar; right: shear testing specimen

The elastic energy is stored in the pre-tensioned bar by pulling its extremity and released to the input bar, leading the propagation of a compressive wave which generates the specimen's brittle failure. The records are taken by the strain-gauge stations glued on the input and output bars of the elastic deformation. The application of the elastic one-dimensional stress wave propagation theory (Lindholm 1971) to the split Hopkinson bar system allows to assess the forces  $F_1$  and  $F_2$  and the displacements  $\delta_1$  and  $\delta_2$  acting on the two faces of the specimen in contact with the input and output bars.

$$F_1 = E_0 \cdot A_0 \cdot (\epsilon_I + \epsilon_R) \quad (45)$$

$$F_2 = E_0 \cdot A_0 \cdot (\epsilon_T) \quad (46)$$

$$\delta_1 = C_0 \int (\epsilon_I - \epsilon_R) dt \quad (47)$$

$$\delta_2 = C_0 \int \epsilon_T dt \quad (48)$$

where  $E_0$  is the bar elastic modulus,  $A_0$  is the bar cross-section area,  $C_0$  is the elastic wave velocity (assumed as 5064 m/s), while  $\epsilon_I$ ,  $\epsilon_R$  and  $\epsilon_T$  are the incident, reflected and transmitted pulses, respectively.

From the measurement of the reflected and transmitted pulse, the strain rate in the specimen is obtaining as follows:

$$\dot{\epsilon}(t) = -\frac{2 C_0}{L} \epsilon_R(t) \quad (49)$$

The shear behaviour was described thanks to the design and consequent use of specific supports (Figure 6.11 and Figure 6.12) capable of inducing shear failure.

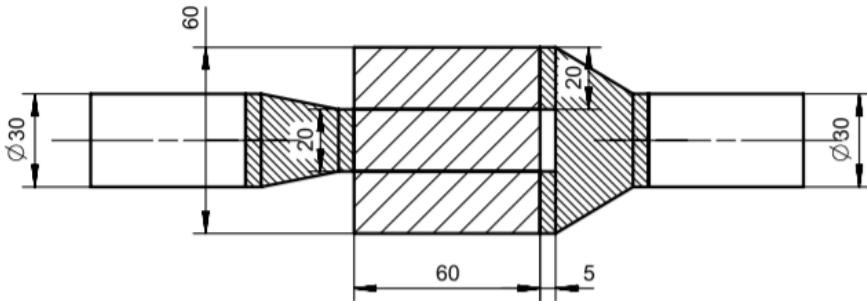


Figure 6.11 Shear supports design

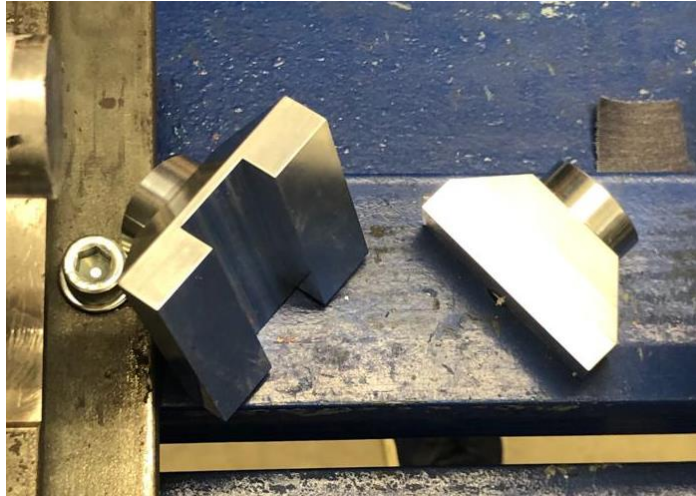


Figure 6.12. Shear supports production

## 6.3 Experimental Results

In the previous section a detailed setup analysis for the different tests carried out has been reported. The results of the tests conducted on different type of specimen are presented and then discussed below.

### 6.3.1. *Tensile tests results*

Tensile experimental data processing can be used to investigate the behavior of the plain and printed concrete subjected to a dynamic regime, at different strain rates. The strain rate during the test is not a constant value, but varies with time so its definition becomes complicated (see Eq. (49)). In order to take into account the test input, imposed strain-rates, equal to the ratio between strain velocity and initial specimen length, are calculated:

$$\dot{\epsilon} = \frac{v_s}{L_0} \quad (50)$$



$v_s$	$L_0$	$\dot{\epsilon}$
(m/s)	(m)	(s <sup>-1</sup> )
0,000002		10 <sup>-5</sup>
1	0.02	50
4,316		215

Table 6.2. Imposed strain-rates in the tests

These results have been compared with the static performances, reported in terms of numerical values in Table 6.3 and in Figure 6.13 and Figure 6.14 in only two cases, i.e. a random specimens characterized by bulk material and printed material with higher waiting time, respectively.

Furthermore, as the Figure 6.13 demonstrates, in the static tensile loading condition, a notch into the bulk specimen, in correspondence with the layer surface, has been produced, in order to induce the tensile crack in the middle of the surface.

A first finding with regards to the printed specimens can be deduced just from the images reported in Figure 6.15, Figure 6.16 and Figure 6.17, Figure 6.18, where a specimen before and after the dynamic tensile test, for performed printing time, is showed revealing a more clear-cut interface failure in the case of higher waiting time ( $T_s=10\text{min}$ ) and so a weaker interface behavior with increasing printing time.



Figure 6.13. Specimen with bulk material before and after static tensile test



Figure 6.14. Printed specimen with  $T_s = 30\text{min}$  before and after static tensile test



Figure 6.15. Specimen with  $T_s=0\text{min}$  before a high strain rate tensile failure test

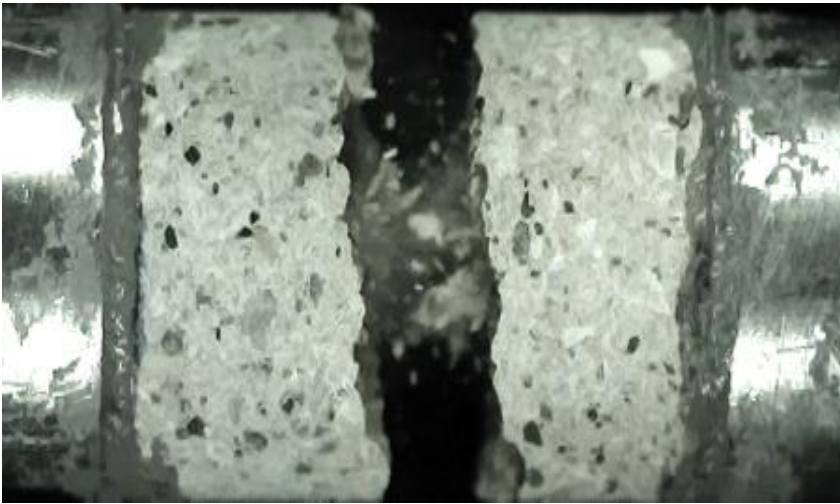


Figure 6.16. Specimen with  $T_s=0\text{min}$  after a high strain rate tensile failure test



Figure 6.17. Specimen with  $T_s=10$  min before a high strain rate tensile failure test



Figure 6.18. Specimen with  $T_s=10$  min after a high strain rate tensile failure test

The results are presented in Table 6.3, and in Figure 6.19 are shown in terms of failure time ( $T_f$ ) versus strain velocity ( $v_s$ ) for each resting time.

Loading conditions	Resting time (min)	$F_{\max, ave}^*$ (N)	$\sigma_{ave}^*$ (MPa)	$\sigma_{st.dev}^*$ (MPa)	Static series variance (%)	Fracture time ( $T_f$ ) (s)
Static	Bulk	566,26	3,15	1,18	-	29,10
	0	415,05	1,34	0,3	-	15
	10	143,77	0,46	0,3	-	10,4
	30	363,74	1,03	0,23	-	21,54
$\dot{\epsilon} = 50 \text{ s}^{-1}$	Bulk	992,21	3,16	0,48	0%	8,51E-03
	0	1292,97	4,19	1,3	68%	5,10E-03
	10	491,05	1,59	1,05	71%	2,20E-03
	30	510,40	1,65	0,05	38%	6,77E-03
$\dot{\epsilon} = 200 \text{ s}^{-1}$	Bulk	2561,78	8,31	0,23	62%	3,64E-05
	0	2393,2	7,76	1,39	83%	3,90E-05
	10	1958,89	6,3	1,27	93%	3,05E-05
	30	1083,78	3,51	0,54	71%	2,95E-05

\* Superscript "ave" and "st.dev" indicate average and standard deviation values, respectively

Table 6.3. Normal stresses of non-printed and printed mortars

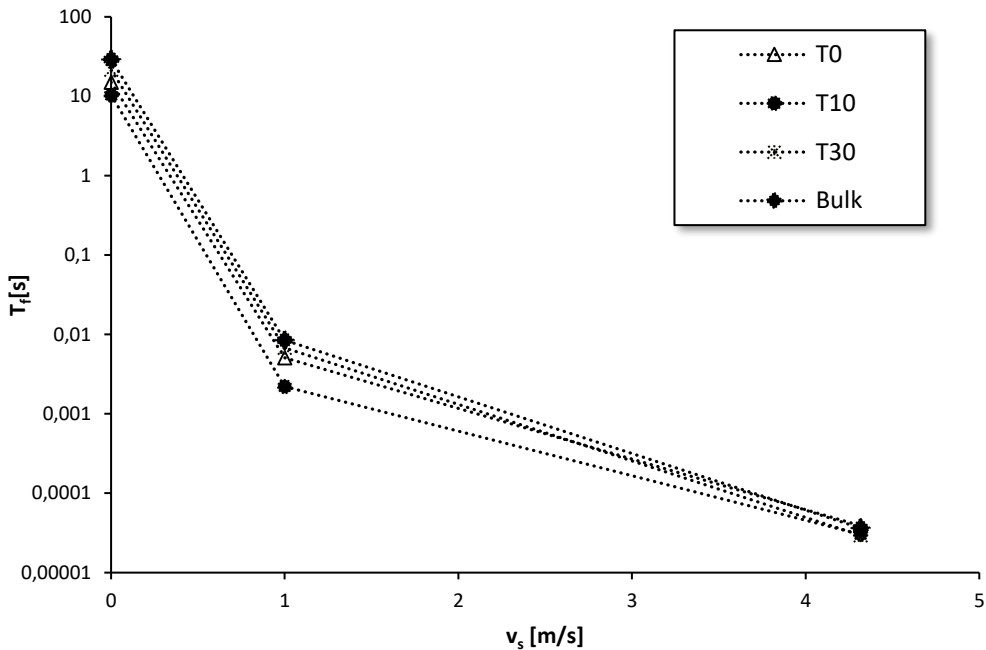


Figure 6.19. Fracture time,  $T_f$  vs. strain velocity,  $v_s$  data

Velocity conditions expressed in m/s are related to the traverse and bar displacement, for static and dynamic tests respectively. The fracture time is measured in correspondence with the maximum stress value, assumption justified by the fact that the mortar is characterized by a brittle-like behavior and so the onset of the first fracture is supposed correspond with the failure of the material.

Observing Figure 6.19 can be deduce that, as the printing waiting time increased, the fracture time decreases, being equal the strain-rate, confirming that the interface is a point of considerable weakness in the printed element and that, in every loading conditions, the main factor influencing negatively the bond strength is the overlapping time in the printing of the different layers. As expected, moreover, the specimen failure time shows a clear decreasing trend with the strain velocity.

A comparison between the different loading conditions, in terms of maximum normal stress exhibited by every specimen, with varying the waiting time, showing an increase in tension with the strain velocity and a decrease with time of waiting in the deposition of layers.

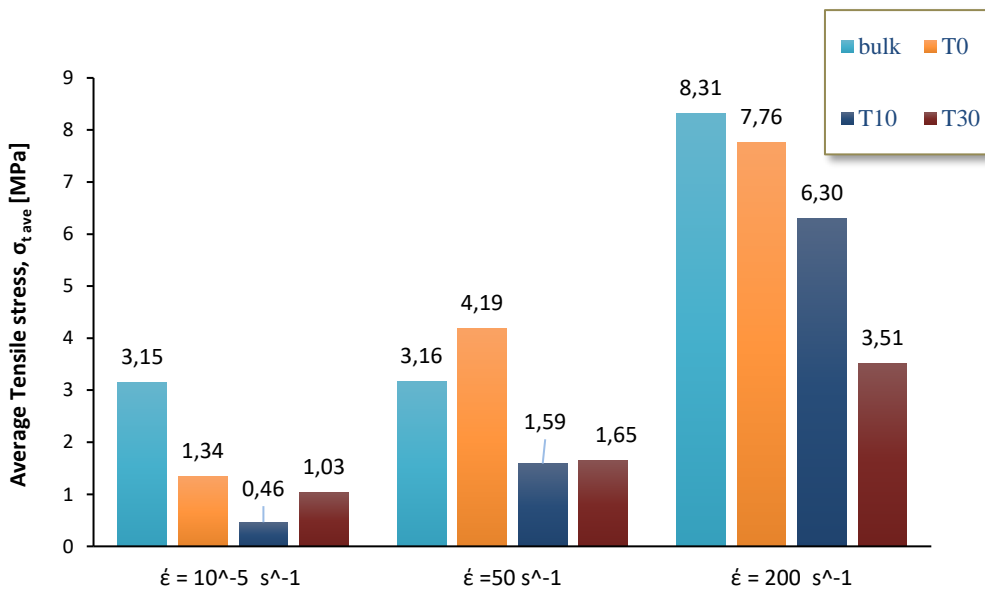


Figure 6.20. Static series variance, in terms of tensile stress, at different strain rates

In the following figure is reported stress vs time for the diverse batches of specimens subjected to tensile medium strain-rates tests. It can also be observed that the maximum stresses are different for the different groups and are reached at dissimilar times.

The difference could be explained mainly with the waiting time effect in the printed elements and so with the occurrence of micro-cracking in weaker material. In these specimens the presence of many propagating micro-cracks causes a fast damage of the material that leads to the decrease in the resisting capacity with respect to the material characterized by less waiting times.

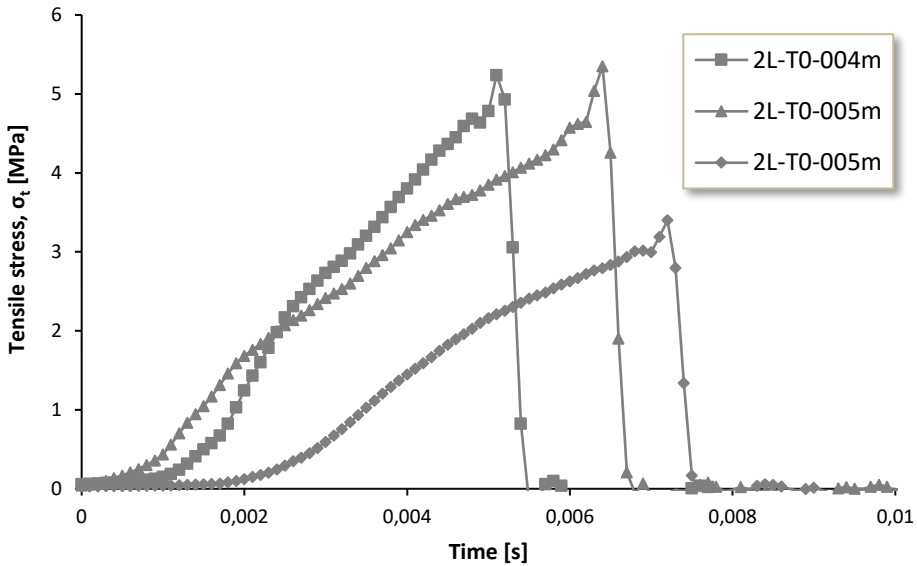


Figure 6.21. Stress vs time of group of specimens with  $T_s=0$  min

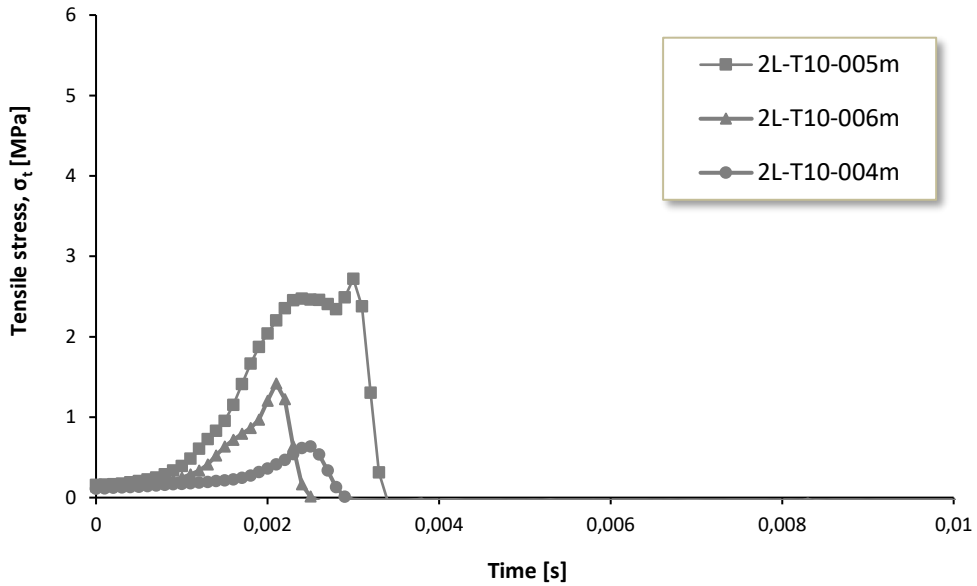


Figure 6.22. Stress vs time of group of specimens with  $T_s=10$  min

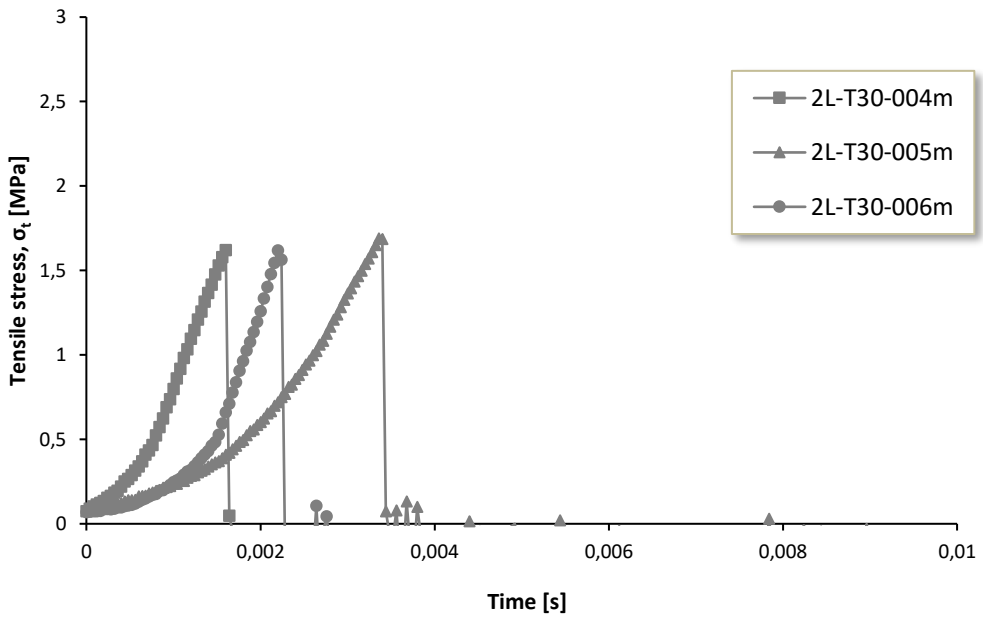


Figure 6.23. Stress vs time of group of specimens with  $T_s=30$  min

The following figures show printed concrete specimens before and after its



failure, subjected to high strain-rates. As it is already typically observed in normal concrete material, also in these types of elements a first crack develops approximately in the middle of the specimen length, defining a more or less clean cut at the cross-section according to more or less high waiting time between layers.



Figure 6.24. Printed specimen with  $T_S=0\text{min}$  before(left) and after (right) high dynamic tensile test

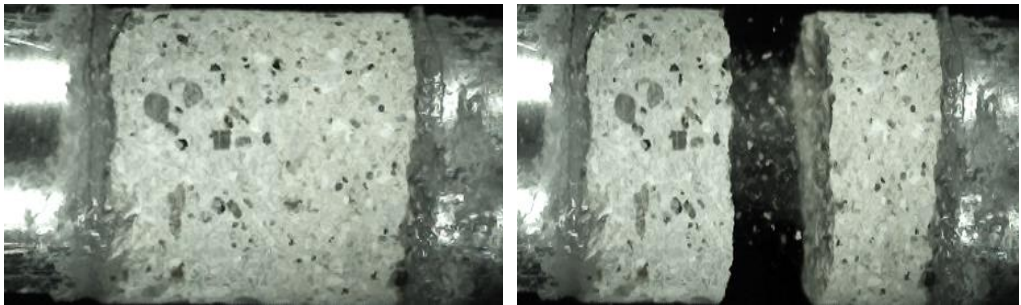


Figure 6.25. Printed specimen with  $T_S=30\text{min}$  before(left) and after (right) high dynamic tensile test

### 6.3.2. *Shear tests results*

In this section, shear tests results, in both static and dynamic conditions and for the different groups of specimen, are described. Initially are reported the pictures reproducing the specimen failure history at the main steps, i.e. the initial phase, the occurrence of the first crack and the complete failure, show also how the time elapsed between the different phases increases as the printing time between the layers decreases, underlining the influence of junction's weakness on the behavior of the entire element. Another factor to consider is the failure mode, which

appears to be sharper in correspondence of the interfaces with increasing  $T_s$ .

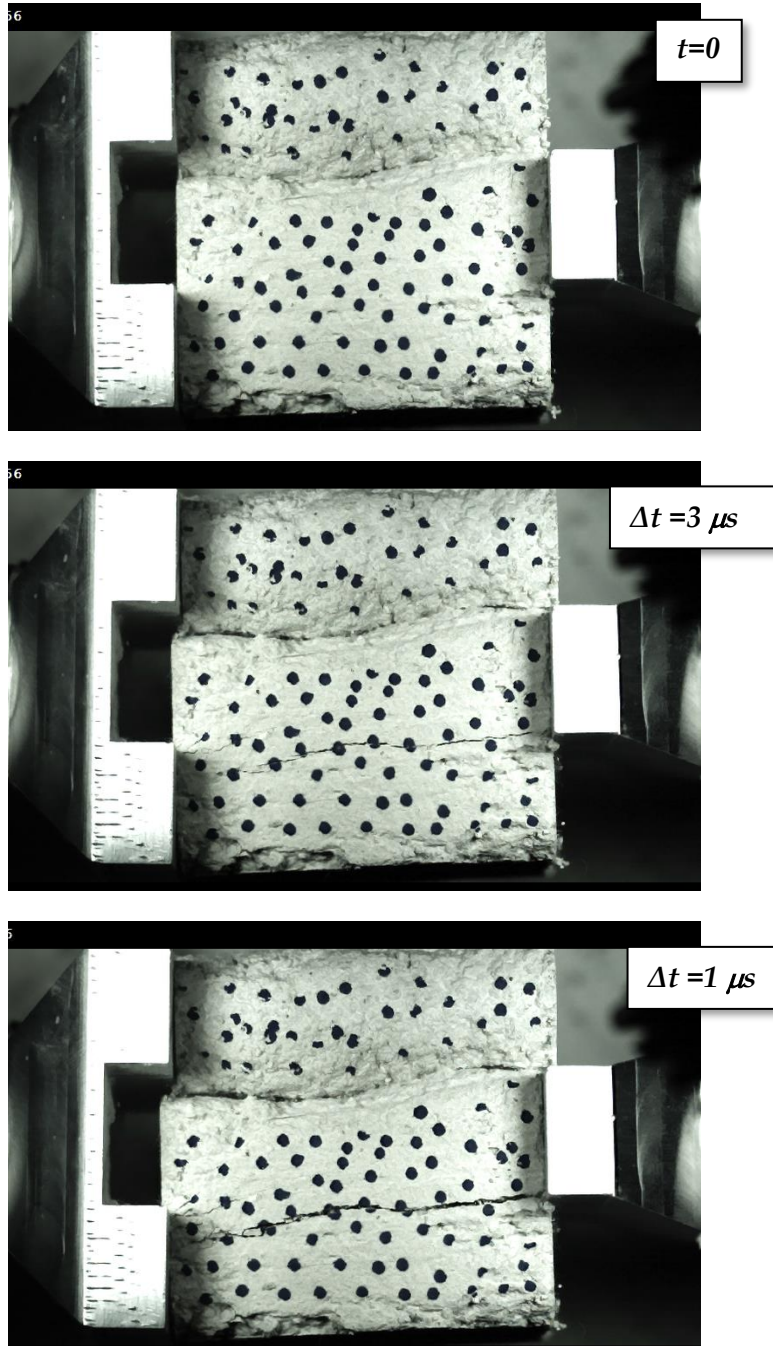


Figure 6.26. Specimen failure history subjected to dynamic shear test (ID specimen: 3L\_T0\_005) at different steps

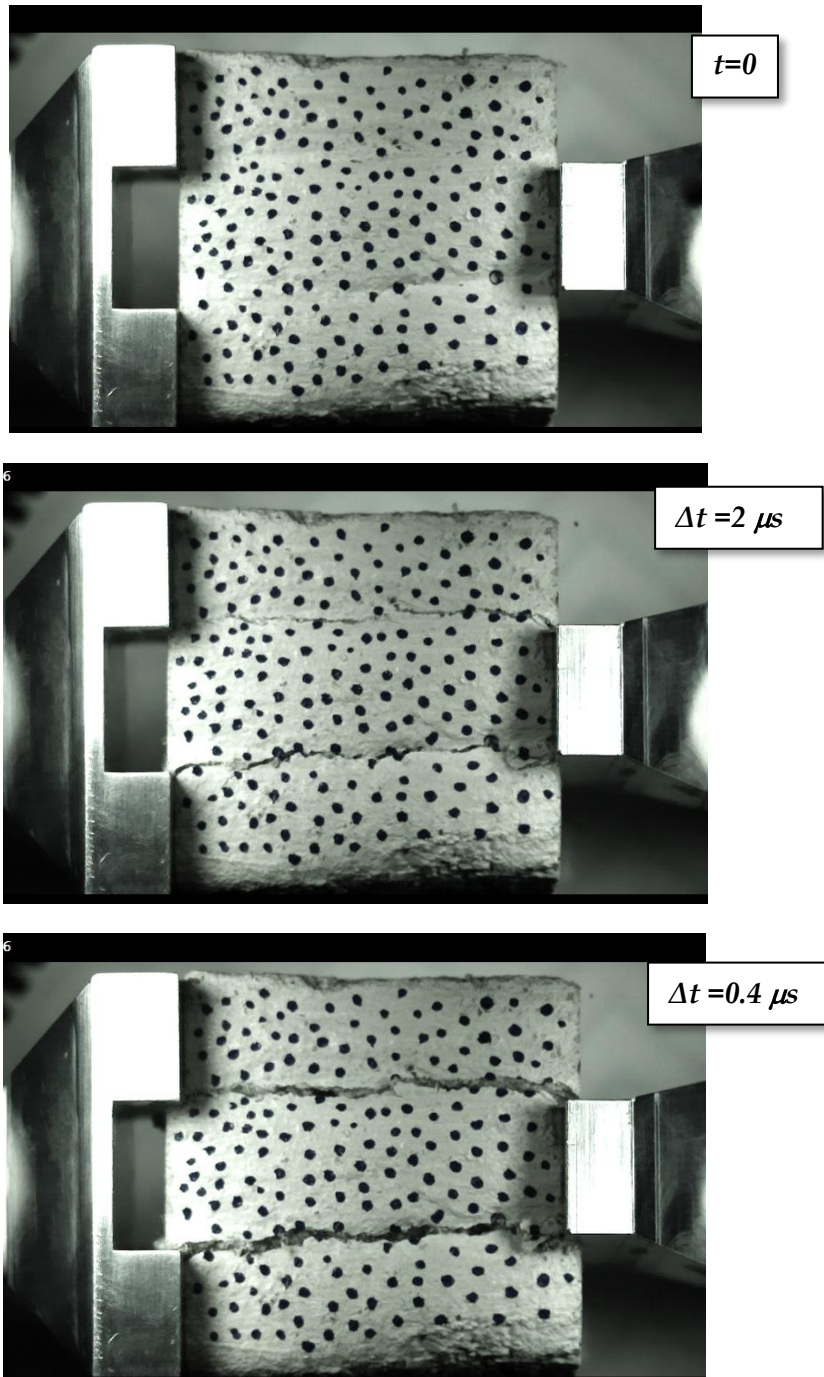


Figure 6.27. Specimen failure history subjected to dynamic shear test (ID specimen: 3L\_T10\_005) at different steps

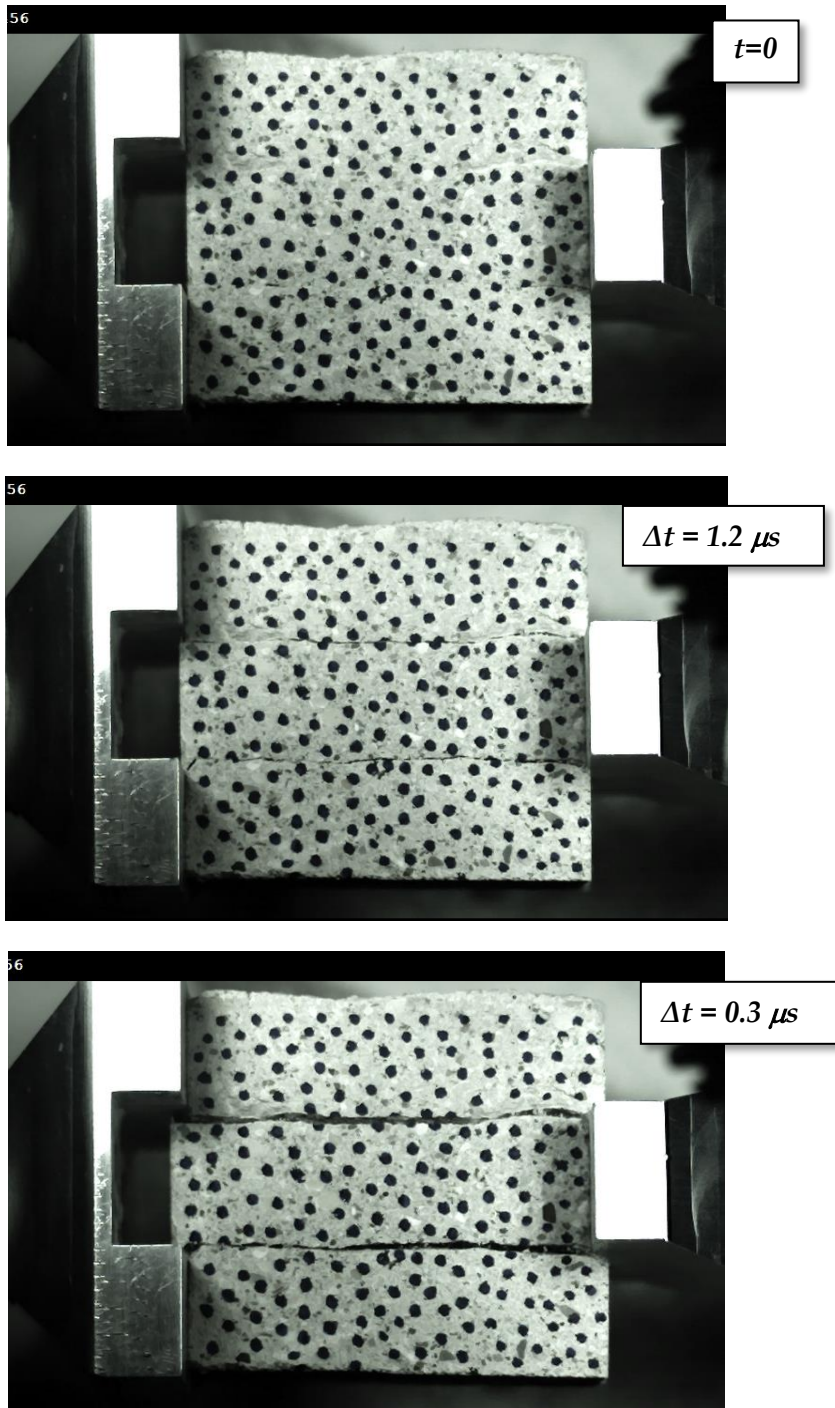


Figure 6.28. Specimen failure history subjected to dynamic shear test (ID specimen: 3L\_T30\_005) at different steps

Table 6.4 summarizes the average mechanical data observed for the analysed mortars, under static and dynamic load conditions, related in both cases to 4 groups with different delay times.

It is worth noting as the average value of the shear stress in dynamic condition for the bulk material is missing. The reason is why the strength exhibited by non-printed mortars is higher than instrumentation capacity, standing at about 34 kN and an incident bar speed of about 3.5m/s; so evidently the stress undergone by the bulk material in dynamic conditions is higher than material with  $T_s = 0$  min, in the same conditions.

Loading conditions	Resting time (min)	$\tau_{ave}^*$ (MPa)	$\tau_{st.dev}^*$ (MPa)	Bulk series variance (%)
Static	Bulk	5,57	0,57	
	0	5,06	0,26	-9%
	10	4,59	0,52	-18%
	30	2,63	0,80	-53%
	Bulk	-	-	-
Dynamic	0	6,65	0,3	16%
	10	5,60	0,38	0%
	30	4,13	0,83	-26%
DIF, $\tau$	0		1,19	
	10		1,22	
	30		1,57	

\* Subscript "ave" and "st.dev" indicate average and standard deviation values, respectively

Table 6.4. Transversal stress of non-printed and printed mortars

Experimental data indicate a significant decrease of strength with increasing intervals times, in other words a dynamic reduction up to about 40% for interlayer delay time of 30 min, as better the following graph shows.

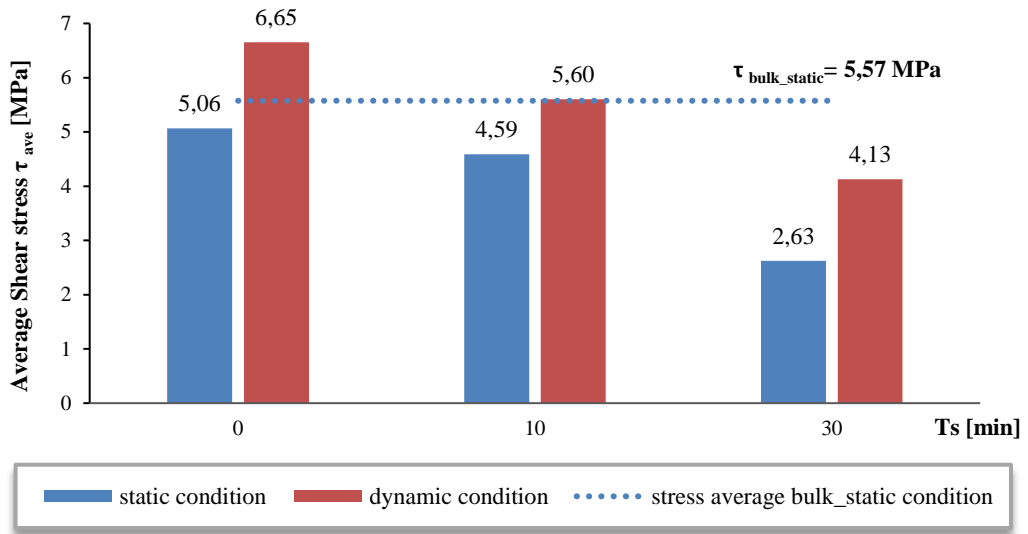


Figure 6.29. Bulk series variance percentage, in terms of shear stress

The occurrence of weak interface between layers in the printed samples justifies lower shear strength than non-printed samples, under both static and dynamic loading conditions, showing as confirm a more brittle failure mechanism presented in the previous figures.

In order to highlight as the shear strength decreases under dynamic conditions with increasing the waiting time, the results of the average failure stresses are processed in terms of Dynamic Increase Factor,  $DIF\tau$  defined as the ratio of the dynamic values of the tensile failure stress over the static tensile strength. The results are represented in Figure 6.30.

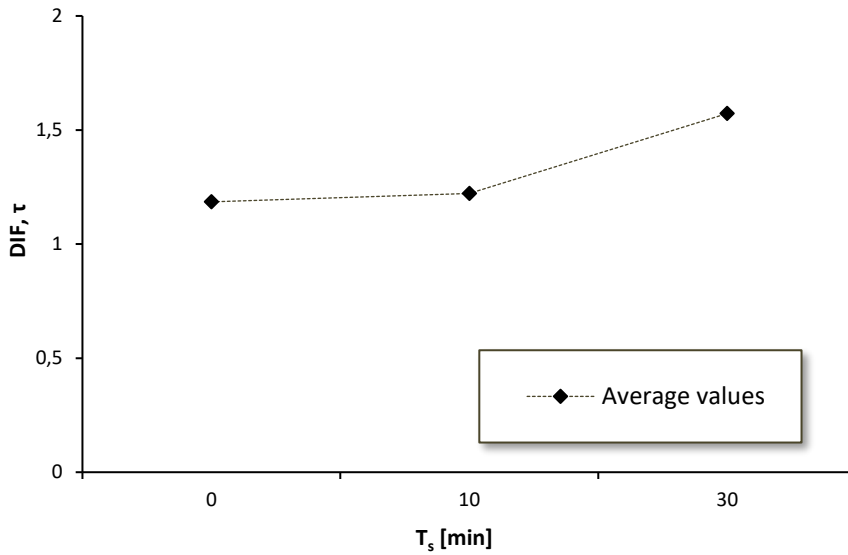


Figure 6.30. DIF $\tau$  vs. waiting time  $T_s$  experimental data

As expected, this figure reveals a behavior under dynamic conditions differing from the static one as waiting time increases; specifically, this gap becomes significant starting from  $T_s = 30$  min, presenting a variation of more than 20%, since increasing the printing time of a layer with respect to the previous one, the loss of adhesion between the two layers plays an important role.

## References

- Albertini, C.; Cadoni, E.; Labibes, K., “Mechanical Characterization and Fracture Process of Concrete at High Strain Rates”, Proceedings of the Second International Conference on Concrete under Severe Conditions (CONSEC '98), Norway, 1998, pp. 735-744.
- Asprone, D., Auricchio F., Menna C., and Mercuri V.. 2018. “3D Printing of Reinforced Concrete Elements: Technology and Design Approach.” *Construction and Building Materials* 165 (March): 218–31. <https://doi.org/10.1016/j.conbuildmat.2018.01.018>.
- Buswell, R. A., Leal de Silva W. R., Jones S. Z., and Dirrenberger J.. 2018. “3D Printing Using Concrete Extrusion: A Roadmap for Research.” *Cement and Concrete Research*. Elsevier Ltd. <https://doi.org/10.1016/j.cemconres.2018.05.006>.
- Cadoni, E., Albertini C., and Solomos G.. 2006. “Analysis of the Concrete Behaviour in Tension at High Strain-Rate by a Modified Hopkinson Bar in Support of Impact Resistant Structural Design.” *Journal de Physique IV (Proceedings)* 134 (August): 647–52. <https://doi.org/10.1051/jp4:2006134100>.
- Cadoni, E., Solomos G., and Albertini C.. 2009. “Mechanical Characterisation of Concrete in Tension and Compression at High Strain Rate Using a Modified Hopkinson Bar.” *Magazine of Concrete Research* 61 (3): 221–30. <https://doi.org/10.1680/mac.2006.00035>.
- Cadoni, E.. 2010. “Dynamic Characterization of Orthogneiss Rock Subjected to Intermediate and High Strain Rates in Tension.” *Rock Mechanics and Rock Engineering* 43 (6): 667–76. <https://doi.org/10.1007/s00603-010-0101-x>.
- Cadoni, E., Dotta M., Forni D., and Spätig P.. 2011. “Strain-Rate Behavior in Tension of the Tempered Martensitic Reduced Activation Steel Eurofer97.” *Journal of Nuclear Materials* 414 (3): 360–66. <https://doi.org/10.1016/j.jnucmat.2011.05.002>.
- Cadoni, E., and Forni D.. 2015. “Strain Rate Effects on Reinforcing Steels in Tension.” Edited by E. Cadoni. *EPJ Web of Conferences* 94 (September): 01004. <https://doi.org/10.1051/epjconf/20159401004>.
- Coppola, L., Coffetti D., Crotti E., Forni D., and Cadoni, E., 2018. “Fiber Reinforced Mortars Based on Free Portland-CSA Binders under High Stress Rate.” Edited by E. Buzaud, A. Cosculluela, H. Couque, and E. Cadoni. *EPJ Web of Conferences* 183 (September): 04013. <https://doi.org/10.1051/epjconf/201818304013>.
- Davies, J., Yim C.W.A., and Morgan T.G.. 1987. “Determination of Fracture Parameters of a Punch-through Shear Specimen.” *International Journal of Cement Composites and Lightweight Concrete* 9 (1): 33–41. [https://doi.org/10.1016/0262-5075\(87\)90035-2](https://doi.org/10.1016/0262-5075(87)90035-2).
- Fenu, L., Aymerich F., Francesconi L., Forni D., Tesio N., and Cadoni E.. 2018. “Dynamic Behaviour of an Earthen Material under Different Impact Loading Conditions.” Edited by E. Buzaud, A. Cosculluela, H. Couque, and E. Cadoni. *EPJ Web of Conferences* 183 (September): 02014. <https://doi.org/10.1051/epjconf/201818302014>.



- Lindholm, U. S., (1971) "High strain rate testing", in 'Techniques of Metals Research: Measurement of Mechanical Properties', edited by R. F. Bunshah, Vol. 5, Part 1 (Interscience, New York, pp. 199-271.
- Marchon, D., Kawashima S., Bessaies-Bey H., Mantellato S., and Ng S.. 2018. "Hydration and Rheology Control of Concrete for Digital Fabrication: Potential Admixtures and Cement Chemistry." *Cement and Concrete Research*. Elsevier Ltd. <https://doi.org/10.1016/j.cemconres.2018.05.014>.
- Nematollahi, B. Xia M., J. Sanjayan G., 2017. "Current Progress of 3D Concrete Printing Technologies Powder-Based 3D Printing Using Geopolymer/Conventional Cement for Construction Applications View Project Current Progress of 3D Concrete Printing Technologies," 260. <https://doi.org/10.22260/ISARC2017/0035>.
- Perrot, A., Rangeard D., and Pierre A.. 2016. "Structural Built-up of Cement-Based Materials Used for 3D-Printing Extrusion Techniques." *Materials and Structures/Materiaux et Constructions* 49 (4): 1213–20. <https://doi.org/10.1617/s11527-015-0571-0>.
- Wangler, T., Lloret E., Reiter L., Hack N., Gramazio F., Kohler M., Bernhard M., et al. 2016. "Digital Concrete: Opportunities and Challenges." *RILEM Technical Letters* 1 (October): 67. <https://doi.org/10.21809/rilemtechlett.2016.16>.



## Chapter 7

# CONCLUSIONS AND FUTURE DEVELOPMENTS: A SUSTAINABILITY PERSPECTIVE ON 3D PRINTING

Over the past decades, the industrial sector has been experiencing deep changes due to a steady growth in process automation. The increasing use of digitization has involved also the construction industry, impacting on the entire building process from the design to the manufacturing stage. Among digital processes, the construction products' manufacturing has been revolutioned by digital fabrication, referring to a new design-to-production framework which provides for the realization of concrete elements by means of a technology of 3D printing.

Among recent and innovative engineering technologies, 3D Concrete Printing (3DCP) can be considered as crucial and revolutionary for the construction industry. The use of an automated layer-by-layer deposition process with cementitious materials leads to high potential in terms of freedom in the design of shapes, elements and structures, functional and esthetic purposes. Then, other advantages include reduction in construction cost by avoiding formwork and human labor and in construction time by operating at a constant rate, increasing worker safety and production speed, minimizing the errors through automated material deposition. Finally, digital fabrication leads to more sustainability in construction by reducing waste generation.

Through the significant benefits, many concrete technological issues are still open and are yet to be investigated, such as the occurrence of cold joints, i.e. the weak surfaces generated at the bond interface through the extrusion of subsequent layers.

So, the assessment of layer interface mechanical behavior becomes a paramount topic, especially in an historical period, like this current one, where the Industry 4.0 has favored the integration of smart production systems and advanced information technologies, making it an important aspect on economic competitiveness.

Several works have shown the loss of structural stability and durability of printed elements, due to the presence of cold joints, but a specific focus on the interfaces' mechanical behavior is not available in the scientific literature. Despite the widespread potential of the innovative technique of 3D Printing, in fact, none of the current research works addresses particular attention to the the impact of interface's characteristics on the strength of elements resulting from 3D concrete printing (3DCP), when subjected to static and dynamic loading conditions, in terms of experimental and numerical analysis.

The situation outlined above is sufficient to understand that the state of the art on assessment of behavior of 3D printed concrete elements still needs to be advanced in several areas: interfaces' mechanical and numerical characterization, dynamic investigation and reinforcement strategy in particular.

A contribution towards this direction has been provided in this work through the study of response of concrete elements produced by 3D Printing technology, characterized by not sufficient interlaminar strength, therefore susceptible to high shear deformations and, eventually, shear failure. Special attention has been focused on failure mode prediction and shear and tensile capacity assessment. For these purposes, both experimental and analytical studies have been carried out and presented herein.

A critical review of the state-of-the-art and of the theoretical background, essential for the development of this work, has been performed. Firstly, the review process has been dedicated to the current additive manufacturing technologies and in particular on 3D printing application in the construction field. After a critical description of past experimental tests on printed concrete elements, the attention has been moved on the shear behavior numerical modelling available in literature. This part of the literature review has been used to reset past experimental setups and adapt it to the purpose of the work.

Several analytical models have been reviewed, too. First, some of the existing models for the evaluation of shear response of printed concrete elements have been briefly discussed, with a particular interest to the brittle strength evaluation

models, due to the concrete behavior as brittle-like material.

An experimental campaign was carried out at the Laboratory of the Department of Structures for Engineering and Architecture, University of Naples “Federico II”, to address the mechanical performance of 3D printed concrete elements, with varying an important factor affecting the response of the elements, i.e. the resting time, the time between the printings of two subsequent layers.

The design procedure aimed to characterize shear bond strength, by using a modified version of the punch-through shear test, analysing the elements in terms of failure mechanism and layers interaction. The experimental program comprised tests on 4 groups of specimens, characterized by different resting times (100s, 200s, 30min and 60min) and on a reference bulk group, made of cast concrete material. This difference highlighted the dependence of the cold joint by the building rate.

In order to investigate the local deformation components existing in the specimens (flexure contribution, shear contribution), an instrumentation was installed. In particular, it was composed of a system of Linear Variable Displacement Transducers (LVDTs), monitoring flexural and shear deformation, and DIC (Digital Image Correlation) measurements, employing the image registration techniques for accurate 2D and 3D measurements of changes in images.

Experimental results have been reported for every group of specimens. Depending on the waiting times, the specimens of bulk material have exhibited a shear failure, as in the case of printed specimens, where the shear cracks have been clearly showed. In particular:

- Bulk concrete specimens have presented the first cracks indeed arose at the inner edge of the supports, subsequently the propagation of the fractures happens along the surfaces located between the supports and the loading platen.
- Printed concrete specimens have showed two main stages, as in the case of bulk elements, but now the first linear part ends with the occurrence of a clear discontinuity that corresponds to the onset of the first crack in the interface surfaces and the relative load is called critical load,  $P_c$ . Subsequently, in the final part the load increases until its maximum value,  $P_{max}$ , which represents the complete

propagation of the shear failure.

The obtained results showed a certain dissimilarity in terms of  $P_{\max}$  values between the first two investigated groups of specimens (Series A and Series B), characterized by similar overlapping times and between the last ones (Series C and Series D). The same analysis involves  $P_c$  values of two groups, confirming that differences in the waiting time imply appreciable differences in terms of reached load, weakening the printed element.

It is worth noting that the difference between the maximum and critical load values tends to decrease as resting time increases. The reason is why the brittle behavior, exhibited by the reaching of failure as soon as the first crack occurs, is more remarkable in the case of elements with weaker interfaces.

The shear response of test specimens has been modelled through a numerical Finite Elements method, in which the core of the concrete which constitutes every layer and the interface links are considered separately.

The numerical simulation of the punch-through shear test aimed at reproducing the behavior of the specimen using as input parameter the experimental results. Specifically, since the main focus is on the evaluation of the “cold joints” behavior, i.e. the material which composes the link between two layers of concrete, the punch-through test has been carried out in order to measure the value of the critical energy release rate,  $G_{IIc}$ , parameter which the mechanical performances of joints are inherently dependent from. This parameter has been evaluated from the experimental curves of the elements by computing the area under the load vs displacement curve stopped at the value of critical load. Therefore, a cohesive surfaced based model is used to simulate the joints' behaviour. Besides, the same test has been simulated on elements without joints, i.e. made out of plain concrete, in order to assess the influence of interfaces. Furthermore, the material properties with refer to the single layer have been evaluated from uniaxial compressive tests and three points bending tests whose results have been then calibrated with aid of FEM simulations. In other words, a numerical method has been performed for evaluating the effect of the resting time on the inherent strength of the interfaces and validating the experimental results, respectively.

The numerical results showed that the adopted model is able to reproduce the experimental global response and the shear contribution with adequate accuracy. In fact, the difference in percentage between the mean experimental and numerical results, in terms of maximum load, was of the order of 10% and 3% for bulk and printed elements respectively.

In conclusion, the proposed testing framework turned out to be reliable for the determination of the critical energy release rate of the sliding mode of fracture. Moreover, the conducting tests have confirmed that the layers interfaces are weakness zones in spite of the time elapsed between the deposition of two subsequent layers. Indeed, the comparison between the numerical simulation of the punch-through shear test carried out on plain concrete element and layered element has shown a clear drop in terms of maximum load for the elements made out of distinct layers.

The experimental and numerical campaign revealed an effective weakness surface in the interface of the different layers, highlighting the need of some improvements in shear strength assessment. Starting from a critical analysis of studies available in literature, a new strategy of interlaminar reinforcement has been defined and proposed. This new model represents a first attempt to overcome the weakness of the joints and is characterized by the steel rods practice that pass across the junctions. Such reinforced elements have shown a different behaviour in terms of strains distribution, in fact the cracks originated in the middle of the lower part of the samples and at the cold joints at the same time; afterwards the cracks developed into the joints meaning that the at first, shear and flexural mechanisms are almost head-to-head but then, with the test progress the shear imposes over other mechanisms.

In term of loads magnitude, reinforced elements showed higher values compared to non-reinforced ones in the order of 15% which is an encouraging result.

Furthermore, the simulation of the reinforced layered elements' behavior has been implemented, reaching a difference between experimental and numerical results in the order of 2% in terms of maximum loads for elements with multiple layers with steel rods embedded. The higher strength in terms of maximum load value exhibited by the printed reinforced elements with respect to the printed unreinforced elements showed the influence and the benefits of the rods in the 3D concrete structure on the mechanical performances. In fact, the rods provided an increase in shear strength due to a sort of dowel action like in the common reinforced concrete elements.

In a general view of the obtained results, both unreinforced and reinforced elements cases presented the lower shear strength than elements characterized by bulk material, confirming the layers interfaces as weakness zones. In particular,

the experimental results about the plain concrete elements showed that the maximum load is about 45% higher than the maximum load of layered non reinforced elements, but about 20% bigger than deriving from reinforced elements.

While for static loading conditions some models for characterizing the mechanical properties of the 3D printed concrete elements are available in literature, concerning dynamic characteristics at different strain-rate levels no dedicated approaches is suggested in literature on the bond of interface between 3D printed layers. It is clear the need to investigate the dynamic characterization through high strain-rate failure tensile and shear tests. To this aim an experimental campaign has been implemented in this work, conducted at the DynaMat Laboratory of the University of Applied Sciences and Arts of Southern Switzerland (SUPSI) of Lugano.

Three batches of layered prismatic specimens, characterized by different waiting times ( $T_s=0\text{min}$ ,  $T_s=10\text{min}$ ,  $T_s=30\text{min}$ ), compared with reference bulk group, have been tested to analyse static and dynamic shear behaviour; and the same number of batches of cylindrical specimens have been experimented to investigate the direct tensile strength, in both static and dynamic configuration and at two different strain-rates ( $\dot{\epsilon} = 50 \text{ s}^{-1}$ ;  $\dot{\epsilon} = 200 \text{ s}^{-1}$ ). The shear dynamic mechanisms have been revealed by using a Modified Hopkinson compression Bar (MHcB) apparatus and by applying supports designed ad hoc to induce shear failure. The dynamic tensile failure tests at high and medium strain-rates, indeed, have been performed on elements with the changes in the time intervals between placements of subsequent layers using a Hydro-Pneumatic machine (HPM) and a Modified Hopkinson bar (MHB) apparatus, respectively.

The results exhibited a decrease in interface tensile dynamic strength with the waiting time up to over 90% for a medium strain-rate and over 20% for a high strain-rate, in both terms of maximum load and tensile stress. Furthermore, the fracture times, calculated for each group of specimens with different waiting times between the layers at which the fracture occurs, decrease with increasing interval times, at the same loading conditions.

The reason of this finding is the waiting time effect in the printed elements and so the occurrence of micro-cracking in weaker material.

Concerning shear behavior of the specimens, different failure modes were experienced, showing a more brittle failure mechanism in the specimens with



longer waiting times. In particular, the gap between static and dynamic conditions becomes significant starting from  $T_s = 30$  min, presenting a variation of more than 20%, since increasing the printing time of a layer with respect to the previous one, the loss of adhesion between the two layers plays an important role.

The tests presented herein can provide a suitable contribution for instance to quantify a safety factor that summarize the influence of joints on the mechanical behaviour of printed elements compared to plain-concrete elements.

Within this context, it is crucial to provide an overview of the impact of certain printing parameters on the mechanical performances of elements, in order to quantify the consequences through an appropriate characterization and improve the critical issues associated with the loss of strength at the interfaces.

These topics of research will encourage the development of the concrete printing technique, such that it can be taken into practice as a highly efficient design and construct method. This type of fundamental research can also be used to guide the new building standards that have to be developed, in order to not slow down the development of the technique, and not compromise the safety of the future user. A suitable balance will have to be found when exploring the frontiers of 3D printing. The research model that is presented in this thesis has shown a way to support the technique.

In the future, a more sustainable experimental investigation on the mixture components should be carried out, considering the strict relation between mixture design, mechanical properties and printing behaviour of concrete.

The mixture could include large size aggregates, such as carbon fibers wastes.

This is another step towards the call for a more sustainable built environment. Besides, this research challenge could be represent an interesting alternative in the development of fibre reinforced mixtures, increasing the ductility of the printed concrete.